6-1-2016

Investigation of Thermal Scaling Effects for a Turbine Blade Leading Edge and Pressure Side Model

Ryan A. Lynch

INVESTIGATION OF THERMAL SCALING EFFECTS FOR A TURBINE BLADE LEADING EDGE AND PRESSURE SIDE MODEL

THESIS

Ryan A. Lynch, First Lieutenant, USAF

AFIT-ENY-MS-19-J-072

DEPARTMENT OF THE AIR FORCE
AIR UNIVERSITY

AIR FORCE INSTITUTE OF TECHNOLOGY

Wright-Patterson Air Force Base, Ohio

AFIT-ENY-MS-19-J-072

INVESTIGATION OF THERMAL SCALING EFFECTS FOR A TURBINE BLADE LEADING EDGE AND PRESSURE SIDE MODEL

THESIS

Presented to the Faculty

Department of Aeronautics and Astronautics

Graduate School of Engineering and Management

Air Force Institute of Technology

Air University

Air Education and Training Command

In Partial Fulfillment of the Requirements for the

Degree of Master of Science in Aeronautical Engineering

Ryan A. Lynch, BS

First Lieutenant, USAF

May 2019

AFIT-ENY-MS-19-J-072

INVESTIGATION OF THERMAL SCALING EFFECTS FOR A TURBINE BLADE LEADING EDGE AND PRESSURE SIDE MODEL

Ryan A. Lynch, BS

First Lieutenant, USAF

Committee Membership:

Dr. M. D. Polanka
Chair

Lt Col. J. L. Rutledge
Member

Dr. M. F. Reeder
Member

AFIT-ENY-MS-19-J-072

Abstract

Recent experiments have attempted to quantify the overall cooling effectiveness at elevated temperature conditions. The Film Cooling Rig (FCR) at the Air Force Institute of Technology has been modified to better match the configuration of a similar large scale, low temperature rig at the Air Force Research Laboratory. This has enabled comparison and trend identification of how various properties scale from the low to high temperature condition. Various internal cooling and hole geometry configurations were investigated over a range of temperatures while utilizing the thermal scaling capability of Inconel 718. Film cooling trends and measures of overall effectiveness were matched, indicating the ability to scale among the temperature ranges tested: 350 K, 450 K, 500 K, and 550 K. Effects of blowing ratio, density ratio, and Reynolds number on overall effectiveness were investigated, as well as the ability of scaling effectiveness measurements between temperature regimes. It was found that an increase in Reynolds number caused a decrease in overall effectiveness. When matching flow parameters, this investigation found direct overall effectiveness scaling to be plausible. Additionally, overall effectiveness of about 0.5-0.6 during cases of no coolant flow were experienced due to conductive cooling to the environment. The highly conductive material also created significant heating of the coolant, drastically decreasing density ratio at the area of interest during testing, which plays an important role in assessing cooling performance.

Acknowledgments

This research would not have been possible without the integral help from a number of individuals. Nathan Clark facilitated the design and fabrication of the test model, while the AFIT and AFRL machine shops is appreciated for the physical fabrication and rig modifications. Carl Pickl's help within the lab was truly invaluable. James Tewaheftewa set the groundwork for the research and provided crucial assistance in working through the data analysis and testing processes. Dr. Clark is acknowledged for his very involved efforts in accomplishing the CFD analysis in tandem with the research. Thank you to Mike, Keith, Jamie, and Josh for your help around the lab and troubleshooting parts. Lastly, a major thanks to Dr. Polanka for your support, guidance, and extreme grace and patience as my advisor.

Ryan A. Lynch

Nomenclature

A	= area
ACR	= advective capacity ratio
b	= slot width
B	= calibration coefficient
Bi	= Biot number
c	= constant
d	= hole diameter
D	= diameter
DR	= density ratio
F	= calibration constant
g	= gap distance
h	= convective heat transfer coefficient
H	= height
I	= momentum flux ratio
$\mathscr{I}$	= radiative intensity
k	= thermal conductivity
L	= length
$\dot{m}$	= mass flow rate
M	= mass flux ratio
Nu	= Nusselt number
P	= pressure or pitch
Pr	= Prandtl number
q''	= heat flux
R	= gas constant or calibration constant
Re	= Reynolds number
S	= place holder
t	= thickness
T	= temperature
U	= velocity
V	= velocity
VR	= velocity ratio
W	= width
x	= length scale or axial position
Z	= distance from curved surface

Subscripts

0	= without film cooling
aw	= adiabatic wall
b	= blackbody
c	= coolant
ce	= coolant hole exit
ci	= coolant hole entrance

$cond$ = conduction
$conv$ = convection
ext = external
f = with film cooling
g = gas or real body behavior
h = coolant hole
imp = impingement plate
int = internal
LE = leading edge
p = plenum
r = relative nozzle
rad = radiation
S = surface
TS = test section
w = wall
∞ = freestream property

Greek

αR = thermal coefficient of resistivity
β = angular spacing
γ = injection angle
ε = emissivity
η = adiabatic (film cooling) effectiveness
θ = nondimensional wall temperature
λ = wavelength
μ = dynamic viscosity
ρ = density
ϕ = overall effectiveness
χ = coolant warming factor

Table of Contents

Page

Contents

List of Figures

Page

List of Tables

Page

INVESTIGATION OF THERMAL SCALING EFFECTS FOR A TURBINE BLADE LEADING EDGE AND PRESSURE SIDE MODEL

1. Introduction

While gas turbine engines have been used and continuously improved for over half a century, there is an ongoing desire to obtain more efficient cooling methods and longer lasting components given the ever-increasing hot gas temperatures. A major contributor to increased life span of these propulsion systems has been component cooling methods. The process to create and improve these cooling methods typically takes generous amounts of time and resources and many iterations. This investigation aimed to utilize and improve the ability of the Air Force Institute of Technology's (AFIT) Film Cooling Rig (FCR) to examine film cooling representative models and analyze heat transfer within these models.

1.1. Motivation

With increasing demands for more power and turbine component efficiency, the need for better and more effective designs remain. The high temperatures that combustors and turbines experience, along with frequent temperature fluctuations, cause degradation in the exposed materials over their use. Various cooling schemes allow these components to operate at higher temperatures, typically even beyond their melting points. The durability of gas turbine engines is strongly dependent on understanding these component temperatures.

1.2. Objectives

There were three main objectives in this investigation. The first objective was to investigate the effects of geometric scaling between the FCR and an existing large scale rig. The second objective was to further investigate the effects of various nondimensional parameters on scaling film cooling effectiveness. The third objective was to analyze the ability to scale overall effectiveness between temperature regimes by matching various nondimensional parameters.

1.2.1. Geometric Scaling

Utilizing a large scale model for testing has its advantages, to include benefits to structural integrity, manufacturing, and ease of instrumentation. The challenge that is present there, however, is how those results from a large scale, Biot number matched model relate to operational engine components. The FCR at AFIT was designed to geometrically scale down the larger model and analyze the ability to mimic film cooling effectiveness at similar flow conditions. But challenges existed with the FCR to mimic the full flow split around the semi-cylinder leading edge model of the large scale rig. The FCR implemented a bypass channel under the airfoil to accomplish the flow split, but did not fully replicate the flow around the large scale rig. But given this design deviation, flow conditions were still reached to enable comparison between geometrically scaled models.

1.2.2. Impact of Flow Parameters on Overall Effectiveness

Continuing with a moderately redesigned FCR model, the effects of nondimensional flow parameters on overall effectiveness were expanded upon. Two

main parameters for investigation were freestream Reynolds number and blowing ratio. Additionally, the FCR used electric inline heaters to control the freestream and coolant temperatures, allowing examination of different temperature regimes and density ratios.

1.2.3. Thermal Scaling of Inconel 718

Research involving the use of Inconel 718 for thermal scaling between temperature regimes was conducted by Stewart and Dyson [3]. The concept of the research was to show that results obtained in a given temperature regime could be replicated with the same model in a different temperature regime. If this were the case, experiments could be conducted at lower and safer temperature conditions and still apply to the same model at the higher operational conditions, creating a time and cost savings. The current research sought to use data collected on the FCR's Inconel 718 model to perform a similar analysis to the large scale model and predict fully operational performance.

1.2.4. Hole Exit Shape Effects

After the leading edge tests, an additional model was created to simulate a row of coolant holes on the pressure side of a turbine blade. The shape of the coolant hole exit has been previously investigated and shown to help increase film cooling effectiveness over the typical cylindrical hole shape. Having a shaped hole, such as fan or laid-back, increases the spreading of the coolant over the surface, improving the coolant coverage and increasing effectiveness [1]. A series of hole shapes were created, aiming to confirm existing research, as well as explore the effectiveness of a new hole shape.

1.3. Thesis Chapter Layout

To accomplish these objectives, Chapter 2 covers the relevant literature and background information for the film cooling concepts and measurement techniques used. Chapter 3 outlines the experimental setup for conducting the research. Chapter 4 reviews and analyzes the results obtained from the experimentation and test runs. The effects of various flow parameters, including blowing ratio, density ratio, and Reynolds number, are covered with how they affect overall effectiveness and its scalability between temperature regimes. Additional experimental effects of material conductivity and coolant heating on overall effectiveness were also found. Lastly, Chapter 5 is a summary of the work accomplished in this investigation.

2. Literature Review

Over the history of jet engine use, there continues to be a drive towards obtaining more efficient designs and longer lasting components, constantly pushing the limits of existing technologies. The drive for higher power outputs is coupled with higher temperatures that engine components must experience during operation, which typically will decrease the component lifespan without increased protective measures. Cooling methods have evolved to combat heating from the increased combustion temperatures, namely through employment of the concept of film cooling. This method seeks to create a buffer of cooler air between the hot freestream and the component surface, which will absorb and sweep away a portion of the heating that would have otherwise been soaked up by the component.

The present research aims to properly investigate various film cooling schemes along with the ability to scale effectiveness results to operational engine conditions. This investigation is carried out in the Air Force Institute of Technology's (AFIT) Film Cooling Rig (FCR), where previous iterations have investigated reactive film cooling, various cooling hole configurations and shapes, and initial scaling experiments. The focus of the current experiment seeks to further solidify experimental to engine condition scaling in addition to analyzing multiple hole configurations and geometries.

This chapter provides the background and surrounding information necessary to understand the film cooling concepts and experiments conducted. This chapter begins with an overview of the film concept in Section 2.1. Sections 2.2 and 2.3, respectively, describe geometric and flow parameters that are analyzed and matched in order to scale experimental to operational engine conditions. Section 2.4 discusses measurements of

cooling effectiveness, while Section 2.5 details methods of obtaining measurements of that performance. Lastly, Section 2.6 provides reasoning to choosing Inconel 718 as the experimental material.

2.1. Basic Film Cooling

Cooling methods used for airfoils have allowed gas temperatures entering the turbine to be higher than the normal operating temperature of the airfoils. In the 1960s bleed air from the compressor was initially routed through to the internal side of the turbine airfoils, which then progressed in the 1970s to being exhausted out through small holes drilled into the airfoil surfaces [1]. This is the basis of the film cooling concept, which is portrayed in Figure 1. This method provides a coolant to exit and create a film over that component, creating a heat transfer buffer between the hotter freestream and surface of the component. Their temperatures are measured in the figure as T_c, T_g, and T_w, respectively. Holes with proper spacing are typically used instead of slots or porous surfaces to maintain structural rigidity [1]. Understanding the effectiveness both internally and externally, as well as within the coolant hole paths, continues to pose research challenges.

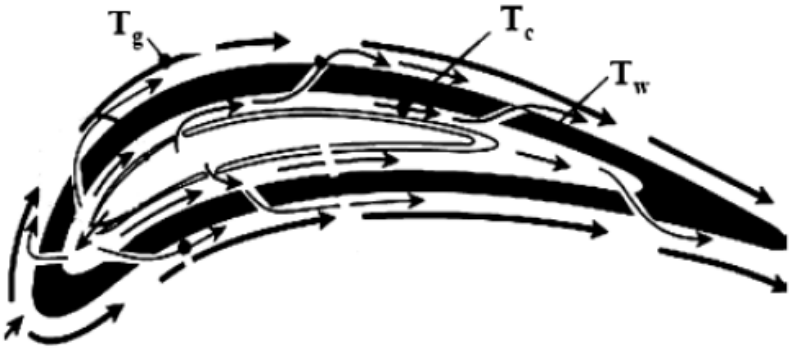

Figure 1: Film cooled airfoil [1]

The leading edge region of an airfoil or blade typically experiences the largest amount of heat loading, and therefore requires a more concentrated amount of cooling. Several closely spaced rows of coolant holes, generally referred to as the showerhead configuration, are typically utilized to achieve this concentrated cooling [1]. There are a few other unique leading edge designs that are utilized, such as a shrouded or guttered tip used by Rolls Royce in their commercial and military engines. These designs, while potentially increasing efficiency and lifespan, tend to be more complex, use more coolant flow, and are more expensive to manufacture [17]. The simpler and lower cost method of utilizing multiple rows of cooling holes at the leading edge has much more widespread use, however. Figure 2 shows this showerhead configuration, using seven staggered rows of coolant holes at the leading edge, consistent with the five- to seven-row showerhead configuration seen throughout the industry. Additional rows of holes are also incorporated down both the suction and pressure sides of the airfoil to supplement coolant as needed by design, along with slots at the trailing edge.

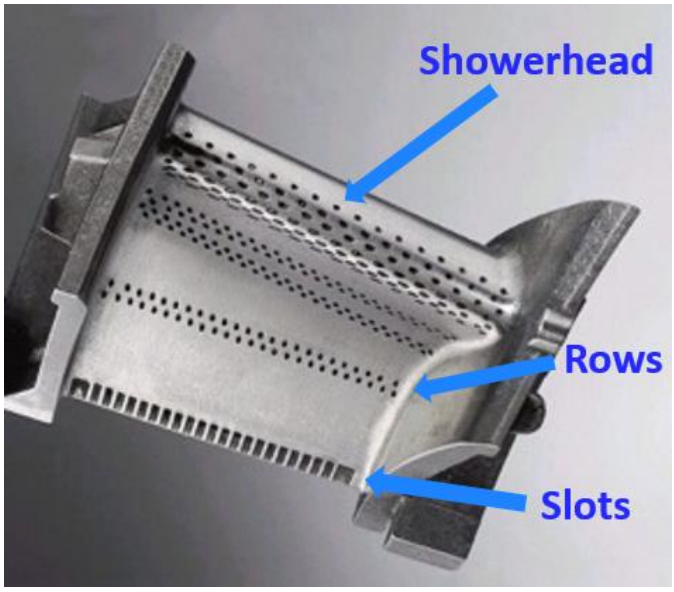

Figure 2: Schematic of Honeywell cooling hole layout [33]

2.2. Geometric Scaling Parameters

The basis of film cooling requires the use of holes or slots at various regions of the turbine blade to release the internal coolant through the blade and out into the freestream. Holes are typically used on the leading edge or near the leading edge on the pressure and suction sides, while slots are used more towards the trailing edge. For the scope of this investigation, cooling holes and their geometry and configuration will be the main focus areas. This section will consist of the pitch, hole ejection angle, hole shape, and hole configuration.

2.2.1. Pitch

The spacing between coolant holes is referred to as the pitch, p. The pitch for coolant hole configuration is typically three hole diameters, d, in the lateral direction, but up to eight can be used. Decreased spacing creates better coolant coverage, but also causes the coolant jets to interact. Wide enough spacing will allow them to act independently. Schmidt et al. [14] and Baldauf et al. [15] both performed studies that found pitch as small as three acting as independent jets, leading to the assessment that that spacing or greater could lend itself to analysis by superposition. Baldauf et al. also found that interactions between the jets occurred when $p/d = 2$.

In an experiment conducted by Dyson et al., they found that with increased pitch, ranging from 7.6d to 11.6d, the cooling effectiveness dropped by as much as 10% in some cases [5]. Having a large pitch causes the jets to act more independently and creates gaps in the coolant that then allows the hot freestream air to reach the component surface, which contradicts the purpose of film cooling.

2.2.2. Ejection Angle

In most film cooling applications, the holes through which the coolant exits are not usually perpendicular to the surface. The angle which the coolant hole makes with the surface is called the ejection angle, and is typically a value between 25-35 degrees. Too low of an angle would not be practical for construction purposes and also create a longer coolant hole path for additional coolant heating to occur. Conversely, too great of an angle would result in jet separation from the surface, allowing the hot freestream to reach under the jet and heat the component surface [1].

2.2.3. Hole Shape

Changing the shape of the coolant hole exits has also been previously explored. Shaped holes create notable improvements by increasing the spreading of the coolant into the freestream, creating a larger area of coolant effectiveness and allows for higher coolant flow rates [1] compared to the typical cylindrical shape. The higher flow rates are achievable due to the additional coolant spreading from the shaped holes. Some examples are shown in Figure 3. Expansion of the coolant hole towards the exit before entering the freestream allows the coolant flow to slow down, creating a lower momentum flux, and therefore a decreased tendency to separate. Increasing the coolant flow rate results in increased effectiveness with a shaped hole, where it usually creates a prominent drop in effectiveness for a normal cylindrical hole. In some cases, depending on shape and coolant flow rate, the heat transfer rates detrimentally increase with the shaped holes compared to the cylindrical holes, offsetting some of the benefit the shaped

holes bring [1]. While this slightly negative offset can occur, most applications of shaped holes still result in an overall increase in effectiveness over the cylindrical holes.

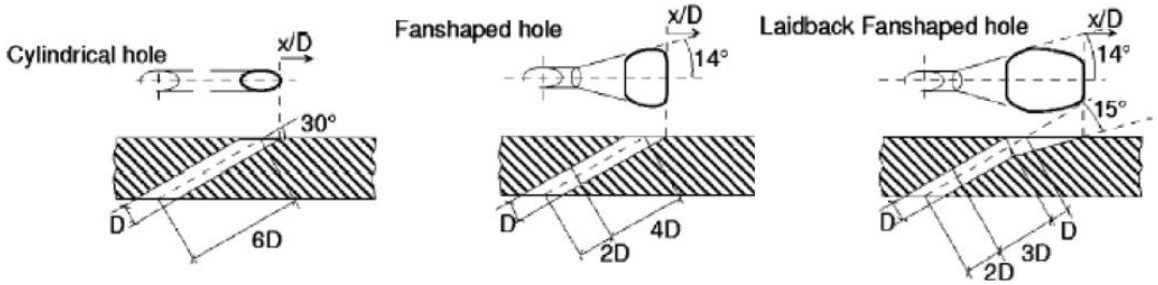

Figure 3: Schematics of different cooling hole shapes [16]

2.2.4. Hole Configuration

The need for film cooling varies depending on the location on the blade. The hole configurations needed can adjust each of the geometric parameters mentioned as needed by design. Film cooling on the leading edge is usually in the form of multiple rows of closely spaced holes, aptly called the showerhead, which is typically 6-8 rows for vanes and 3-5 rows for blades. A higher concentration of coolant holes is necessary because the leading edge sees the brunt of the hot freestream gases. Coupled with the stagnation line being located in this region, heat transfer rates can more than double in this region compared to the rest of the blade [1]. The challenge then arises of accurately understanding and counteracting the intense heating that is experienced.

Additional rows of film cooling holes on both the pressure and suction sides of the turbine blade are used to either create additional film cooling from the leading edge. Anywhere from one to four extra rows can be incorporated, depending on the design of the blade and the characteristics of the flow conditions [1]. Two closely spaced rows of holes have been proven most effective for supplying additional cooling to the blade surface while maintaining structural stability. For the scope of this research, however, a

single row of pressure side holes will be examined to highlight varying hole exit shape geometries.

2.3. Flow Scaling Parameters

As previously mentioned, scaling from experimental to engine conditions would allow for increased analysis of film cooling performance without the added complexity of attempting to take measurements within a fully operating engine. The assessment of film cooling performance that will be focused on through the research is overall effectiveness, ϕ, given in Eq. (1). This parameter incorporates the freestream temperature, T_∞, the actual wall temperature, T_w, and the coolant temperature in the internal channels before entering the coolant holes, T_{ci}. Values of overall effectiveness range from 0 to 1, with closer to 1 being more effective.

$$\phi = \frac{T_\infty - T_w}{T_\infty - T_{ci}} \tag{1}$$

There are a number of flow parameters that, if and when matched, allow for scaling effectiveness between these conditions. Section 2.3.1 describes the Reynolds number to help set the flow regime around the blade or model. The Biot number, outlined in Section 2.3.2, incorporates the conductive and convective heat transfer properties of the material used, which is important to match when conducting conjugate heat transfer analysis. Section 2.3.3 introduces density ratio along with three other parameters, blowing ratio, momentum ratio, and velocity ratio, which would supplement the matching efforts when density ratio cannot be fully matched. Lastly, Section 2.3.4 describes the advective capacity ratio, which is used for thermal scaling based on the individual gases contained within the flow.

2.3.1. Reynolds Number

The first parameter that can be matched for scaling between conditions is the Reynolds number, defined in Eq. (2) as the ratio of flow velocity, *U*, and reference length, *L*, to the kinematic viscosity, *ν*. The Reynolds number helps determine the flow conditions that are being experienced, such as laminar or turbulent flow.

$$Re = \frac{UL}{\nu} \tag{2}$$

A CFD study conducted by Greiner et al. argued that matching the Reynolds number of the coolant is more important than matching the Reynolds number of the freestream [3]. This may very well be the case, but the Reynolds number of the coolant cannot be matched alone and still be scalable to engine conditions. The fact of both coolant and freestream Reynolds numbers being matched for scalability still remains.

2.3.2. Biot Number

One key parameter that must be matched is the Biot number, *Bi*. One-dimensional, steady state, heat transfer analysis reveals the importance of this parameter both to establish the correct heat flow through the part and that this parameter is one of the keys to replicate the engine environment at room temperature. This must be done along with matching the ratio of heat transfer coefficients simultaneously with the film cooling conditions to obtain a matched overall effectiveness [2], given in an alternate form from Albert et al. [13] in Eq. (3). This form also incorporates the film cooling effectiveness, η, and ratio of convective heat transfer coefficients, h_f/h_c.

$$\phi = \frac{1-\eta}{1 + Bi + \frac{h_f}{h_c}} + \eta \tag{3}$$

The Biot number can then be incorporated to more accurately determine the environmental effect that the airfoil would experience with the external convective heat transfer coefficient, h_f, airfoil thickness, t_w, and conductivity, k_w [2]. This relationship would suggest the introduction of the Biot number (*Bi*), defined in Eq. (4).

$$Bi = \frac{h_f t_w}{k_w} \tag{4}$$

Dyson et al. [5] matched the Biot number to measure overall effectiveness for an experimentally simulated turbine blade leading edge. By using a material with a high conductivity such that the Biot number was matched and measuring overall effectiveness, an accurate representation of the temperature distribution as would occur on an actual turbine airfoil was achieved. This would allow the identification of any "hot spots" that may occur which would potentially become a weak or breaking point for the blade over time.

2.3.3. Density Ratio

As stated by Bogard and Thole [1], many gas turbine engines operate with a coolant temperature equal to about one half of the freestream temperature, resulting in a coolant to freestream density ratio, *DR*, of about 2. Given in Eq. (5), the density ratio is the density of the coolant, ρ_c, over the density of the freestream, ρ_∞.

$$DR = \frac{\rho_c}{\rho_\infty} = \frac{T_\infty}{T_c} \tag{5}$$

A *DR* of 2.0 is typically difficult to achieve in experimental conditions, however, and is usually much lower. In order to still be able to scale and relate performance

metrics to the higher *DR* at engine conditions, one of the following parameters must be matched [1]. These include the mass flux, or blowing, ratio, *M*,

$$M = \frac{\rho_c U_c}{\rho_\infty U_\infty} = \frac{A_\infty}{A_c}\frac{\dot{\mathrm{m}}_c}{\dot{\mathrm{m}}_\infty} \tag{6}$$

the momentum flux ratio, *I*,

$$I = \frac{\rho_c U_c^2}{\rho_\infty U_\infty^2} \tag{7}$$

and the velocity ratio, *VR*.

$$VR = \frac{U_c}{U_\infty} \tag{8}$$

Each ratio corresponds to a different scalable aspect of the flow characteristics. The mass flux ratio describes the proportionate coolant flow rate with respect to the freestream, while the momentum flux ratio pertains more to the dynamic interaction between the coolant and freestream flows. The momentum flux ratio will describe how far a coolant jet may penetrate into a freestream flow, and how easily it gets turned back down to the wall. Lastly, the velocity ratio scales the shear layer between the coolant and freestream flow, effectively describing turbulence production [1].

Of these parameters, the most commonly used throughout experiments and among the literature is the mass flux ratio. This is due to simply requiring the knowledge of the coolant and freestream areas, A_c and A_∞, along with their corresponding mass flows, $\dot{m}_c$ and $\dot{m}_\infty$, two easily known or controlled measurements. Momentum flux ratio is the next most common, and is frequently investigated alongside the mass flux ratio. Much of the literature is discussed in terms of *M* and *I*, depending on which aspect of film cooling is focused on. Flow visualization and jet separation effects are typically in terms of

momentum flux ratio because that is describing the flow behavior itself. Bulk heat transfer and material temperature effects due to the flow, however, are more often expressed in terms of blowing ratio.

Wiese et al. [8] experimentally investigated effects of a range of mass flux and momentum flux ratios of the leading edge showerhead region of a simulated turbine blade. By ranging mass flux ratio from 1.0 to 1.5 to 2.0, the increase in coolant flow was shown to have a negative effect at the leading edge showerhead region due to being on or within the first set of coolant row holes, causing too much coolant penetration into the freestream and away from the surface. This occurrence is due to the sharply decreased freestream velocity within the stagnation region, allowing the coolant flow to greatly overpower the freestream and create these adverse effects. Blowing ratio of 1.0 maintained some positive film cooling effects, however. The investigation also similarly ranged the momentum flux ratio, and while behavior at I = 1.0 was similar to the blowing ratio case that Wiese conducted with a positive interaction being observed, increasing to 1.5 and 2.0 showed some reattachment of the coolant jets, increasing cooling effectiveness vice the blowing ratio cases by about 0.1.

2.3.4. Advective Capacity Ratio

The final flow parameter is the advective capacity ratio, *ACR*, which incorporated the thermal effects of the flow by introducing the specific heat of each gas in accordance with Eq. (9).

$$ACR = \frac{c_{p,c}\rho_c U_c}{c_{p,\infty}\rho_\infty U_\infty} \tag{9}$$

ACR behaves similarly to *M*, but is influenced by the individual gas thermal properties and is most useful in the analysis of a reacting flow where multiple gases are present. While the current research only used air, *ACR* data can still be used to compare to other research. Fischer [30] analyzed the *ACR* of various gases and its effects on scaling adiabatic effectiveness between temperature conditions. He found that the use of ACR collapsed the adiabatic effectiveness profiles between all gases used prior to separation. Separation began to occur at I > 1.2, after which the data no longer collapsed.

2.4. Measurements of Effectiveness

Utilization and analysis of the aforementioned parameters when conducting experiments gives a level of insight into the effectiveness the film cooling methods have in reducing the temperatures seen by the components of study. There are two main measures of effectiveness throughout the literature and previous research. The first, outlined in Section 2.4.1, focuses on solely the film cooling's effectiveness of coverage, also known as the adiabatic effectiveness. The measure of overall effectiveness, described further in Section 2.4.2, additionally incorporates heat transfer due to conduction through the component surface from the freestream flow in conjunction with the coolant flow through the internal channels.

2.4.1. Adiabatic Effectiveness

Overarching relationships have been created to gain insight into the effectiveness of film cooling techniques. Assuming an adiabatic (non-conducting) scenario, a common parameter used is the nondimensional film effectiveness, η, also referred to as adiabatic effectiveness, shown in Eq. (10). In this equation, T_∞ is the freestream temperature, T_{aw}

is the temperature of the adiabatic wall, and T_{ce} is the temperature of the coolant at its exit. The values of adiabatic effectiveness range from 0 to 1, where values closer to 1 are indicative of more effective cooling.

$$\eta = \frac{T_\infty - T_{aw}}{T_\infty - T_{ce}} \tag{10}$$

Adiabatic effectiveness is analyzed as a nondimensional variable so that it can be scaled and related to engine conditions [1], one of the main goals of this current film cooling research. Through this employment, adiabatic effectiveness can be used to estimate the engine's metal surface temperature and is dependent on coolant and freestream flow behavior [2]. While the interaction between the coolant and freestream plays a large role in cooling performance, there are additional influential factors that need to be considered because no material or surface can be truly adiabatic. This behavior can be represented with the analysis of various parameters, some of which are detailed in Section 2.3.

2.4.2. Overall Effectiveness

The adiabatic effectiveness only captures the external effects of the coolant flow, and therefore further analysis is required because other modes of heat transfer are occurring during engine operations. Specifically, heat is conducted through the wall due to the convection of the external freestream and internal coolant flows, depicted in Figure 4.

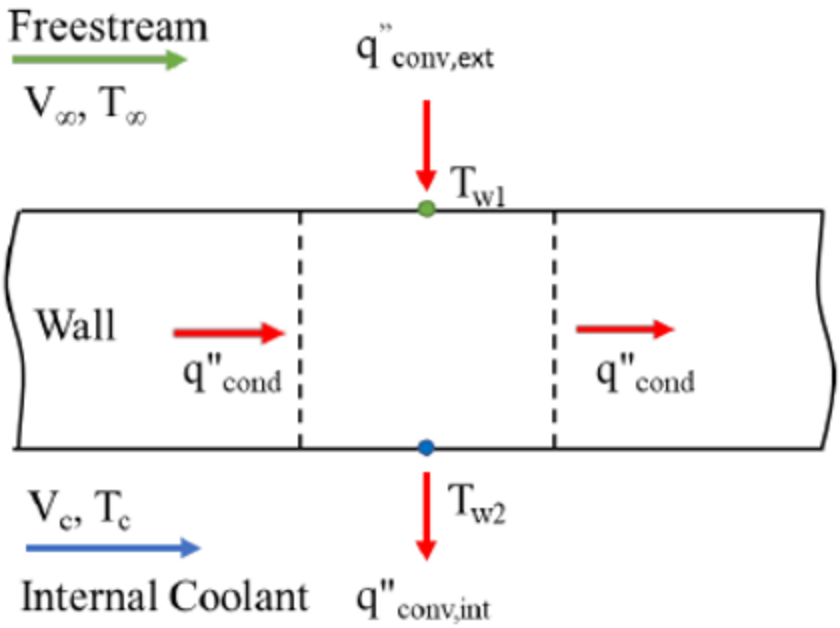

Figure 4: Basic modes of heat transfer in component wall including external/internal convection conduction [2].

One-dimensional heat transfer is given in Eq. (11), where k_w is the thermal conductivity of the material and dT/dx is the temperature gradient through the material. While not given, conduction is occurring in multiple directions and the equation can be converted accordingly. Convective heat transfer between a fluid and a material is given by Eq. (12), where h is the convective heat transfer coefficient, T_w is the wall temperature, and T_∞ is the fluid flow temperature. The temperatures used are both either the external freestream or internal coolant temperatures and corresponding wall temperatures used together.

$$q"_{cond} = -k_w \frac{dT}{dx} \tag{11}$$

$$q"_{conv} = h\,(T_w - T_\infty) \tag{12}$$

In addition to the equations given previously, Rutledge et al. [6] outlined another useful expression for the overall effectiveness in Eq. (13).

$$\phi = \frac{(T_\infty - T_w)}{(T_\infty - T_{ci})} = \frac{\chi\eta\left(Bi + \frac{h}{h_i}\right) + 1}{\frac{h}{h_i} + Bi + 1} \tag{13}$$

$$\chi = \frac{T_\infty - T_{ce}}{T_\infty - T_{cp}} \tag{14}$$

This expression incorporated a new term, the internal coolant warming factor, χ, defined in Eq. (14). The internal coolant warming factor refers to the additional heating the coolant experiences as it travels between the coolant hole plenum through to exiting the cooling hole, and can be expected to match for scalability when matching material conductivity and flow through the holes. Bryant [23] sought to better understand where the coolant is warmed, so she split the coolant warming factor into two components, the warming experienced within the plenum itself, χ_p, and with the coolant hole, χ_h.

$$\chi_p = \frac{T_\infty - T_{ci}}{T_\infty - T_{cp}} \tag{15}$$

$$\chi_h = \frac{T_\infty - T_{ce}}{T_\infty - T_{ci}} \tag{16}$$

Of these, the value that is closest to zero indicates the location where the most warming is occurring. Multiplying these two terms would yield the overall value of χ, with a value closer to unity being indicative of less warming. The highest of the three blowing ratios tested, M = 0.9, was the only instance where freestream ingestion into the coolant holes did not occur. Given that ingestion is not usually experienced at engine conditions, these values were most representative of where the most warming occurs. Here the hole warming factor was 0.85 and the plenum warming factor was 0.95, leading to χ = 0.81

and the conclusion that at normal engine conditions without ingestion, most of the warming experienced occurs within the coolant holes versus the plenum. This conclusion is quite relevant because within the leading edge, or showerhead, region, there are multiple rows of closely packed coolant holes, resulting in the coolant warming factor having a much more significant impact than a single row of holes on a surface side.

This new form of ϕ more distinctly presents and relates the parameters, including the impact of the *Bi*, that need to be matched in order to achieve accurate results. When the Biot number, along with the heat transfer ratio and adiabatic effectiveness can be simultaneously matched, then scalability to engine conditions can be achieved.

2.5. Data Measurement Methods

Through the course of experimentation, two main temperature measurement methods will be utilized: thermocouples and IR thermography. The thermocouple temperature readings are able to provide measurements at various locations on and within the model, as well as aid in calibration of the IR data. The IR thermography readings and images provide temperature mapping of the object's surface to identify temperature trends with varying parameters and allow for effectiveness analyses.

2.5.1. Thermocouples

The first of the two temperature measurement methods is the use of thermocouples. This simple method provides accurate temperature readings at discrete locations over a large range of temperatures. Thermocouples such as Omega® k-type thermocouples are widely used. These thermocouples operate by using two different metals joined together and placed into the area or on the surface which a temperature

reading is desired. This reading is completed within a circuit also containing a value at a known temperature, and the difference in voltage between the readings is converted to a temperature output. These Omega® thermocouples have an operating range of -200℃ to 1250℃ with an error range of either ±2.2℃ or ±0.75%, whichever value is larger [19]. While accurate in temperature readings, thermocouples do have their drawbacks. For instance, they cannot provide readings for a larger area, unless that area is entirely covered in thermocouples, but that would not be practical. Additionally, small changes in where the thermocouple is placed can have large impacts on the temperature reading it provides, due to potentially large gradients existing in a certain area of a surface or flow. Lastly, thermocouples are physically intrusive and can cause adverse effects if inserted into a fluid flow where small variants make a difference. As a result, proper consideration of placing thermocouples should be taken.

2.5.2. IR Thermography

Infrared (IR) thermography is typically used in thermal investigations to capture temperature measurements and mappings to be used in conjunction with other thermal analysis. Through this analysis, surface temperatures can be found and used in the effectiveness calculations for this and other related research, including that of Tewaheftewa [12] and Bryant [23]. As a non-invasive technique, IR thermography only requires clear optical access to view the object of interest, allowing for the testing environment to remain undisturbed.

IR thermography is a technique that measures the radiation emitted by an object's surface. Radiation emitted by a blackbody emits in accordance with Eq. (17), where σ is

the Stefan-Boltzmann coefficient and T_w is the surface temperature of the object of interest.

$$q''_{rad,b} = \sigma T_w^4 \tag{17}$$

The blackbody object is an idealized concept, however, because no real object has an absolute perfect emissivity. The true value of an object's radiation is some fraction below the blackbody, which is partially determined by the surface's emissivity, ϵ, which has a value between 0 and 1. Eq. (18) represents the radiation of a real object.

$$q''_{rad,b} = \varepsilon \sigma T_w^4 \tag{18}$$

IR thermography uses an IR detector to measure and record the radiation emitted by a surface and, when coupled with the known surface emissivity, can determine the surface temperature of the object. This method is advantageous because it is non-intrusive and therefore will not disturb the flow. The result is also a two-dimensional temperature mapping of the surface without needing extra equipment [24]. Test surfaces are usually painted with a high temperature flat black paint in order to achieve a reliable surface emissivity [24]. A disadvantage to IR thermography is the need for optical access, typically using an IR-transparent window made of quartz [25], zinc selenide [24], sodium chloride [26], or sapphire [22].

While IR thermography can be used in various heat transfer tests, knowing the emissivity of the object's surface does not guarantee an accurate temperature reading from the surface radiation. Other sources of radiation exist that can skew the radiation level measured from the surface and must be accounted for. This is typically

accomplished by performing an in-situ calibration with embedded thermocouples on the object's surface to provide a series of reference temperatures for the calibration.

Martiny et al. [27] and Ochs et al. [28] both employed one of the two main methods of performing in-situ calibrations. This method begins with observing how spectral infrared radiation is related to blackbody temperature through Planck's Law, which is shown in Eq. (19),

$$q_b^{"}(\lambda) = \frac{c_1 \lambda^{-5}}{e^{\frac{c_2}{\lambda T}} - 1} \tag{19}$$

where λ is wavelength and c_1 and c_2 are physical constants. But emissivity must also be incorporated because real objects radiate below the blackbody value, and this relation is shown in Eq. (20).

$$q_g^{"}(\lambda) = \varepsilon(\lambda) * q_b^{"}(\lambda) = \varepsilon(\lambda) * \frac{c_1 \lambda^{-5}}{e^{\frac{c_2}{\lambda T}} - 1} \tag{20}$$

With this new relation, the temperature of the object, *T*, could then theoretically be solved for by measuring the spectral irradiance, assuming the object's emissivity is known. This relation for *T* is shown in Eq. (21).

$$T = \frac{c_2/\lambda}{\ln(\frac{\varepsilon(\lambda) * c_1 * \lambda^{-5}}{q_g^{"}} + 1)} \tag{21}$$

By the same reasoning, Martiny et al. [27] presented a semi-empirical relation based on Planck's Law. Shown in Eq. (22), this relation presents the radiation detected, *I*, in terms of the temperature of the object, *T*, along with three new parameters: *R*, *B*, and *F*.

$$I = \frac{R}{e^{\frac{B}{T}} - F} \tag{22}$$

Once again rearranging and solving for T gives Eq. (23).

$$T = \frac{B}{\ln(R/I + F)} \tag{23}$$

Given this new form, the three remaining coefficients, *R*, *B*, and *F*, could be determined using a nonlinear least square fit, described more in Martiny et al. [27], and known pairs of temperatures and detected radiation values.

The newer alternative in-situ calibration is the method that has been used in several experiments at AFIT's small scale film cooling rig [12,21,22] and used the relation between radiative heat flux and temperature measurements in accordance with the Stefan-Boltzmann Law from earlier. This technique relates the physical temperatures measured on the surface to the radiative intensity emitted, using surface thermocouples and an IR imager, respectively. Because radiative heat transfer follows a fourth-order behavior, a relationship between temperature and radiative intensity can be formed, given in Eq. (24).

$$T = a\mathcal{I}_{rad}^{1/4} + b \tag{24}$$

In this equation, $\mathcal{I}_{rad}$ is the count of photons hitting the IR imager's sensor and *a* and *b* are constants created by the curve fit. The curve fit is produced from a batch of data that was collected at a range of surface temperatures to span the range expected during testing. Figure 5 shows and example of this curve fit from Tewaheftewa [12].

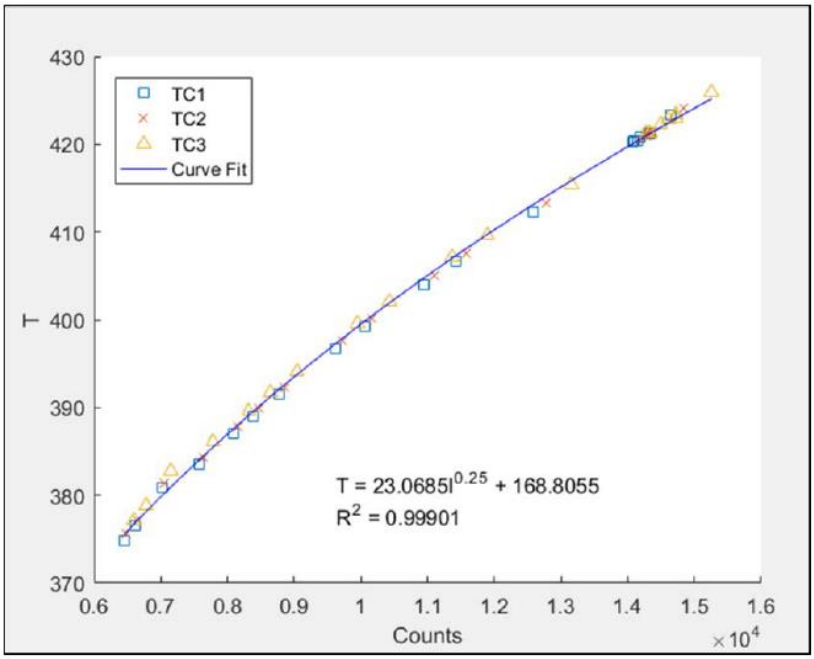

Figure 5: In-situ IR calibration example [12]

This relationship and style of in-situ calibration can be modified to incorporate various relationships that exist in other environments, as shown by Ashby [22]. These extend to adapting the curve fit to use a more precise or a variant of the equation, or to be used with other calibration data sets for other experiments. But because of the ease of use and adaptability of this calibration technique, it has consistently been the in-situ calibration of choice for FCR experiments.

2.6. Inconel 718

Through previous research, various materials have been selected to analyze scalability between experimental and engine conditions. Of those materials, one that is frequently seen and will also be used for the current research, is the high-conductivity, nickel alloy Inconel 718. In large part, the reasoning behind why Inconel 718 is a top choice for film cooling experiments is how its conductivity changes with temperature.

Inconel 718 is also metallurgically similar to typical turbine materials, which allows the Biot number to be approximately matched to real hardware. The ratio of thermal conductivity of air to the thermal conductivity of Inconel 718 stays relatively constant along the temperature range from room to engine conditions, which quantifies as about a 2.5x linear increase over this range for both. This relationship makes Inconel 718 a great material for scaling experiments, allowing for the matching of many terms discussed so far, such as Reynolds number, adiabatic effectiveness, and Biot number. While matching Re, Pr, and Nu for the coolant and freestream, along with absolute temperature and blowing ratio, an Inconel 718 conjugate heat transfer experiment should be fully scalable within reasonable uncertainty [7].

An additional advantage of Inconel 718 is that it is a highly thermally conductive material, allowing for increased performance in overall effectiveness compared to a non-Biot number matched or nonconducting material. Albert et al. investigated adiabatic and overall effectiveness between low and high conductivity materials. Found that adiabatic effectiveness was greatest in magnitude immediately downstream of the coolant holes for the low conductivity model. But the high conductivity model, which also matched Biot number, had much more uniform spanwise effectiveness due to conduction along and through the surface [8, 13].

3. Experimental Methods

The research was conducted utilizing the Film Cooling Rig (FCR) within the Combustion Optimization and Analysis Laser Laboratory (COAL Lab) located at the Air Force Institute of Technology (AFIT). The FCR was originally designed for reacting flow investigations, but has been previously modified to run heated and cooled air for the current investigation. For this investigation, the majority of the overall rig was kept the same.

The current research focused on scaling and comparing film cooling overall effectiveness among various temperature regimes, with the ultimate objective of relating experimental results to a turbine blade at operational engine conditions. The airfoil model was designed as a scaled down version of a larger model from previous research to analyze geometric scalability. Most of the changes made pertained to the airfoil design and coolant flow within the test block section to aid in matching and validating the experimental data for engine conditions.

The large scale facility that the current research modeled off of is described in Section 3.1. Section 3.2 covers the FCR facility itself, where Section 3.3 outlines the FCR test section in more detail. The test setup is covered in Section 3.4. Section 3.5 describes the computational analysis. Lastly, Section 3.6 reviews repeatability and Section 3.7 outlines uncertainty.

3.1. Large Scale Facility

The large scale film cooling rig used by Bryant [23] served as a reference for both geometric and temperature scaling. The model consisted of a semi-cylinder leading edge

with a flat afterbody. Figure 6 shows the front and cross-sectional views, with the specific pertinent measurements given in Table 1 and scaled measurements for the current research defined later in Section 3.3.2. Bryant's rig consisted of a full coverage leading edge coolant hole configuration in a staggered array with a total of 42 holes. Her model also used an interchangeable impingement plate design, and from her results, the most effective impingement plate design with three rows of 20 holes was selected for the current research.

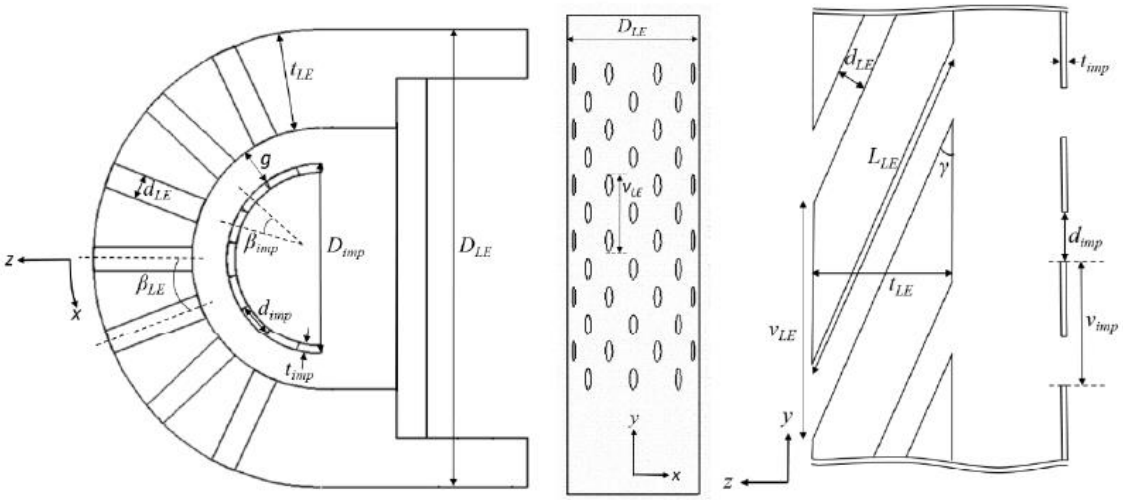

Figure 6: Large scale schematic views [23]

Table 1: Bryant model dimensions

LEADING EDGE			
OUTER DIAMETER	D	8.89	cm
COOLANT HOLE DIAMETER	d	0.48	cm
WALL THICKNESS	t	1.93	cm
INJECTION ANGLE	γ	20	deg
ANGULAR SPACING	β	21.5	deg
HOLE SPACING	v	3.78	cm
HOLE LENGTH	L	5.61	cm

Bryant's rig was situated as a true two-sided airfoil within its wind tunnel. AFIT's small scale rig used in this research was geometrically scaled down to 1/9th the size of Bryant's rig, but was designed as a single-sided airfoil with an underside bypass to

mimic a split flow around an airfoil due to the available facility. While AFIT's setup is outlined in Section 3.3, Figure 7 shows a diagram of Bryant's rig. The IR camera viewed one side of the leading edge, while a thermocouple measured the freestream temperature on the other, and a pitot-static probe to measure the freestream pressure.

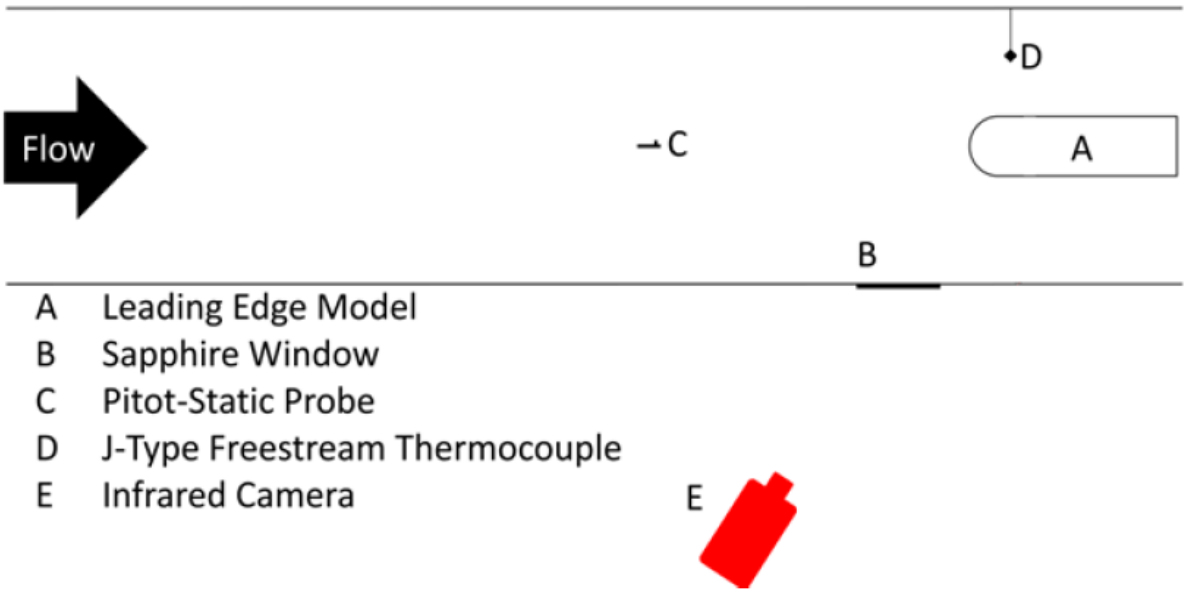

Figure 7: Large scale test section schematic [23]

Bryant's tests were conducted in the 300-320 K freestream temperature range with blowing ratios of M = 0.25, 0.5, and 0.9. Her coolant temperature could reach as low as 270 K, but the actual temperature during testing was not explicitly specified. Overall effectiveness at these three blowing ratios with the 20-hole impingement plate is shown in Figure 8. Without ingestion, Bryant was seeing overall effectiveness values between 0.55-0.85. In this setup, only the coolant hole inlets and the impingement plate holes on the stagnation row lined up, causing an increase in film effectiveness for this row at M = 0.9. Ingestion at the stagnation row occurred at M = 0.5, however, with increased ingestion into the next most central row on each side of the stagnation row at M = 0.25.

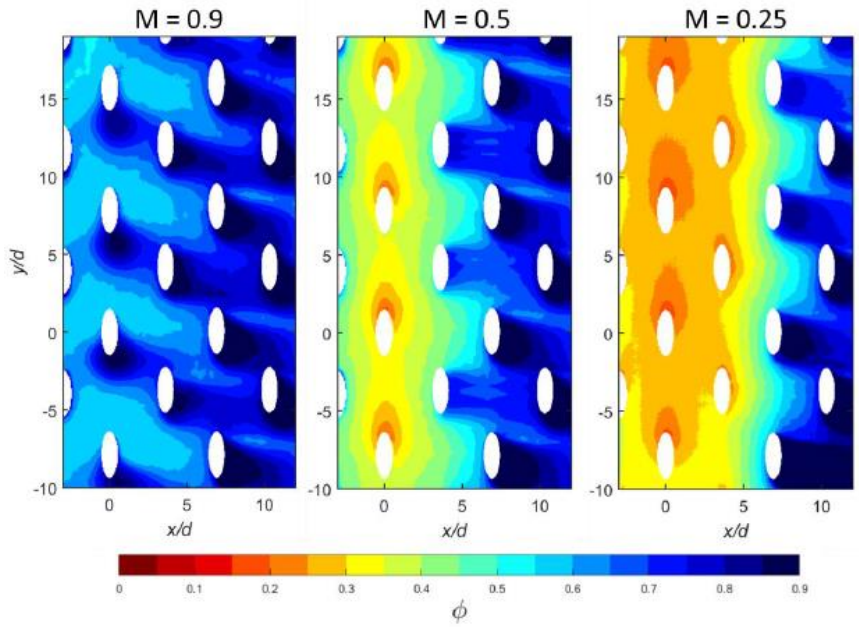

Figure 8: Overall effectiveness contours with 20-hole impingement plate [23]

AFIT's COAL Lab FCR facility aimed to replicate and scale down the work done by Bryant. By using a geometrically scaled down model of Bryant's setup, the current research aimed to create similar overall effectiveness contours in increased temperature regimes by matching flow conditions. In doing so, scalability of film cooling performance between experimental and operational conditions could be achieved.

Vorgert [21] and Tewaheftewa [12] had started this scaling process through various iterations of development. Vorgert's model was a one-sided airfoil model with a bleed slot. That initial bleed slot did not create an ideal flow split, however, so Tewaheftewa incorporated a bypass channel under the airfoil model to accomplish the boundary layer bleed along with a flow split to better replicate Bryant's two-sided model.

3.2. COAL Lab Facility

AFIT's COAL Lab FCR facility was designed to simulate a simplified, cooled turbine blade in a hot freestream environment. A schematic view of the airflow path

feeding the FCR is displayed in Figure 9. The air supply and selection valves are outlined in Section 3.2.1. Section 3.2.2 describes the air line and corresponding controls and heaters used for the freestream flow, while the coolant line and controls are detailed in Section 3.2.3. The FCR itself will be discussed in Section 3.3.

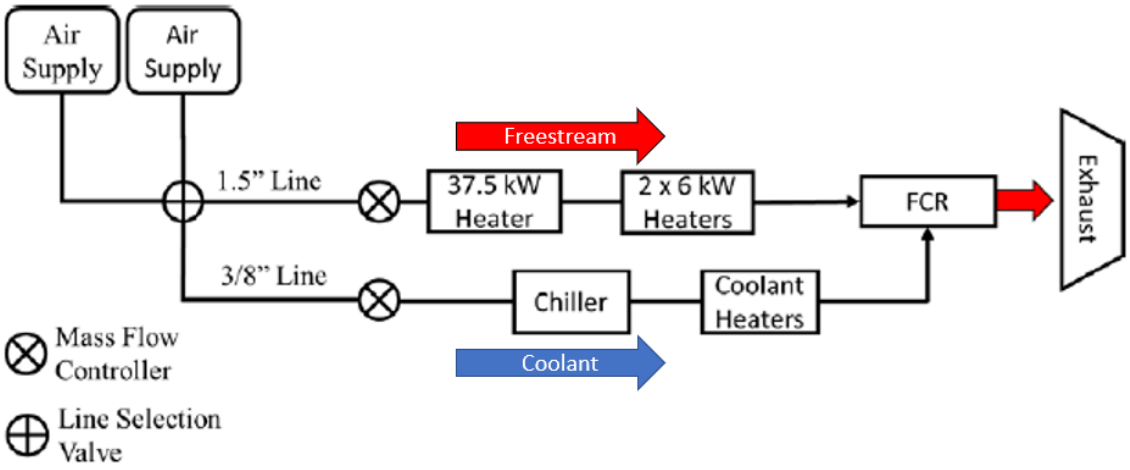

Figure 9: AFIT Film Cooling Rig diagram [12]

3.2.1. Air Supply

The current setup solely used heated and cooled air to reduce variables for examining film cooling methods. The COAL Lab had access to two different air sources, the shared building air line and a dedicated compressor for the lab. The AFIT shared line was powered by two Kaeser BSD-50 air compressors and were available to be shared among the neighboring labs to the COAL Lab. During previous years' testing, large drop-offs in air flow were sometimes experienced when using the shared air line [12]. The actual cause was never discovered, but it was possibly due to more than one lab utilizing the flow at a given time. Developed mainly for the Ultra Compact Combustor (UCC), which shares the COAL Lab space with the FCR, a compressor system dedicated to the COAL Lab was installed by Parks [31]. This dedicated system used an Ingersoll

Rand H50A-SD compressor and two vertical dryers to remove moisture from the air. Further specifications can be found in Tewaheftewa [12] or Damele [20], but this compressor was capable of providing more than enough airflow to the FCR and remain mostly steady.

The line selection valve in Figure 10 was used to select which incoming air source was to be used and then route the air to the desired lines for testing. The 1.5" air line was used for the freestream flow, and the 3/8" line was used for the coolant flow. Typically, the dedicated compressor was utilized when conducting tests to reduce the possibility of the significantly fluctuating airflow that was experienced previously.

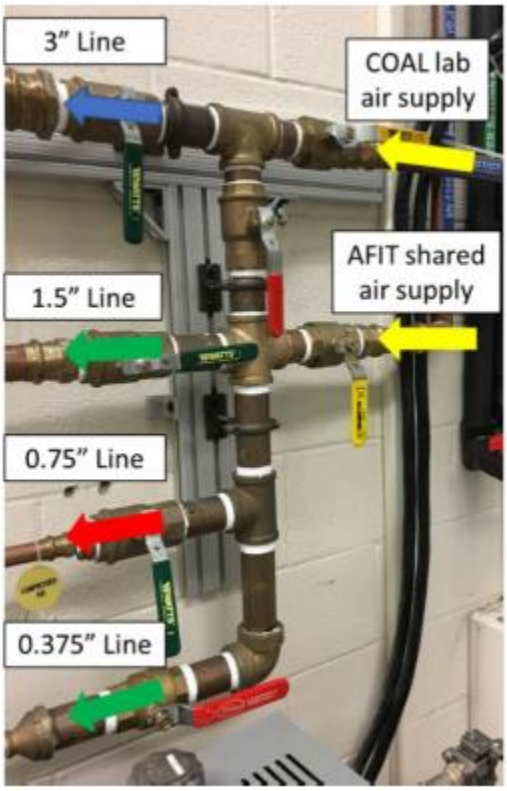

Figure 10: Manifold of line selection valves [12]

Once the desired air source was selected, air was brought in to the FCR through two different lines, outlined in Figure 9, one to the heaters for the freestream and the

other to the chiller for the coolant. Due to the freestream and the coolant having their own flow rates and temperatures, a separate series of temperature and flow controls was required for each.

3.2.2. Freestream Air Line

The freestream flow control setup consisted of an air-powered solenoid valve, pressure regulator, flow meter, and flow control valve, depicted in Figure 11. The solenoid valve was controlled by the same LabVIEW user interface program used by Vorgert [21] and Tewaheftewa [12], but the layout of some of the controls was modified from previous years for more efficient use. The air travels from the solenoid to a Fisher 299h pressure regulator to establish the pressure necessary to achieve the desired mass flow, which that mass flow is then measured by a Fox Thermal Instrument, Inc. FT2 flow meter. The freestream flow rate was controlled by a Eurotherm 2404 process controller in tandem with a FlowServe MaxFlo 3 control valve, rated for a maximum flow rate of 0.3 kg/s [12, 21].

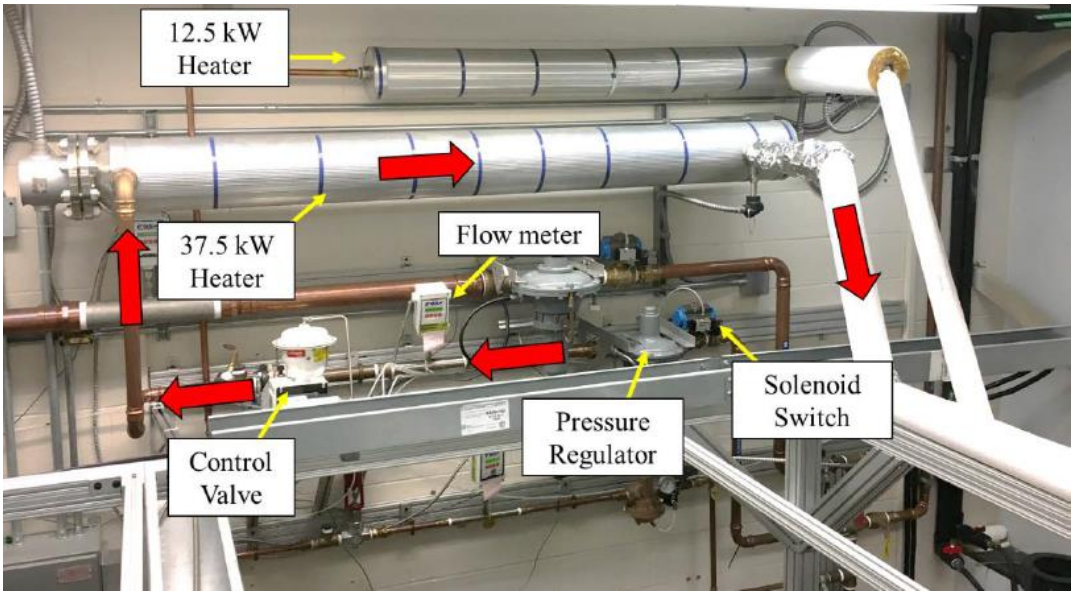

Figure 11: Freestream support equipment and flow path of 1.5" air supply line [12]

The 1.5” line was routed to the series of heaters to heat the freestream flow that the airfoil test section encountered. A 37.5 kW Gaumer Process heater mounted on the wall, identified toward the top of Figure 11, was first used to warm the air up to about 420 K before sending it to subsequent heaters. The Gaumer Process heater was powered and controlled by a wall-mounted Gaumer control box and operated by entering the percent of full power desired instead of a temperature input. Being a percent power input, the resulting temperature varied depending on the air flow being run through it. This type of command and lack of other feedback resulted in a longer time required, up to an hour, to reach a steady state temperature.

Two 6 kW Osram Sylvania electric heaters were located just before the main rig and created the additional heating necessary for the test runs. The two Osram Sylvania heaters, pictured in Figure 12, were decided on after a selection and installation process by Tewaheftewa [12] on account of expected flow rate and temperature goals of being able to heat 2260 SLPM total flow to 523 K from room temperature. Each of these heaters took about half of the flow, further heating it from 420 K to a projected 650 K right before entering the FCR test section.

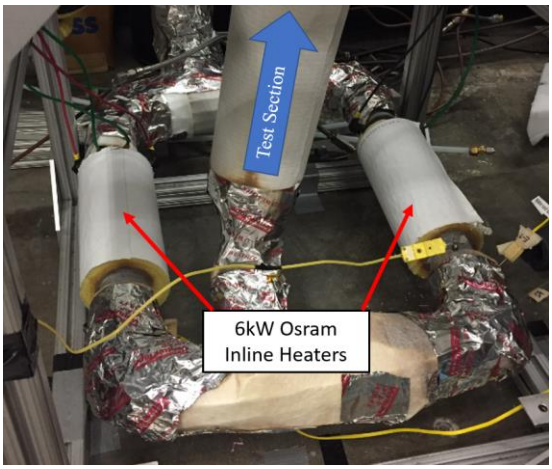

Figure 12: 6 kW Osram Inline Heaters

The two Osram inline heaters, as opposed to the Gaumer Process heater, were controlled by a newer digital temperature control that provided the set and real time temperature being output by the heaters in units of Fahrenheit. Mounted on the main rig structure just left of the rig and flow controls, the controller could input the desired temperature using the up and down arrows. When running, the inline heaters were able to create a faster response time and achievement of freestream temperature within minutes, but 10-15 minutes for the model to reach a steady-state temperature still remained for the model and test section materials to reach a steady-state temperature, as well. These heaters were downstream of the Gaumer wall heater and could adjust themselves automatically to achieve the desired temperature. This was done by continually sending commands and receiving feedback responses from a 0.125" diameter thermocouple placed behind one of the heaters. Because each of the two heaters took half of the flow and could work in parallel, the time for the heaters to reach a desired temperature was notably decreased to about 5-10 seconds.

The air then traveled vertically up from the inline heaters, through a 45.7 cm long flexline from Main Line Supply, to what has been dubbed the toroid bypass with its surrounding mounting assembly in Figure 13. This section was the remnant of the Well Stirred Reactor (WSR) used in a previous iteration by Ashby [22] to increase the freestream temperature, but created combustion products within the test section. This has since been disassembled and adapted to the test section by Tewaheftewa [12] because the new heat sources were added and no longer needed the WSR to meet the temperature goals, which were within the 650 K capability of the new heaters.

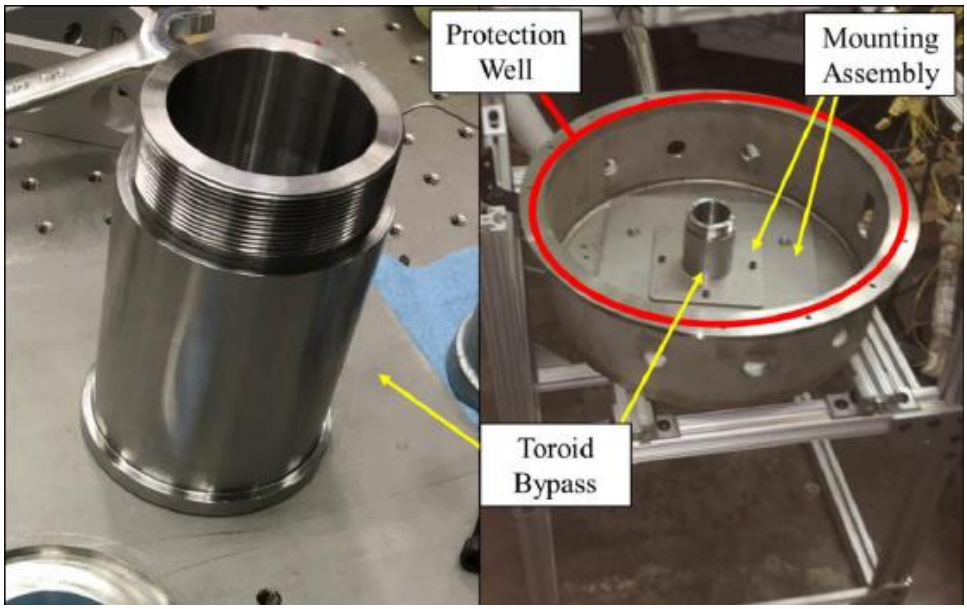

Figure 13: Toroid bypass (left) and mounting assembly (right) [12]

The heated air then traveled through an aluminum transition stack, pictured in Figure 14. A previous stack first consisted of a steel chimney outer shell with a ceramic inner core that changed from a circular to rectangular duct. The current stack serves the same purpose, but was made entirely out of aluminum. The stack changed from a circular pipe with a 49.5 mm diameter to a rectangular duct that is 50.8 mm wide and 25.4 mm tall, matching the shape of the test section entrance.

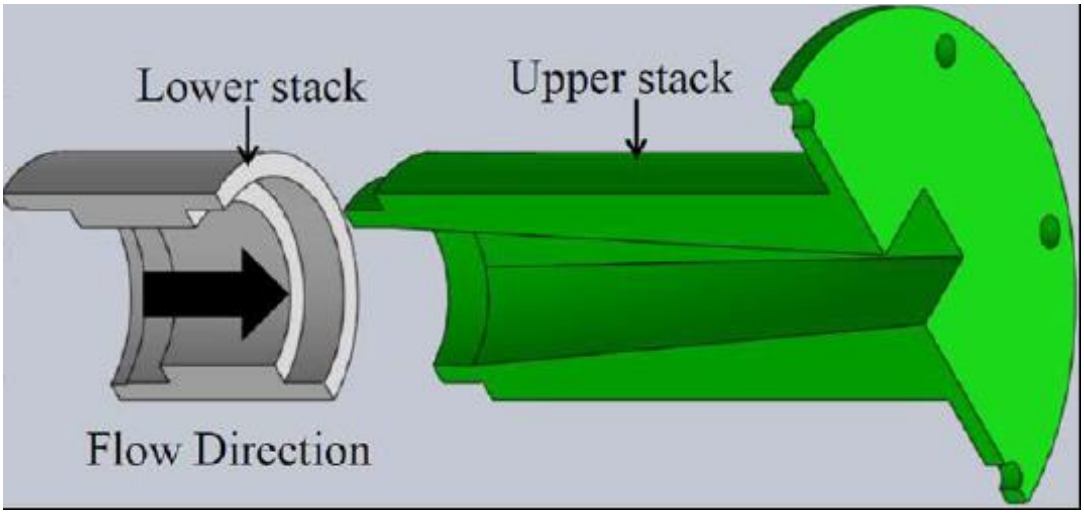

Figure 14: Aluminum transition stack [12]

The air then traveled through the FCR test section, described in detail throughout Section 3.3, and was exhausted out of the lab. An 18-inch diameter exhaust system was in place above the FCR exit to actively route the hot air from the lab environment. The exhaust fans within the system ensured a continuous exhaust flow and prevented any back pressure behind the test section exit.

3.2.3. Coolant Air Line

As shown in the diagram in Figure 9, the facility's 3/8" air line was used as the coolant line. A Valtek pressure regulator was used to control air pressure, and the flow rate was controlled by a MKS MC20A mass flow controller, managed by a MKS Model 647 C multi gas controller. The temperature is controlled by two inline electric heaters, a 1200 W OMEGALUX AHPF-121 and a 400 W OMEGALUX AHPF-061, and a Cole-Parmer 1C6 cooling and heating circulating bath. The two inline heaters were controlled by two Dart power controllers, shown in Figure 15, and the chiller unit had its own temperature control system.

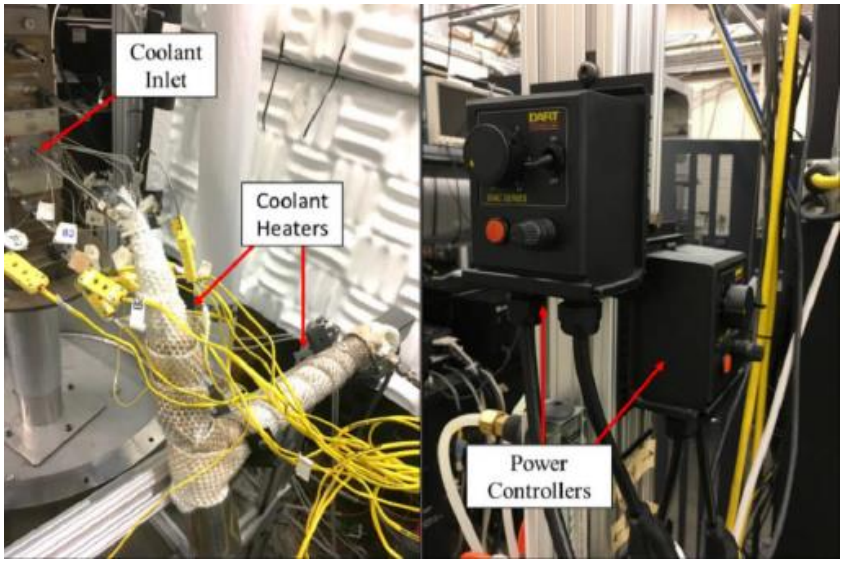

Figure 15: OMEGAFLUX heaters (left) and power controllers (right) [12]

In previous testing, the coolant temperature could reach 600 K with the 1200 W heater alone, and a maximum temperature with both heaters was never determined [22]. The 600 K temperature previously reached was more than sufficient for the range of this testing, which did not include coolant temperatures greater than 500 K. While the chiller had the ability to produce coolant fluid temperatures as low as 253 K, the lowest coolant temperatures observed were no lower than 283 K [12], measured just before entering the coolant block. The coolant temperature entering the rig was also influenced by the temperature regime the rig was operating in for testing, which was a factor to be accounted for by redesigning the coolant's path through the coolant block, further discussed in Section 3.3.2.

3.3. Film Cooling Rig Test Section

The FCR is a test rig used for scaling effects from a range of experimental to engine operating regimes. It is capable of operating at both high and low temperatures and can be used with multiple gases for the freestream and coolant flows. The rig was designed for the ability to be modified to reach a range of objectives. One main objective was scaling Bryant's large scale rig down to a 1/9th size. Her large scale rig operated at a lower temperature regime of 300 K and Re = 60,000 [23], based on leading edge diameter. Blowing ratio sweeps were conducted at greater temperature regimes to match back to trends identified by Bryant. Additionally, the large scale rig was a two-sided airfoil, where the FCR was one-sided, so area ratios at the model had to be matched along with introducing a bypass channel underneath the airfoil to achieve a proper flow split and allow setting of the stagnation point. The test section, shown in Figure 16, can be

broken down into three major sections: the main test rig, the test block, and the viewport. The main test rig, which consists of the freestream and bypass channels, transition wedge and bypass adjustor, and its slight changes will be discussed in Section 3.3.1. The test block underwent a series of design changes, along with creating of a new coolant delivery block and airfoil, and will be outlined in Section 3.2.2. Lastly, Section 3.2.3 will describe the various viewports utilized for flow observation.

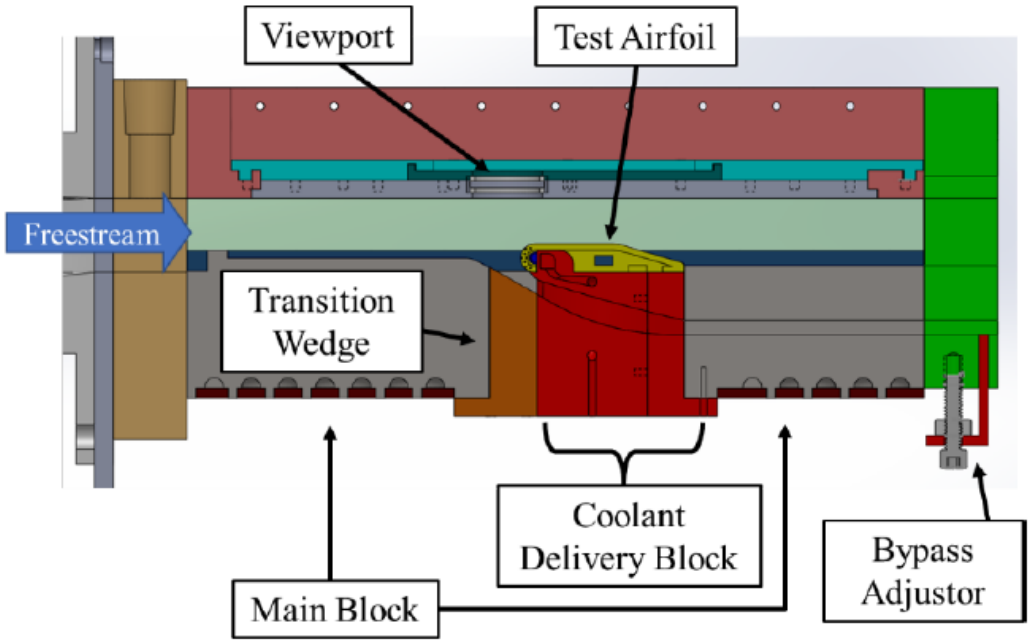

Figure 16: FCR Test Section [12]

3.3.1. Main Test Rig

The main test rig consisted of everything from Figure 16 that is not the viewport or the test block and airfoil. The rig was designed to replicate scaled conditions to Bryant, which had flow above and below the airfoil, and will be detailed further in this section. Figure 17 outlines the path the air flow took through the FCR. The freestream air entered the test section, hit the boundary layer trip, traveled either over the airfoil as the main freestream or split off down the boundary layer bypass, and exited out the back

end through the main flow exit or adjustable bypass exit. These components were designed by Tewaheftewa [12], but the layout and pertinent information will be discussed throughout this section.

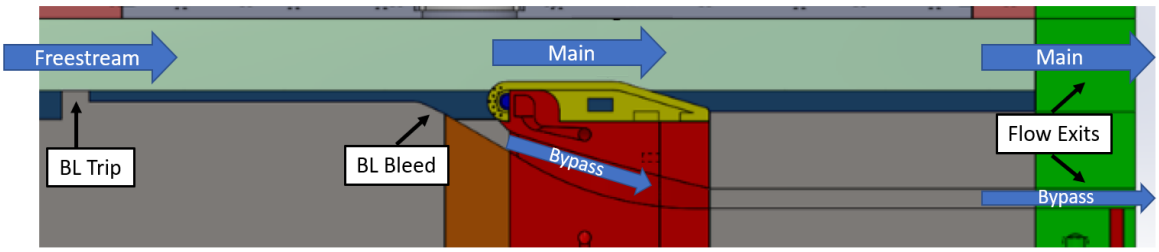

Figure 17: FCR flow path

The entrance of the freestream flow into the test section consisted of a boundary layer trip, shown in Figure 18. The trip itself was 4.3 mm high and 7 mm long, and 10.8 cm upstream of the airfoil. The channel height before the trip was 24.9 mm and 20.5 mm after, with 17.8 mm above the trip. The boundary layer trip was an important component because it allowed for a consistent turbulent boundary layer that could then be removed just before the airfoil at the boundary layer bypass, creating a more uniform freestream flow.

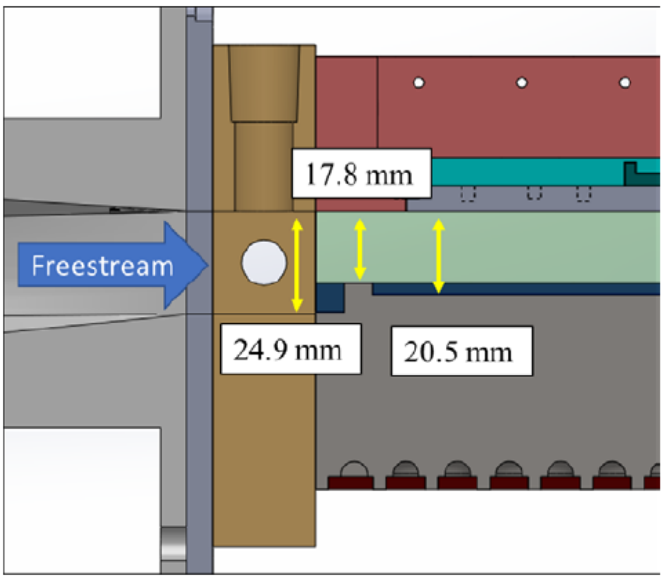

Figure 18: Entrance of freestream with boundary layer trip [12]

As stated previously, the freestream entering the test section split just before encountering the test airfoil, either going over the airfoil or beneath it through the boundary layer bleed slot in Figure 19. In addition to removing the turbulent boundary layer, the boundary layer bleed was created with the previous objective of matching the split flow around Bryant's large scale rig [23] while maintaining the freestream area contraction ratio above the model at 0.76. Accomplishing the proper split proved challenging, however, because Bryant's rig was a two-sided airfoil with an even flow split, and the FCR airfoil was a one-sided airfoil that had to be adapted with the bypass channel. The bypass channel allowed the flow split without the need to double the freestream flow rate. The area above the FCR airfoil was 787.4 mm^2 and the bypass channel area was 280.1 mm^2. While not an even flow split, the airfoil's location at the bottom of the test section would have helped account for that offset.

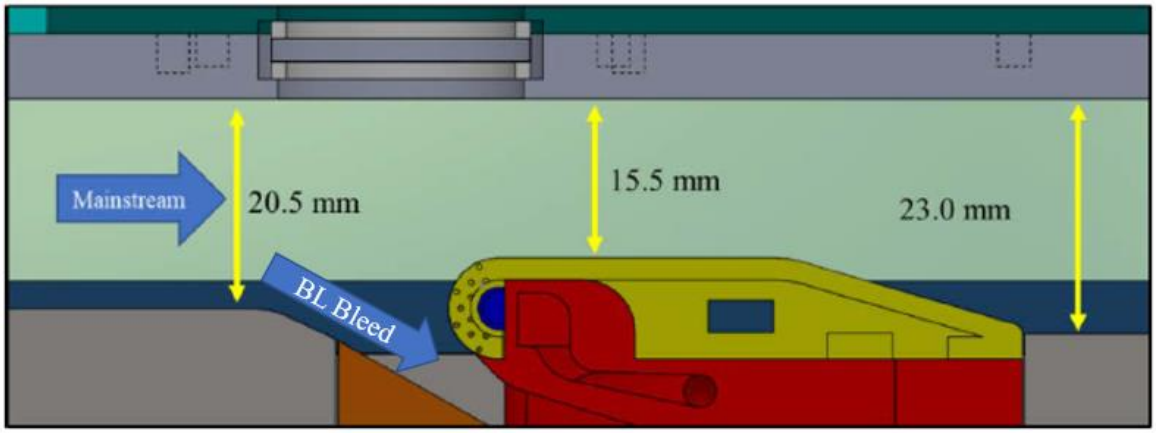

Figure 19: Test airfoil flow split, adapted from Tewaheftewa [12]

The contraction ratio (*CR*) of the test section, not accounting for the bypass channel, was matched to Bryant's large scale rig to have similar acceleration as the air flows over the model. Matching the ratio of the freestream channel to the area above the airfoil model aided in keeping the same flow acceleration between the two scaled models.

Along with the channel height measurements before and above the airfoil in Figure 19, a head-on view schematic with measurements is given in Figure 20 for both Bryant's large model and the FCR model. Both include the wind tunnel height and width at the airfoil, h_{WT} and W, and the leading edge diameter, D_{LE}. The height of the test section above the airfoil model, h_{TS}, is also given, as that is a one-sided model that sits on the bottom of the wind tunnel for the FCR. The *CR* here is the ratio of the area above the airfoil to the area just upstream of the airfoil in the wind tunnel. A_{WT} for the large scale rig was 1494.1 cm^2 and A_{TS} was 1133.1 cm^2, leading to a *CR* of 0.76. The current location of the airfoil and freestream channel height was set by Tewaheftewa in order to match this ratio. The resultant A_{WT} was 1041.4 mm^2 and A_{TS} was 787.4 mm^2, leading to a matched *CR* of 0.76.

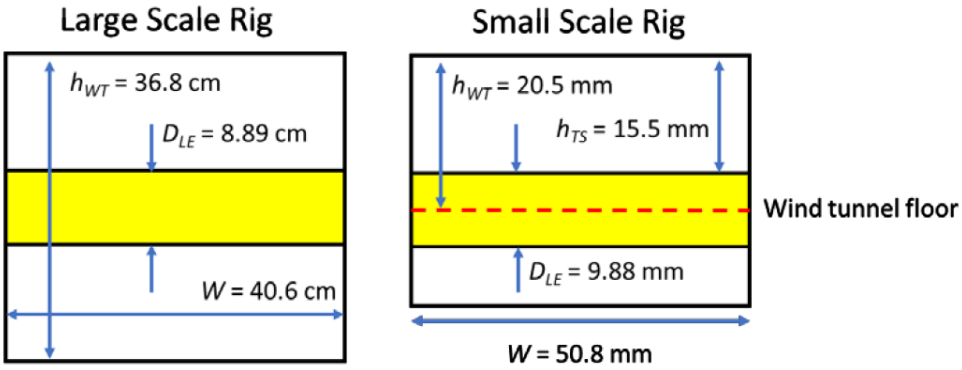

Figure 20: Head-on view of rig flow areas [12]

In conjunction with the design changes for setting the *CR*, the airfoil location was also lined up such that the center row of coolant holes would be directly in line with the bottom of the freestream channel, assuming that the bypass under the airfoil would result in a stagnation point and flow split at that central row of holes. The bypass channel incorporated an adjustor at the exit, pictured in Figure 21, that could control the amount of flow through the bypass channel, thereby allowing some control of the stagnation point to be above, at, or below the central row of holes.

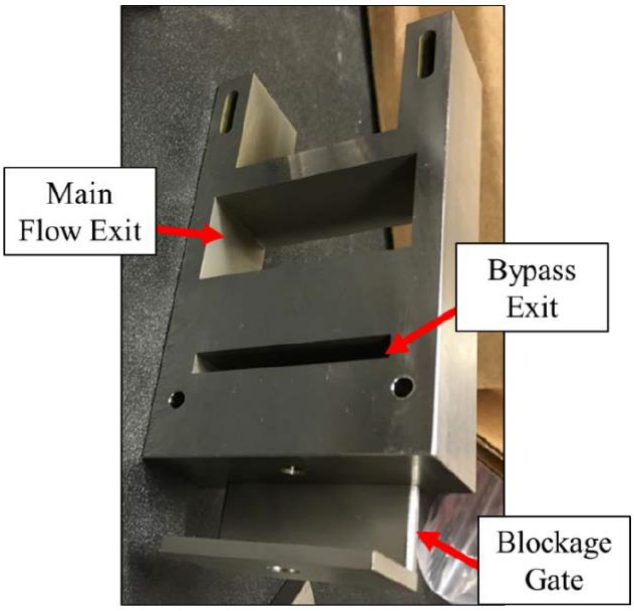

Figure 21: Bypass channel adjustor [12]

The bypass channel served the purpose of simulating a full wind tunnel without doubling the freestream flow rate, as well as providing more control over the stagnation point location on the airfoil. The stagnation location could be shifted between the central and first rows of holes by controlling how much air went through the bypass using the bypass adjustor at the FCR exit. The process of finding this stagnation point will be discussed further in Section 3.4.1. The bypass channel also decreased the amount of conductive heat transfer that was possible from the airfoil to the rest of the rig, which allowed for more accurate assessments of overall effectiveness. During his examinations, Vorgert [21] used a one-sided airfoil that effectively sat on the bottom of the test section. This situation created a conduction path between the airfoil and its surroundings that was not accounted for, even without coolant flowing, and resulted in consistently higher overall effectiveness results of about 0.6 at the higher temperature regimes compared to the lower temperatures because more heat was released to the surroundings during the

high temperature testing. Although no coolant was flowing, the T_c temperature was used to calculate ϕ because the internal coolant plenum still had a temperature difference for within the model as opposed to out. This phenomenon was also observed at $M = 0$ for the four temperature regimes investigated during this research and will be examined further in Section 4.4.1.

3.3.2. Test Block

A number of changes were made to the test block section of the FCR, which consisted of the test airfoil and coolant delivery block. Nathan Clark was integral in handling the design and CAD drawings for the new, redesigned airfoils and test blocks, along with aiding the coordination of parts manufacturing and initial shakedown runs. Changes were made to the airfoil from the previous iteration to include allowing better visibility of flow development by the IR camera and more accurate hole drilling for better geometric scaling. The coolant delivery path through the coolant block was also redesigned in order to decrease the amount of heating the coolant experienced as it traveled through the block before reaching the airfoil. The changes to the leading edge airfoil model will first be outlined, followed by new coolant delivery block designs, including a design with an impingement plate integrated into the block, which is outlined in Section 3.3.2.1.

3.3.2.1. Leading Edge Test Block

Part of the experimental objectives focused on geometric scaling of film cooling of a turbine blade leading edge model. A new film cooling airfoil was created by Tewaheftewa and then slightly modified for this iteration. The airfoil model created was

aimed at scaling to the semi-cylinder leading edge model used by Bryant, which was a model scaled up by a factor of 9. The airfoil was constructed and milled at the AFIT machine shop with Inconel 718 stock from Rolled Alloys, Inc. Using a typical hole configuration for this area, and following from the cooling hole scheme used by Bryant outlined in Section 3.1, seven staggered rows of six cylindrical cooling holes each were used for this testing as shown in Figure 22.

Figure 22: Leading edge airfoil model

Most dimensions remained the same from Bryant's design, which are defined in Figure 25 and summarized in Table 2. Table 2 lists the dimensions of Bryant's model, the target scaled value, the actual value, and scale factors for the geometric measurements. The main difference from Tewaheftewa's design was an overall spanwise shift of the leading edge holes by one pitch, depicted by the green dots in Figure 25. Because the cooling holes have a spanwise injection angle of 20˚ and therefore require room for the film to fully develop, this shift would allow a larger portion of that usable, developed flow data to be collected by the IR camera's viewing area, represented by the red oval. In an example of Tewaheftewa's flow results in Figure 23, Section 2 was the most developed section that was fully visible, but it had different flow characteristics from Section 1 for the corresponding areas. While he used Section 2 as the best data set,

it was reasoned that shifting the hole configuration down would reveal the next section, which would ideally be more identical to the section before it.

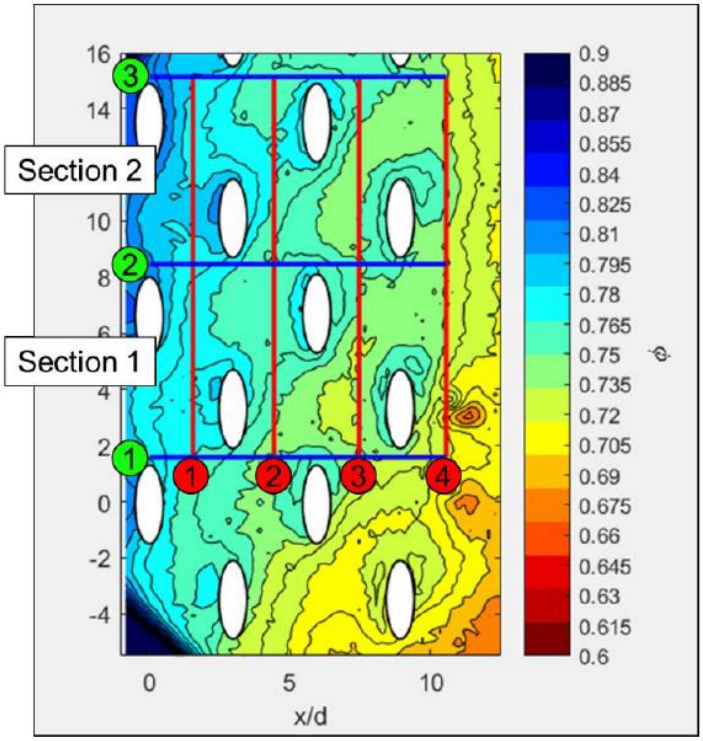

Figure 23: Previous flow development layout [12]

After the pitch shift, flow development was again analyzed. The layout and results of the three spanwise pitch sections are shown in Figure 24. The difference between Sections B and C was less then A and B, showing that the flow development was beginning to level off even if it had not yet fully been reached in the visible region. Because the next pitch section could not be seen in full, Section C was chosen for data analysis.

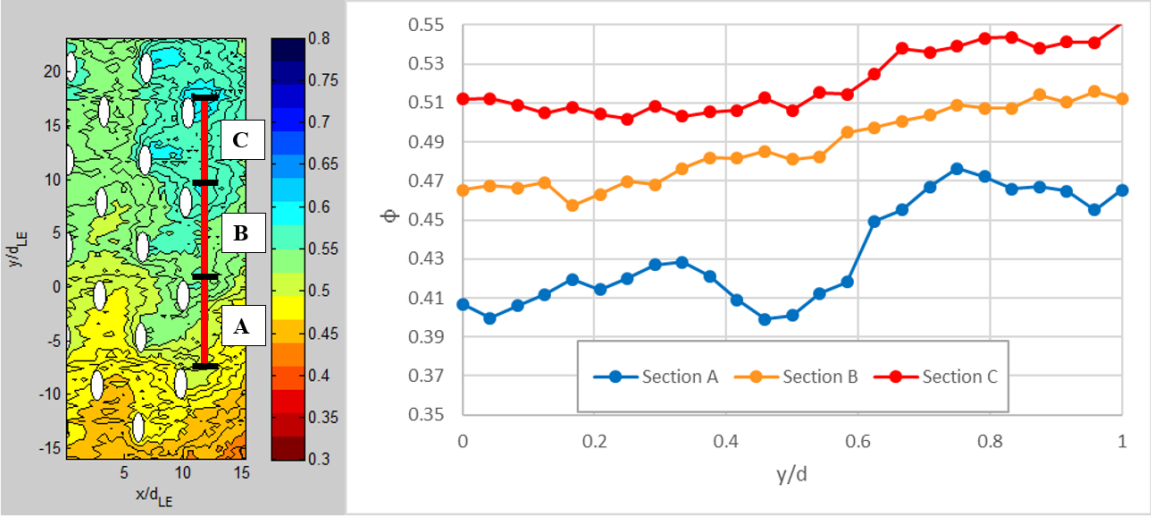

Figure 24: Leading edge flow development analysis

All other aspects and dimensions remained the same. The angular spacing, β_{LE}, between the coolant hole rows was 21.5˚, with the middle row being placed on the center of the semi-cylinder. The hole injection angle, γ, was 20˚ and oriented in the spanwise direction, resulting in a hole length, L, of 0.626 cm. The pitch, P_{LE}, and leading edge thickness, t_{LE}, were matched at 0.42 cm and 0.214 cm, respectively.

The cooling hole diameter, d_{LE}, was targeted for 0.533 mm, but resulted in 0.508 mm due to the drill bit size options available. The holes on the previous model by Tewaheftewa resulted in being tapered and too large at 0.622 mm due to some shaking during the manufacturing process. For this iteration, the ability to match the target value for the hole diameter exactly was limited by the availability of tooling and drill bits of such small magnitude, and shaking during drilling did not end up being an issue. A 0.020 in drill bit was chosen, with drilling done by the Air Force Research Lab (AFRL) model shop. With a leading edge diameter, D_{LE}, of 0.988 cm, the D_{LE}/d_{LE} came to be 19.44, 4.9% variance to Bryant's model. The percent difference in the L/d_{LE} value of 12.32 was also similar at 5.4%.

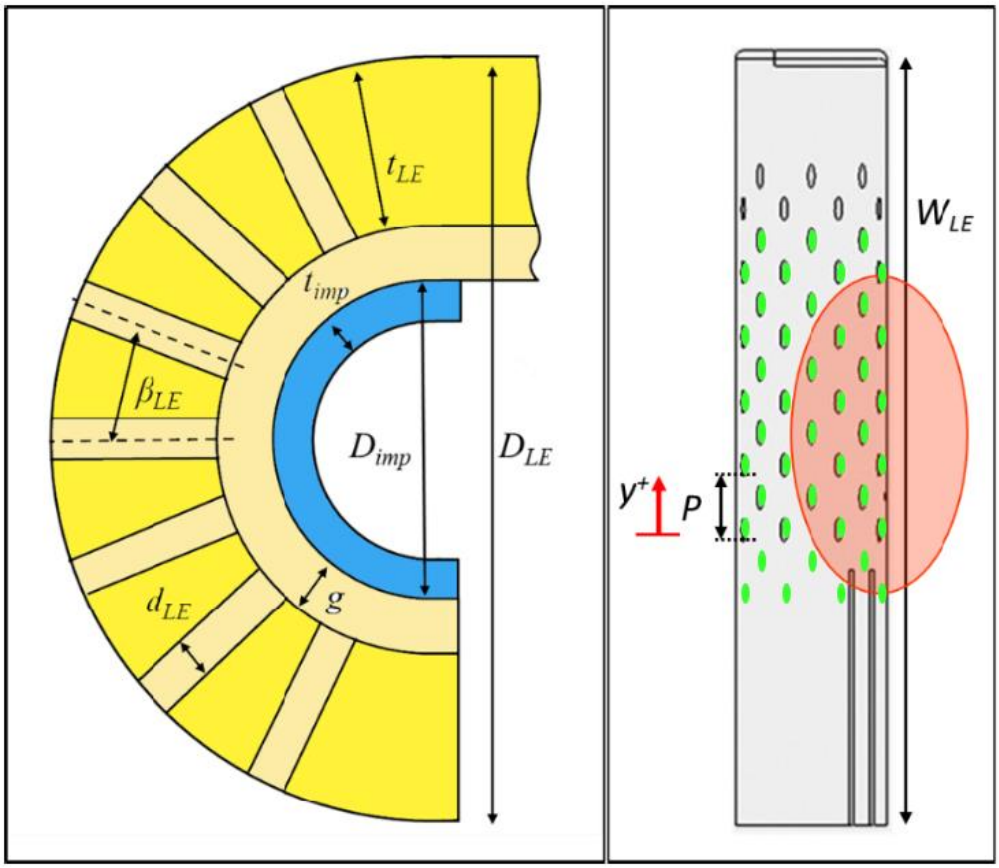

Figure 25: Leading edge dimensions and views, adapted from Tewaheftewa [12]

Table 2: Leading edge dimensions

Parameter	Large Scale Value	Target Scale Value	Actual Value	Actual Scale Factor
β	21.5˚	21.5˚	21.5˚	N/A
γ	20˚	20˚	20˚	N/A
d_{LE}	0.48 cm	0.533 mm	0.508 mm	9.45
D_{LE}	8.89 cm	0.988 cm	0.988 cm	9.0
D_{LE}/d_{LE}	18.52	18.54	19.44	N/A
L_{CH}	5.61 cm	0.623 cm	0.626 cm	9.0
L_{CH}/d_{LE}	11.63	11.69	12.32	N/A
P_{LE}	3.78 cm	0.42 cm	0.42 cm	9.0
t_{LE}	1.93 cm	0.214 cm	.214 cm	9.0
g	0.64 cm	0.71 mm	0.71 mm	9.0

The previous coolant block design used by Tewaheftewa was intended to be directly modeled after Bryant's large scale rig, but accessibility due to the smaller FCR

size and the existence of the bypass channel, discussed in Section 3.2.1., hindered creating a directly geometrically scaled design. Bryant's "soaker hose" design can be seen in Figure 26.

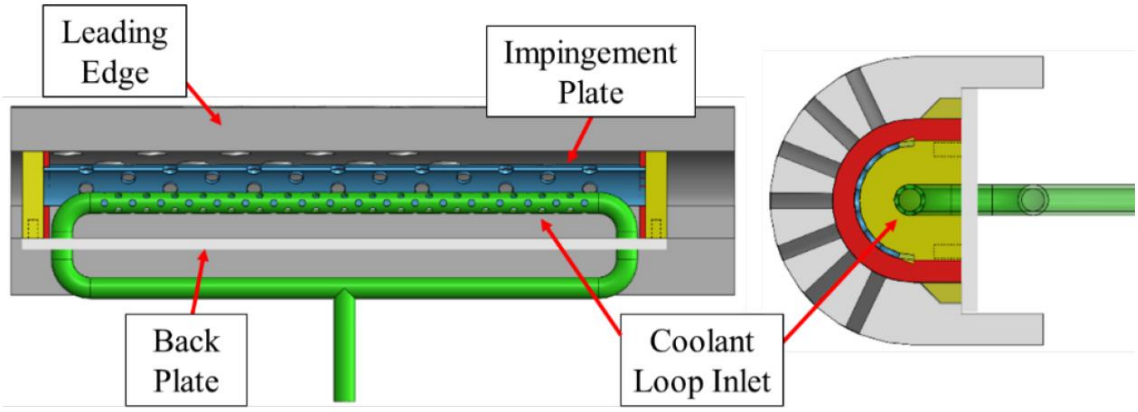

Figure 26: Bryant's coolant delivery design [23]

Tewaheftewa's design, in Figure 27, mimicked Bryant's design by the implementation of the soaker hose for coolant delivery. Routing around the bypass channel and through a highly conductive material, however, resulted in higher heat transfer to the coolant between entering the block and exiting out through the impingement plate, as much as 70 K.

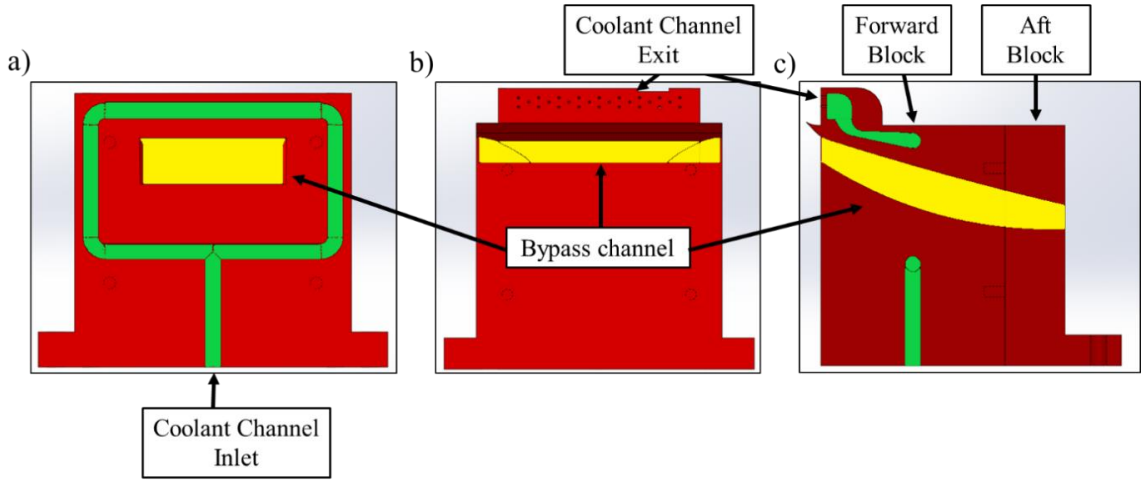

Figure 27: Previous coolant delivery design [12]

Because the coolant was already experiencing increased heating compared to Bryant's rig, it was decided to deviate from matching the internal coolant delivery in order to achieve cooler temperatures at the impingement plate. The large amount of surface area compared to the volume of coolant flowing through caused the coolant to be 74 K higher at the channel exit than it was upon entering the block at 292 K for Tewaheftewa's test cases at T_∞ = 400 K. A new inlet from the side of the block near where the bypass channel was located, shown in Figure 28, along with providing a larger area for the coolant to occupy within the block, was designed to reduce the unnecessary heating of the coolant before it reached the exit. However, it became apparent during testing that the new coolant delivery block performed worse, gaining over 100 K during similar tests at 450 K. Figure 29 shows the impingement coolant block, including the bypass channel and coolant inlet.

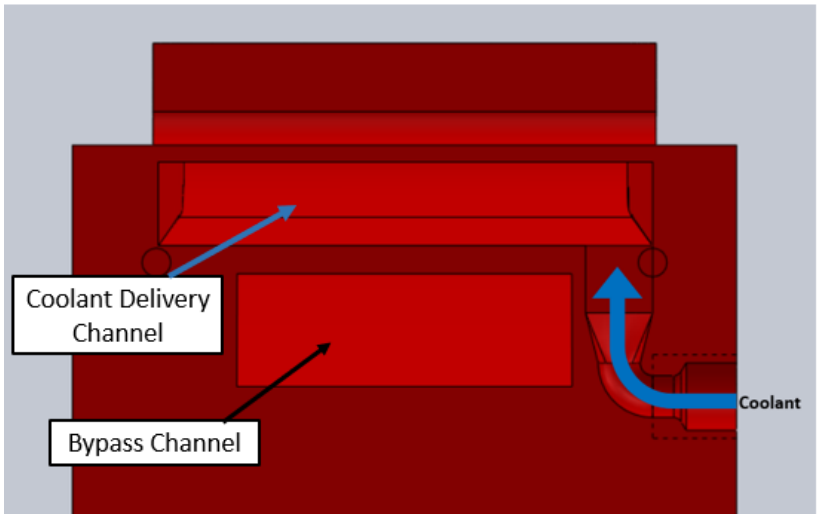

Figure 28: New Coolant Delivery Design

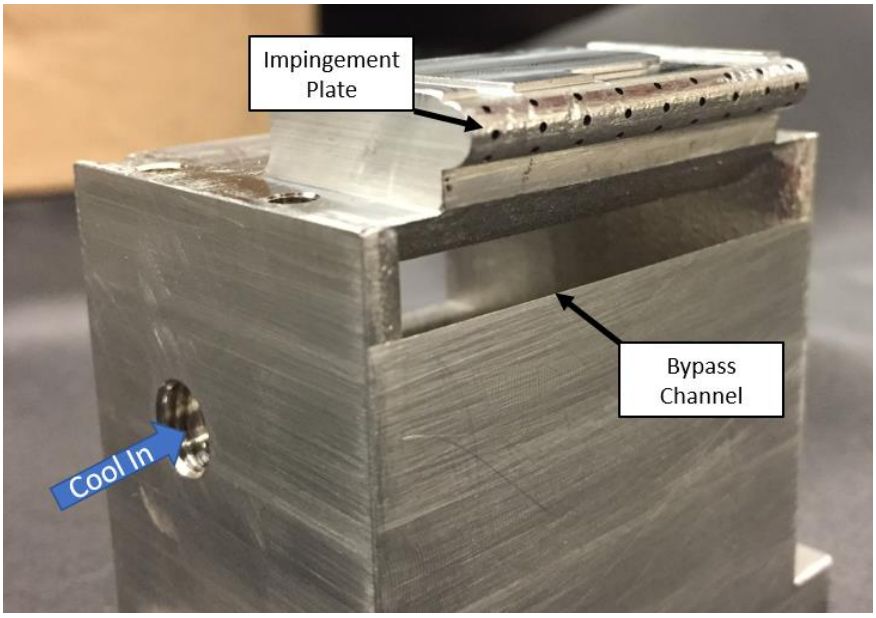

Figure 29: Impingement plate coolant block

3.3.3. Viewports

The viewport allowed for optical and IR access to the test airfoil through a circular window to work in conjunction with the thermocouple point measurements. This circular window could be made of sapphire, quartz, or silicon. A sapphire window provides best IR access, and so it was chosen for the purposes of this experiment. The viewport setup, shown in Figure 30, was the same as used by Tewaheftewa [12]. He had performed a redesign of the viewport assembly to result in a smaller void area below the window, decreasing from 15.3 cm^3 to 1.7 cm^3, but no design changes were made for this iteration. The aim of the redesign, however, was to reduce any impact to the freestream near the model as much as possible.

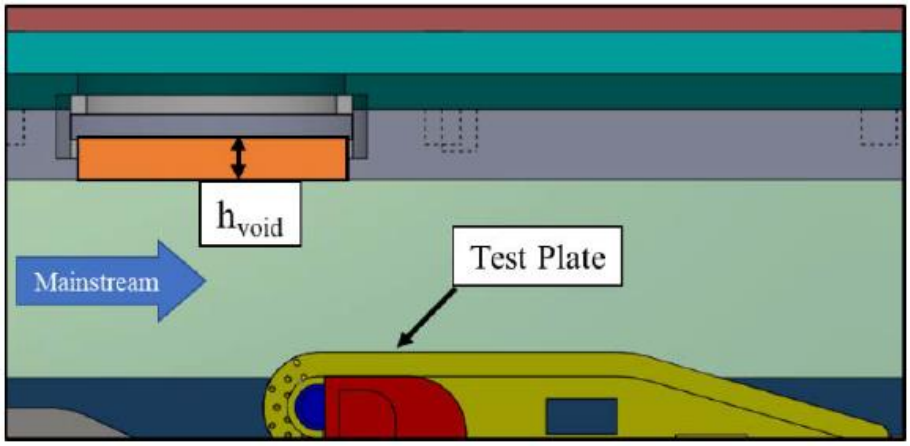

Figure 30: Viewport window and void cross-sectional view [12]

Figure 31 is a cross sectional view of the viewport assembly, and Figure 32 identifies each component. An assembly of multiple parts was required for viewing window location modularity. Due to the small size of the window itself, its location needed to be able to shift depending on which aspect of the airfoil was being investigated. For this investigation, the window had to be more upstream to view the leading edge and, conversely, further downstream to view the pressure surface. The bottom plate was the piece closest to the test model and fit the bottom side of the main block. It served the purpose of minimizing the void above the test section along with providing the hole for line-of-sight access to the test model. The window plate served the purpose of sandwiching the 25 mm diameter sapphire window against the bottom plate. Additionally, a high temperature RTV sealant was used around the edge of the sapphire window to further hold it in place and seal it off. Lastly, the sealer plate secured the bottom and window plates in place and also created an additional layer to minimize flow leaks out of the rig.

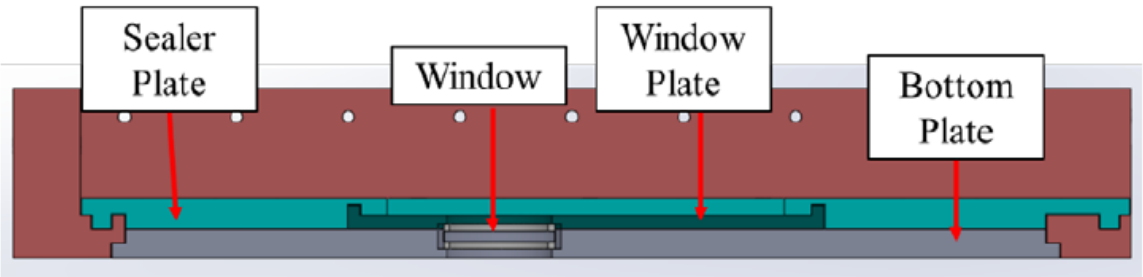

Figure 31: IR viewport assembly [12]

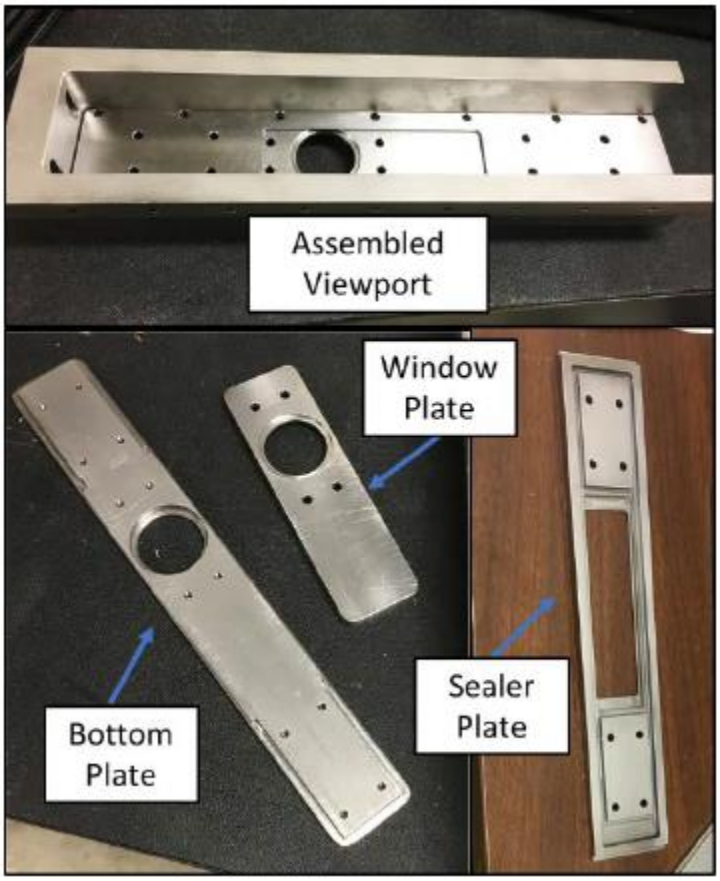

Figure 32: IR viewport assembly components [12]

Due to the nature of modularity and the clamping design, in order to move the window to a different location, the sealer plate must be removed and the window and bottom plates swapped out. Multiple sets of window and bottom plates were made with the window hole in different places to allow the IR camera to view different parts of the test model by changing its viewing angle. The full assembly and bottom plate designs

can be seen in Figure 33. The 65˚ view allowed for observation of the leading edge, while the 45˚ view allowed for observation of the downstream pressure surface. The blank plate removed the void created by the window but also blocked optical access. Figure 34 depicts the notional camera angles measured from vertical.

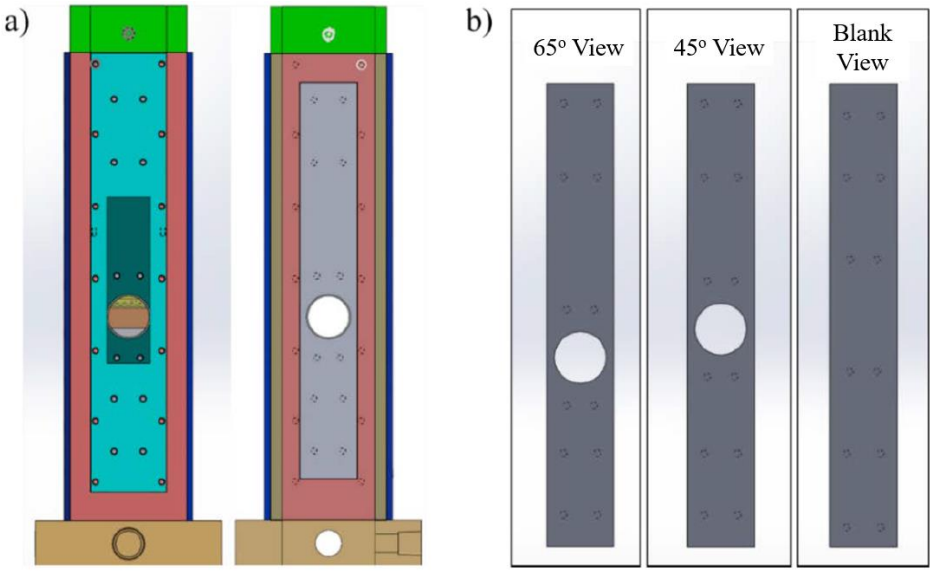

Figure 33: a) Assembled viewport (front and back) b) Viewport bottom plate designs [12]

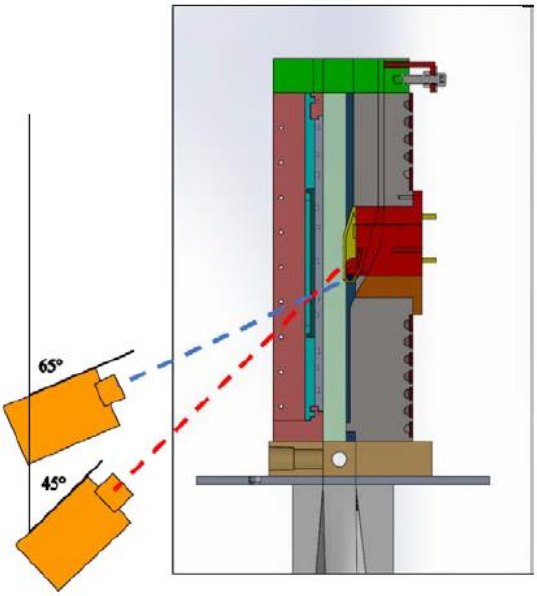

Figure 34: IR camera setup angles for pressure side (45˚) and leading edge (65˚) views [12]

3.4. Pressure Side Test Block

An additional objective originated from Honeywell to investigate shaped pressure side film cooling holes. Extra rows of film cooling holes are typically utilized to supplement the film protection initialized by the leading edge, but this investigation focused on a single row of coolant holes without the leading edge influence. Shaped coolant holes are more frequently used on these downstream rows than on the leading edge, and Honeywell has provided some hole geometries for investigation. Cylindrical coolant holes are typically used for simplicity, but these downstream regions are capable of incorporating shaped coolant holes to aid in slowing down and increasing spreading and mixing rates of the coolant with the freestream.

A typical turbine blade has a series of internal passages that feed the multiple rows of holes around the airfoil's surface. Figure 35 shows the geometry of a Honeywell airfoil, which was targeted to run at Re = 15,000, based on leading edge diameter. This investigation focused on the row of pressure side holes, located downstream of the leading edge on a flat portion of the airfoil. Because this row of holes was on a flat surface, flat interchangeable plates were able to be used for this investigation. To properly replicate the thermal environment around this hole, the u-bend of coolant flows 5 and 6 were replicated in the current investigation. A row of pressure side holes was modeled using a new airfoil and coolant block design, also manufactured out of Inconel 718.

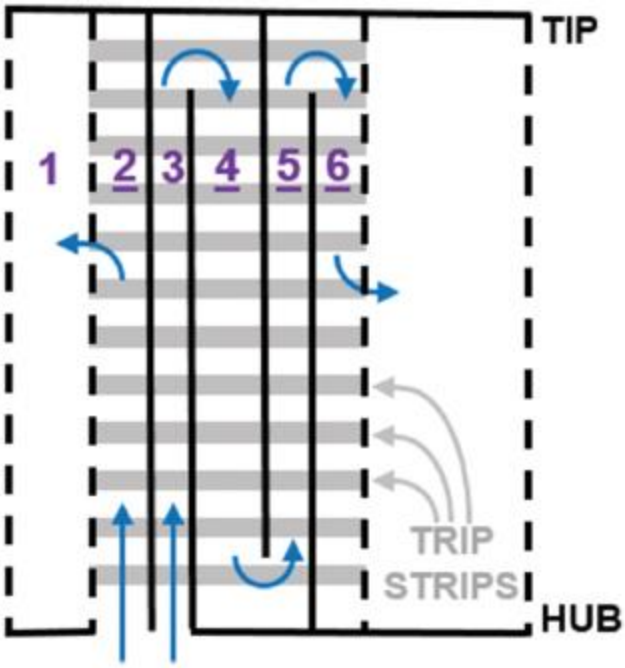

Figure 35: Schematic of internal passages [18]

Section 3.4.1 details the pressure side test model, including the coolant holes, airfoil, and coolant block. Section 3.4.2 describes how the test model was set up for instrumentation, where Section 3.4.3 outlines the coolant line configuration. Lastly, Section 3.4.4 is an overview of issues that were experienced with sealing the coolant channel within the test model.

3.4.1. Pressure Side Model

The three coolant holes tested for the pressure side row and their relative height and width dimensions are shown in Figure 36. Each hole had the same inlet diameter, and a pitch spacing of 6*d*. The fan shape resembled a cylindrical hole that was flattened out at the exit, and the duck foot was designed as three cylindrical holes converging midway through the hole with a slight offset to the left side.

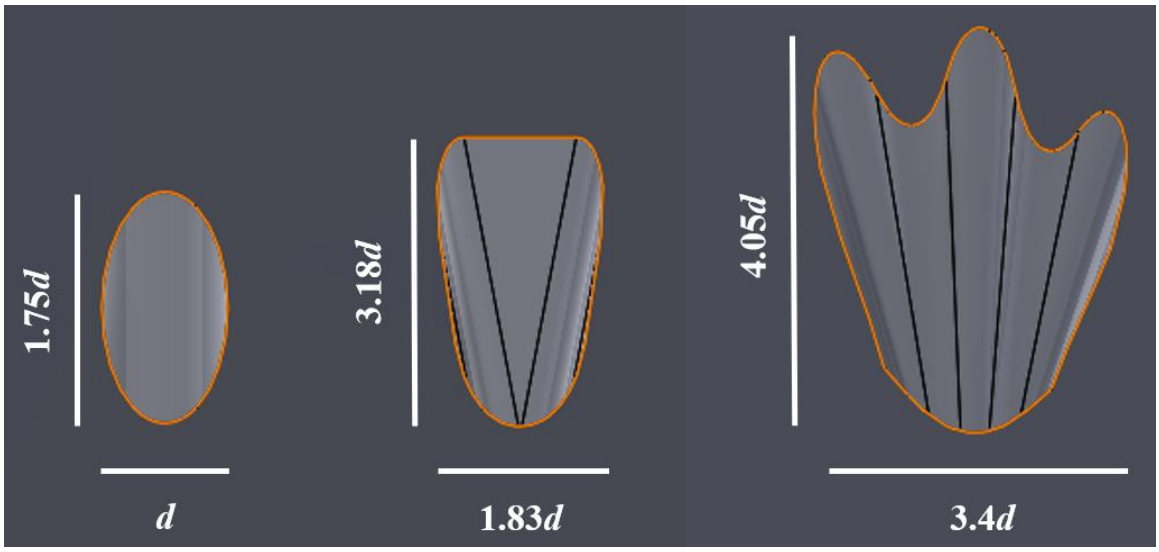

Figure 36: Close-up and dimensions of cylindrical, fan, and duck foot holes (left to right)

All holes for this design had the same initial injection angle to the freestream flow, which the cylindrical holes maintained through the exit. Figure 37 contains the side views of all three hole designs to highlight the injection angle and shape layout. Starting part of the way down the hole, the fan and duck foot holes were further laid back to about half of the initial angle to the freestream, allowing for better attachment to the surface after exiting. Shaped holes, to include the fan and duck foot, tend to create notable improvements by increasing the spreading ability of the coolant over the surface, creating a larger area of coolant effectiveness. Expansion of the coolant hole towards the exit before entering the freestream allows the coolant flow to slow down, creating a lower momentum flux, and therefore a decreased tendency to separate. This decreased tendency to separate can also allow for higher coolant flow rates [1].

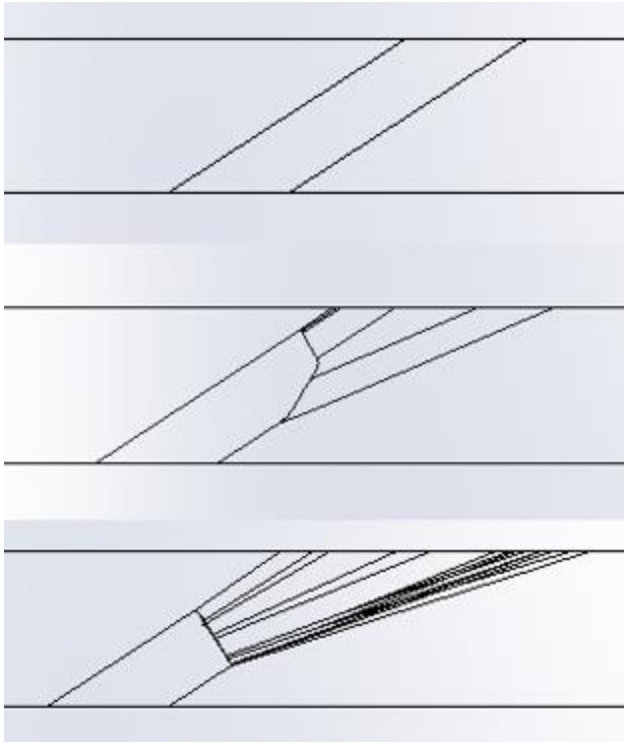

Figure 37: Coolant hole design side view, cylindrical (top), flat (middle), duck (bottom)

A test model was required in order to investigate the series of holes. Given the airfoil model of the FCR and coolant delivery system, the FCR test model was adapted and designed to test a pressure side row of holes. The new airfoil and coolant block used for the pressure side coolant hole row investigation are shown in Figure 38. The blade design provided by Honeywell had a row consisting of 16 holes, but due to width constraints of the test model, the number of holes was reduced to 12. Size and spacing were all kept the same, so the test performance would remain unchanged as long as the coolant flow rates were adjusted accordingly for the decreased number of holes. The airfoil was designed for the modularity of swapping out the separate plates with the various coolant hole shapes created for the investigation.

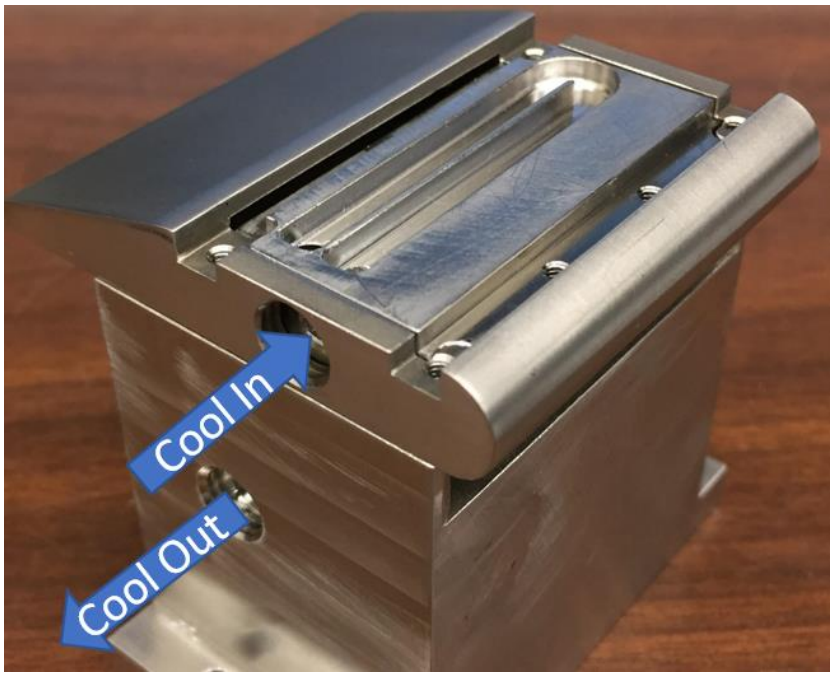

Figure 38: Pressure side coolant block and airfoil

The dimensions for the channel were also specified by the sponsor, with a divider in between, and are labeled in Figure 39. The area of the coolant channel was maintained down its entire length for consistent flow through all holes. The length of the channel extended beyond the row of holes on each end to allow for uniform flow across the hole inlets and to allow for thermocouple instrumentation. The cylindrical coolant channels feeding and leaving the bend had a diameter of 1/8", or 3.18 mm.

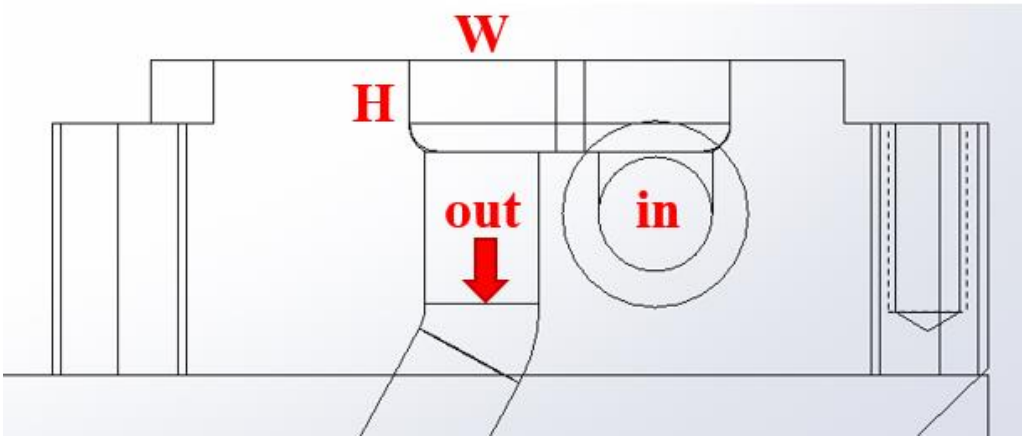

Figure 39: Coolant channel dimensions

Four plates were created for this investigation, with one that would remain as a blank. All holes were created by Meyer Tool through the use of electrical discharge machining (EDM), shown in Figure 40 before being painted. Each plate had six screws total. Each of the four corner screws secured to the airfoil, and the center two screws in the front secured down into the coolant block. As per specification, the row of holes was at a location downstream of the leading edge of the blade and 6*d* apart in pitch, being fed from the upstream leg of coolant flow.

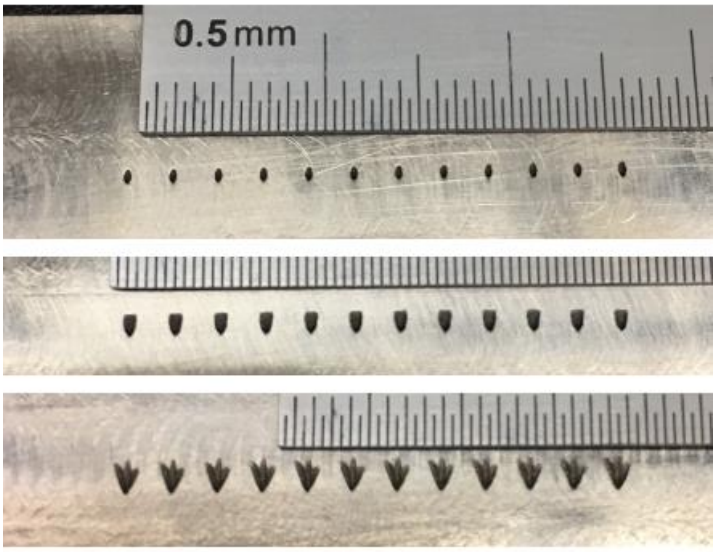

Figure 40: Cylindrical, fan, and duck foot shaped holes (from top to bottom)

3.4.2. Instrumentation

Thermocouples were attached to each plate in the same configuration to capture the necessary surface temperatures for overall effectiveness calculations and analysis, with the locations specified in Figure 41. The white line across the plate is simply for better visibility of the row of holes in the image. S1, S2, and S4 were on the external surface, and S3 was routed underneath and set on the internal surface opposite of S2. S4 was the only thermocouple not situated above or within the return leg of the coolant

channel. The S4 thermocouple was placed at a point where the plate is in contact with the coolant block below it to provide insight into the effects of conduction through the material. An estimation of the IR viewing window is also shown by the red oval in the figure and the surface was painted black for the IR thermography method. Figure 42 depicts the three thermocouples routed through the coolant block and up into the channel to capture the coolant temperature as it progressed down the channel and around the bend. B1 and B2 a located before and after the row of holes, and B3 is located at the end of the return leg. While it would be best to know the temperature of the coolant out of each hole, knowing the temperature just before and just after the row of holes will provide some of that insight.

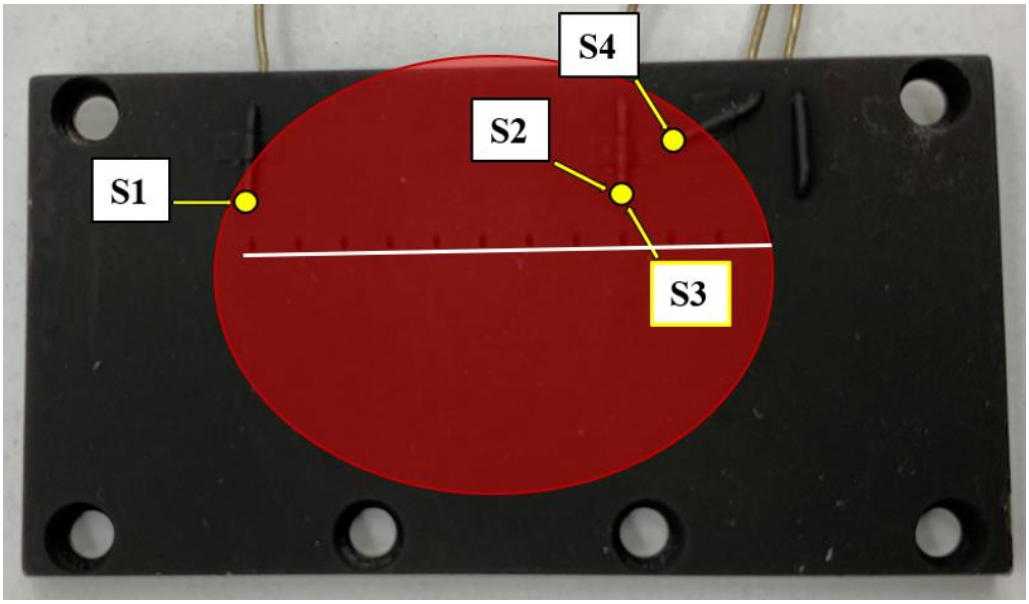

Figure 41: Pressure side thermocouple and IR viewing locations

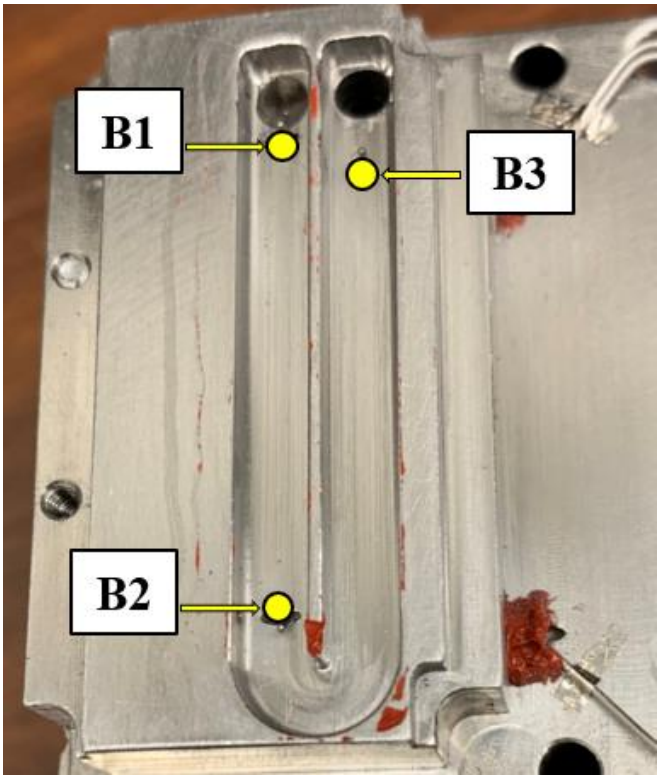

Figure 42: Honeywell coolant channel thermocouples

3.4.3. Coolant Controls

The Honeywell pressure side model was designed to use the same coolant supply line as the leading edge model. The coolant line diagram layout for this testing is given in Figure 43 The coolant supply line already had a mass flow controller to control the coolant flow into the rig, but an additional mass flow controller was connected after the coolant exited the rig. This additional coolant line was created to control the temperature of the coolant as it exited the block after the return passage. This was required to bring the temperature back to near ambient to obtain accurate flow readings from the downstream mass flow controller.

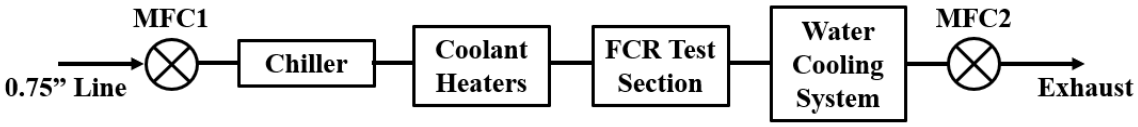

Figure 43: Honeywell testing coolant line setup

During testing, the latter mass flow controller was set so that the difference in mass flows would result in the desired blowing ratio out of the coolant holes. Based on achieving *Re* = 15,000 freestream and performing blowing ratio sweeps between about 0.5-2.0, the difference in mass flow between the MFC's, resulting in the coolant flow out of the holes, would be in the range of 2-12 SLPM. MFC1 has a flow range of 50 SLPM and MFC2 has a range of 30 SLPM. During initial testing, the same SLPM difference will be varied at various overall flow rates to examine the impact of coolant flow velocity and heat transfer.

Because the coolant would heat up during its passage through the block, a water-cooling system was built by Carl Pickl to cool the flow down so that the second mass flow controller would not be damaged. The cooling system, shown in Figure 44, was a sealed water tank that circulated water through the water-in and water-out lines. The heated coolant was brought into the tank and was sent through a copper line that was coiled within the tank, discharging the heat to the water, and back out the tank. The outlets for the water and the coolant each had an integrated thermocouple to monitor that sufficient heat was removed from the coolant before reaching the second mass flow controller.

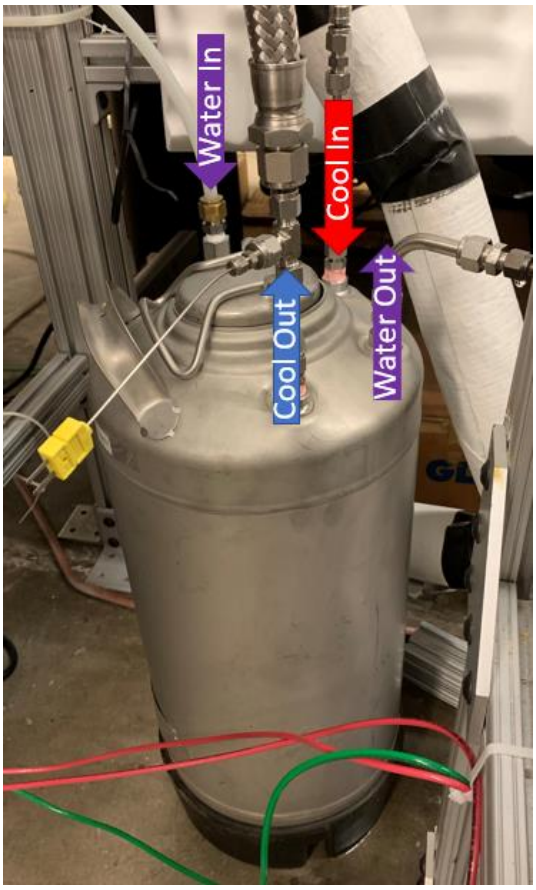

Figure 44: Water-cooling system for coolant line

A few aspects of the test section needed to be swapped out or changed to accommodate this test block and airfoil setup. The 45° viewport was utilized here instead of the 65° viewport in order to see further down the airfoil surface. A bracket that held the new side plate had a notch cut out to provide access to the new coolant-in connection, which is shown in Figure 45. Paired static pressure and thermocouple ports were also integrated into the new side plate, shown in Figure 46. These ports were to track flow temperature and acceleration data as the freestream flow progressed down the channel and around the airfoil.

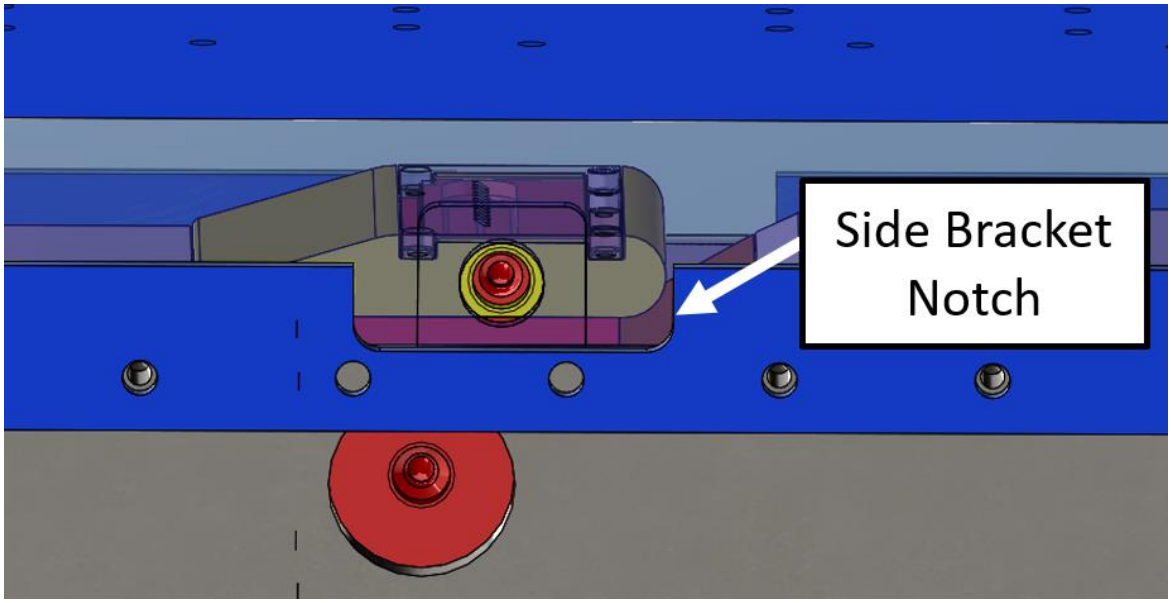

Figure 45: Side bracket notch

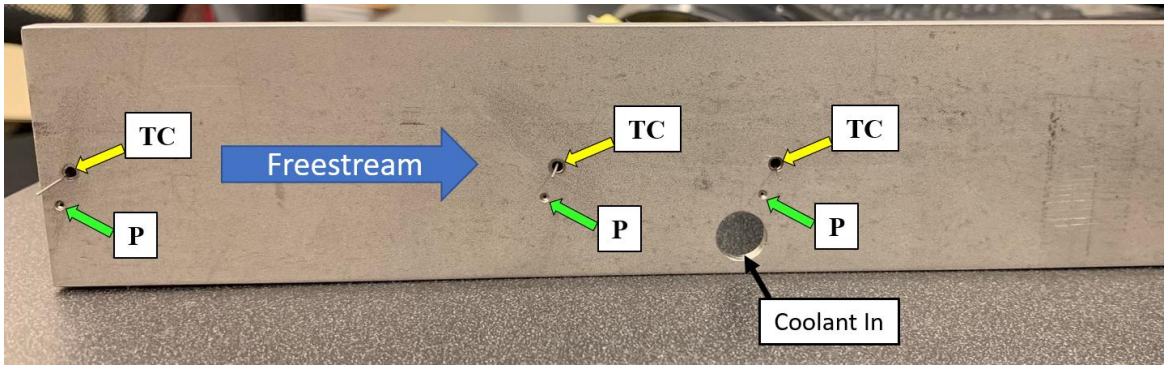

Figure 46: Temperature and static pressure ports

3.4.4. Coolant Channel Sealing

Difficulties arose when testing the seal of the airfoil and plate to the coolant block. A blank plate with no holes was attached to the airfoil. This assembly was tightened to the coolant delivery block and was expected to create a contact pressure seal, enabling all inlet flow to progress out of the coolant block channel without escaping. The airfoil had two connection rods, shown in Figure 47, that went through and out the bottom of the coolant delivery block to guide and tighten the airfoil down. The rods slide through the bottom of the block to allow the airfoil to sit all the way down. The ends of

the rods were threaded so that the airfoil could be tightened down onto the block by tightening a nut at the bottom end. The two front middle screws of the coolant hole plates screwed into the block, as well, providing increased sealing ability.

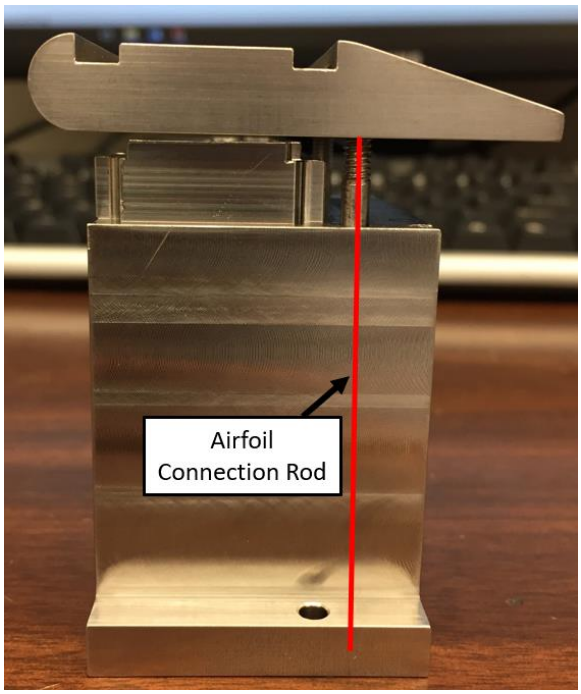

Figure 47: Airfoil connection rods

All other connections in the coolant line had been verified to not have any flow loss by tracking the controlled flow in from MFC1 and comparing that to the amount of flow that reached MFC2. A 15 SLPM flow was commanded by MFC1 and MFC2 was set to 20 SLPM, so that the indicated flow on MFC2 would be the resulting flow through the line. Without any extra sealant, the model was losing almost 10 SLPM. A 1/16" layer of compressible graphite was explored as a sealant, but would create unwanted heat transfer paths, and the best seal achieved was still losing 3.9 SLPM. A high temperature red silicone RTV border around the channel was also investigated, as shown in Figure 48. The best seal achieved here still lost 3.7 SLPM, leading to a potential redesign of the

block and channel. The RTV was also used to seal off the thermocouple entry points on the back of the block, along with sealing and smoothing off the borders around the plate, shown in Figure 49.

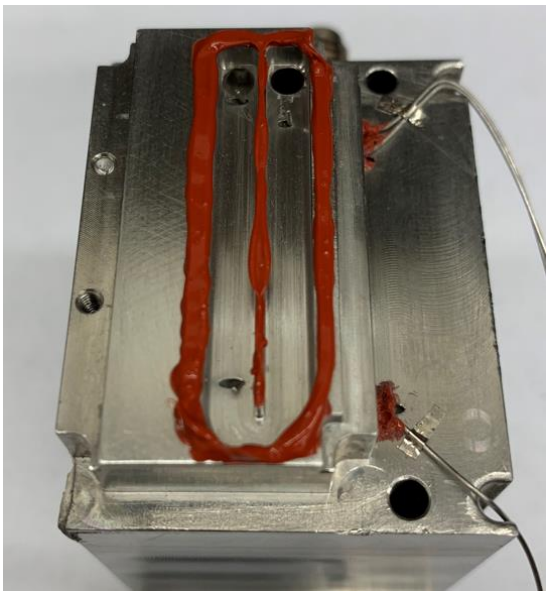

Figure 48: RTV sealant for coolant block channel

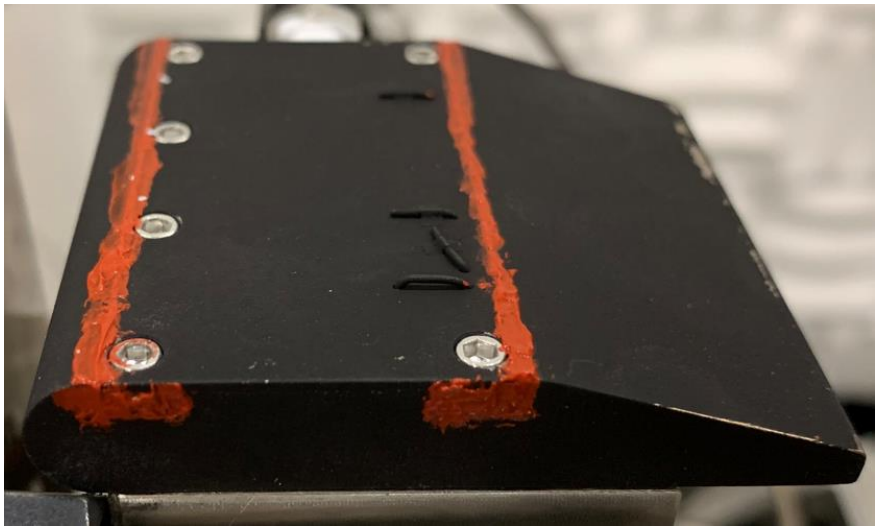

Figure 49: RTV border seal on plate

3.5. Computational Methodology

Computational fluid dynamics (CFD) simulations were run by Dr. Ryan Clark from Miami University to aid experimental validation and analyze flow conditions not achievable due to limits of the FCR's capability. This section describes the setup of the computational simulations.

The goal that the CFD simulations aimed to achieve was to expand on the exploration of density ratio (*DR*), temperature, blowing ratio (*M*), and Reynolds number as they related to film cooling effectiveness scalability. Those terms were defined back in Section 2.3. The layout of test runs to achieve that goal is given in Table 3. Tests 1-3 had the same *DR* of 1.5, the freestream temperature varied from 500-800 K. Tests 4-6 had a DR of 2.0, the freestream temperature varied from 500-1900 K. Tests 7-9 performed a blowing ratio sweep from 0.5 to 1.5 at a freestream temperature of 650 K and DR of 1.5. Lastly, tests 10 and 11 explored Reynolds numbers of 10,000 and 20,000 at a freestream temperature of 650 K, *DR* = 1.5, and *M* = 1.0.

Table 3: CFD Test Runs

Test	Reynolds Number	T_∞ (K)	T_c (K)	Density Ratio	Blowing Ratio	V_∞ (m/s)	$\dot{m}_c$ (kg/s)
1	15,000	500	333	1.5	1	57.54	0.00034
2	15,000	650	433	1.5	1	89.02	0.00041
3	15,000	800	533	1.5	1	124.65	0.00047
4	15,000	500	250	2	1	57.54	0.00034
5	15,000	1250	625	2	1	254.63	0.00061
6	15,000	1900	1000	2	1	491.19	0.00078
7	15,000	650	433	1.5	0.5	89.02	0.00027
8	15,000	650	433	1.5	0.9	89.02	0.00037
9	15,000	650	433	1.5	1.5	89.02	0.0005
10	10,000	650	433	1.5	1	59.35	0.00027
11	20,000	650	433	1.5	1	118.69	0.00055
Grid Independence Study (Adapt and smooth grid)							
12	15,000	650	433	1.5	1	89.02	0.00027
13	15,000	650	433	1.5	1	89.02	0.00027

A grid independence study was also set to be performed for most efficient use of simulation run time. However, errors with the simulations for these runs occurred and a grid independence study was not finished. As a result, what would have been set as the medium grid was used for each test case.

The computational domain incorporated all freestream and coolant air passages within the FCR test section and relevant features, including the test model and block, boundary layer trip, bypass channel, and IR window. The test section SolidWorks file was imported into Pointwise, which was used to generate a computational mesh of the FCR test section, as shown in Figure 50, with both flow and main block meshes being created for conjugate heat transfer simulations.

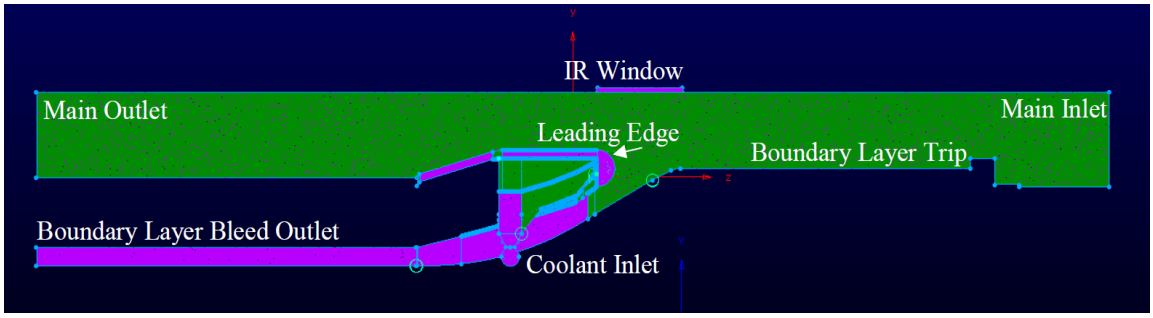

Figure 50: CFD mesh geometry of FCR [from Clark]

The airfoil model and smaller coolant passages were more refined with a greater density of cells, shown in Figure 51, to more accurately capture the flow within and around the airfoil. This area included the leading edge, coolant holes, impingement plate, and coolant plenum.

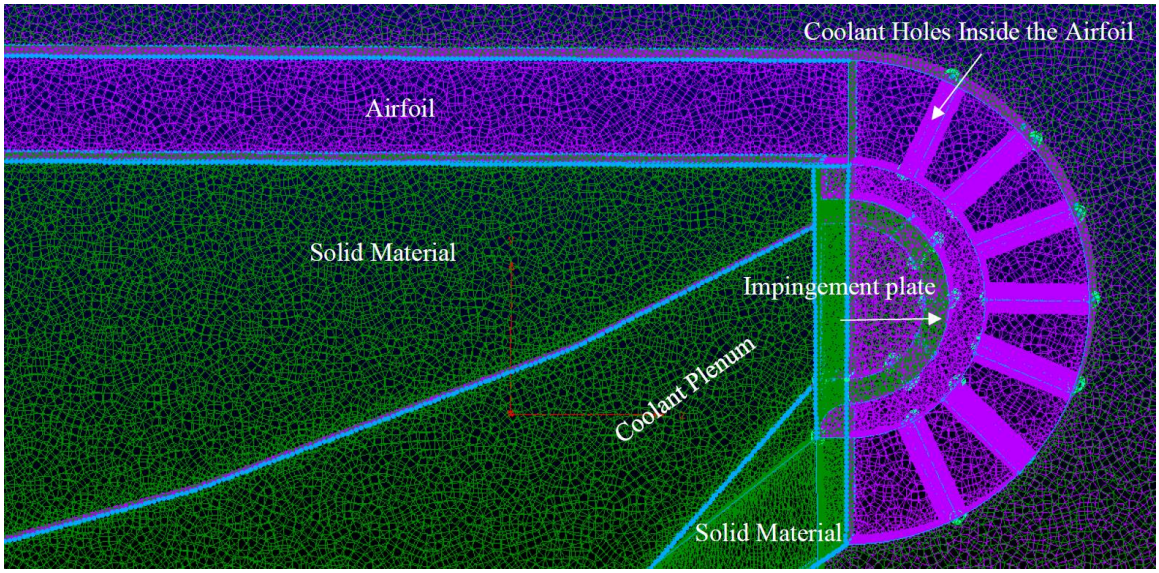

Figure 51: Airfoil leading edge mesh [from Clark]

The simulations were completed using the pressure-based ANSYS Fluent CFD Solver, using the SST k-omega turbulence model within the program. The fluid had the material properties of air. The solid material had the material properties of nickel. While the experimental model used a nickel alloy, Inconel 718, the material in Fluent's database that most closely approximates Inconel 718 (ρ = 8220 kg/m^3, k = 11.2 W/mK) is nickel (ρ = 8908 kg/m^3, k = 91 W/mK) at room and testing temperatures. The main flow inlet was a velocity type inlet. The coolant inlet was a mass flow rate inlet type. The main outlet and boundary layer bleed outlet were pressure outlets. The coolant temperature was set at the inlet to the block, and therefore experienced significant heating before reaching the airfoil. Section 4.2 goes more in depth into the heating experienced through the coolant channel.

Each test case was run until the flow and temperature values leveled out at a consistent value at about 1,000 iterations. The surfaces and flow could be colored by temperature and convective heat transfer coefficient, which are Figure 52 and Figure 53,

respectively, for CFD Case 1. It was noted that the surface temperature distribution was too uniform from what would be expected in both the streamwise and spanwise directions considering how the coolant was being ejected out spanwise. The *h* contour plot had a bit more of a gradient in the spanwise direction, but the values are all negative. Although the magnitude of the values seems reasonable, it was expected that they would be positive. The values for surface and flow temperatures still appeared to be valid, however, so the complications with the *h* values were assumed to be with how they were extracted.

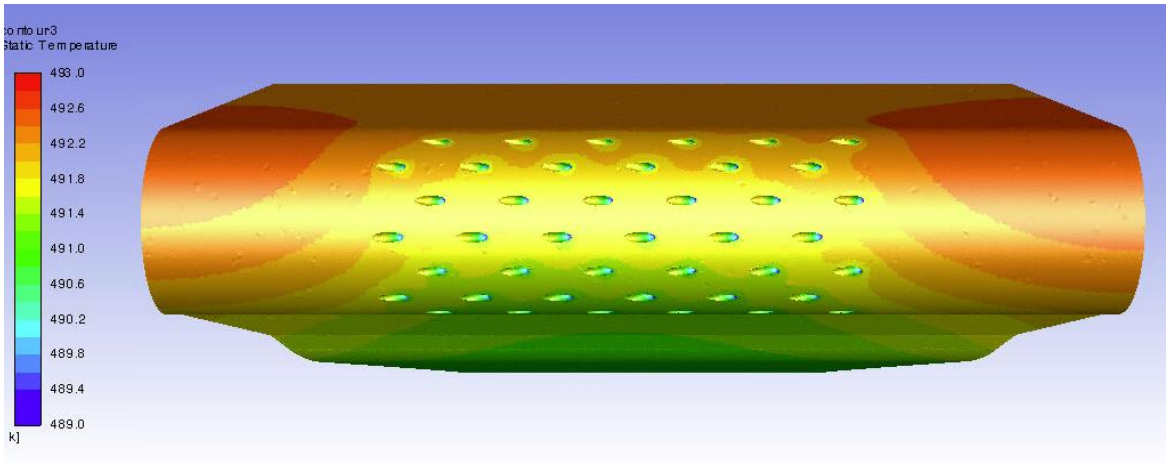

Figure 52: CFD Case 1 surface static temperature contour

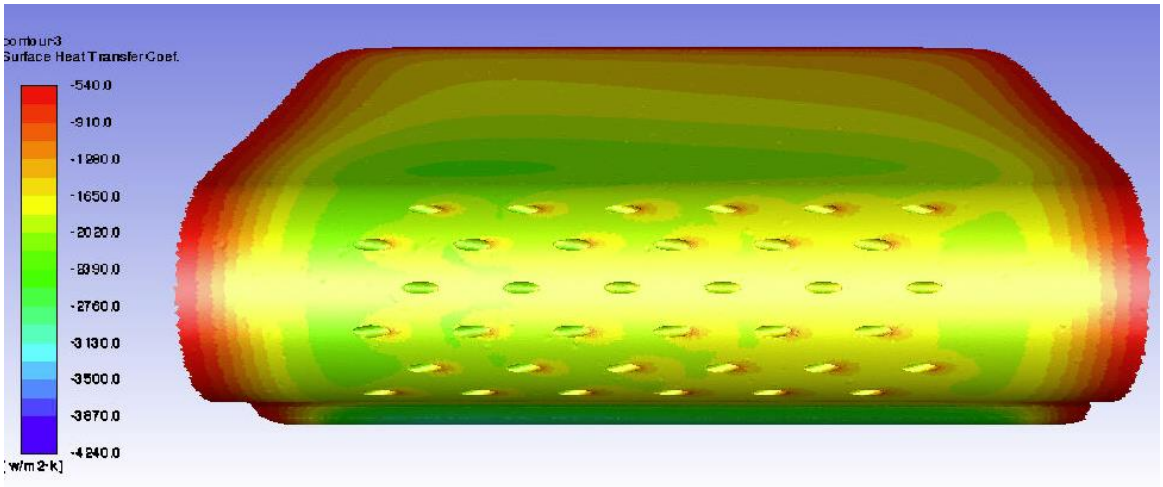

Figure 53: CFD Case 1 surface heat transfer coefficient

Nonetheless, CFD data was set up to be extracted from the same locations as the experimental data with the streamwise cut from x/d = 0 to 15 and two spanwise cuts at x/d = 4.5 and 12, as laid out in Section 4. The external data points that were extracted are shown in Figure 54.

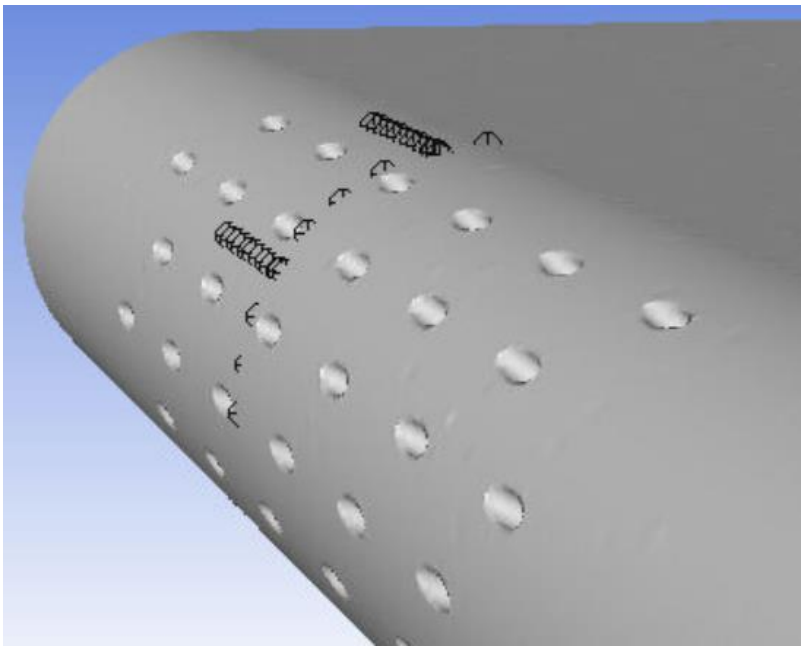

Figure 54: CFD external data points

The internal data points are shown in Figure 55 and were positioned on the internal airfoil surface opposite of the two external surface spanwise points, x/d = 4.5 for the blue box and x/d = 12 for the yellow box. Additionally, the location of the experimental thermocouple used for the coolant temperature is shown with the red box point. It was assumed that the coolant temperature varied across the internal channel, so using the temperature from the same spanwise location should help with analysis.

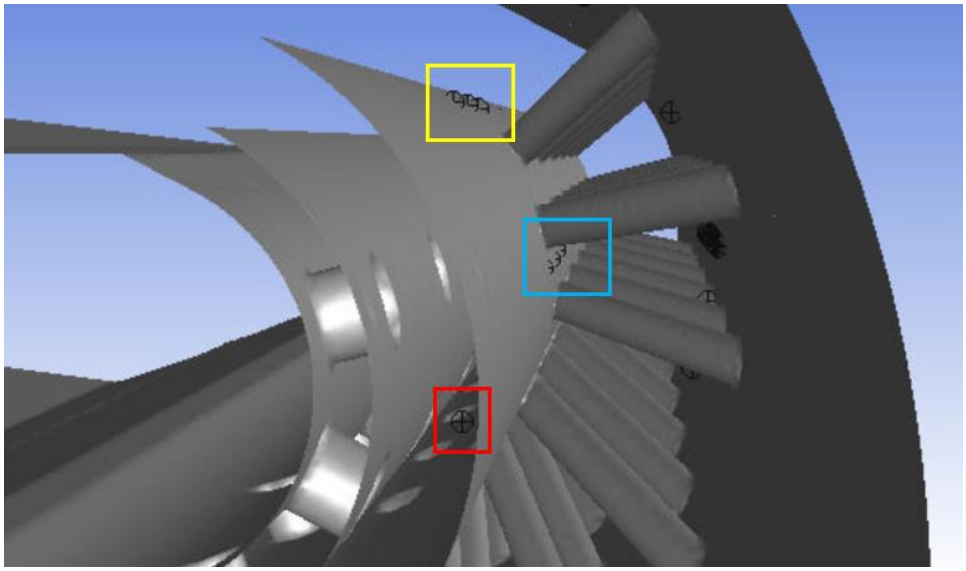

Figure 55: CFD internal surface data points

To further the analysis of the coolant temperature distribution in the internal channel, data extraction points were placed at the entrance of each coolant hole at x/d = 0 and at the fourth hole of x/d = 3, 6, and 9, shown in Figure 56. This would allow for an assessment of coolant distribution within the external area of interest for testing.

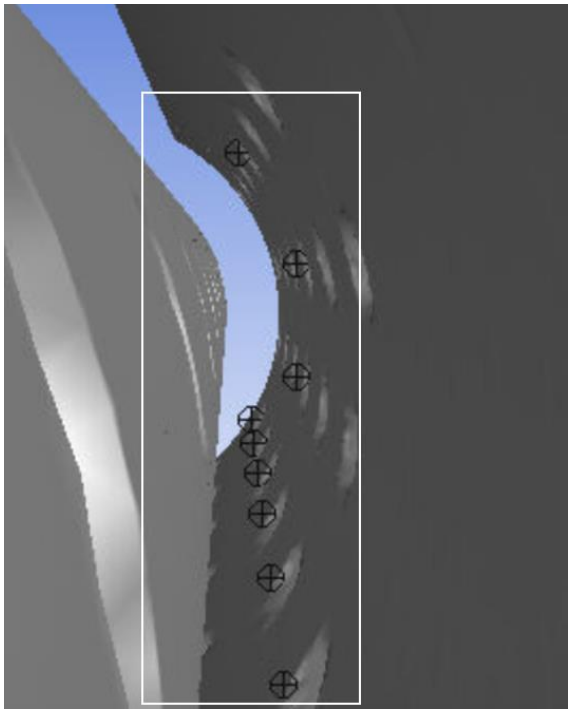

Figure 56: CFD internal coolant temperature points

Assuming proper values from these data points were achieved, the internal and external *h* values could be used in the analytical analysis used for Reynolds number in Section 4.3. Being that these values were not as they should have been, however, they were estimated for that Reynolds number analysis. The internal coolant temperature, external surface temperature, and freestream temperatures would be used to calculate overall effectiveness and compare to experimental results.

3.6. Test Setup

This section will review initial setup analysis and measurement equipment and techniques used to conduct this investigation. Section 3.5.1 will cover how the leading edge stagnation region was assessed. Section 3.5.2 outlines the thermocouple setup and IR thermography method. The method for solving for overall effectiveness is detailed in Section 3.5.3.

3.6.1. Stagnation Investigation

Knowledge and understanding of the location of the stagnation region on the leading edge of the airfoil allowed for better analysis of the test results and how the coolant flow was behaving as it exited each row of holes. An investigation into the location of the stagnation region was performed. The aim was to have the location be along the central row of holes at $x/d = 0$, pictured in Figure 57.

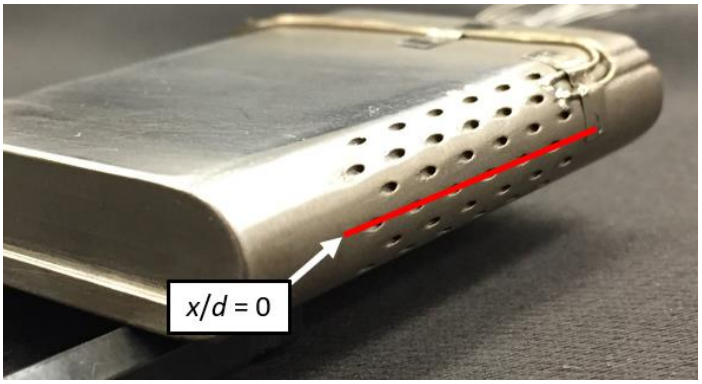

Figure 57: x/d = 0 row specification

Discussed in with Figure 19, the bypass channel was created to serve the purpose of similarly splitting the flow, with the bypass adjustor at the exit of the channel to vary the flow through the channel, thereby shifting the stagnation line in either direction from that central row.

A blank airfoil with no holes was used to experimentally investigate the stagnation line, shown in Figure 58. A fine white paint pen was used to draw lines on the model to represent the *x*/*d* coolant hole rows at 0, 3, and 6. An oil solution containing a fluorescent powder was utilized in conjunction with a black light to obtain a visual of the flow split when the freestream air was turned on, representing the stagnation region. The visual was captured using a Nikon DSLR high-definition camera. Once applying the solution to the model, the freestream airflow was set to an average testing condition of 3 kg/min, but the increase to the set airflow in the channel was not immediate. The flow increase was gradual enough for the fluid to split and dry on the airfoil before the freestream flow reached its intended velocity, so the true stagnation region may be slightly different than found here, but would still remain in the same region. Three bypass adjustor positions were tested: fully open, half open, and fully closed. It was found that the more restricted the bypass flow became, the higher up from center the

stagnation line moved. The fully open bypass position resulted in the stagnation line closest to the center, which is shown in Figure 58. This was not a completely precise analysis, but did serve as a useful rough estimate. With how the rig was set up, the stagnation line was not able to be situated directly on $x/d = 0$.

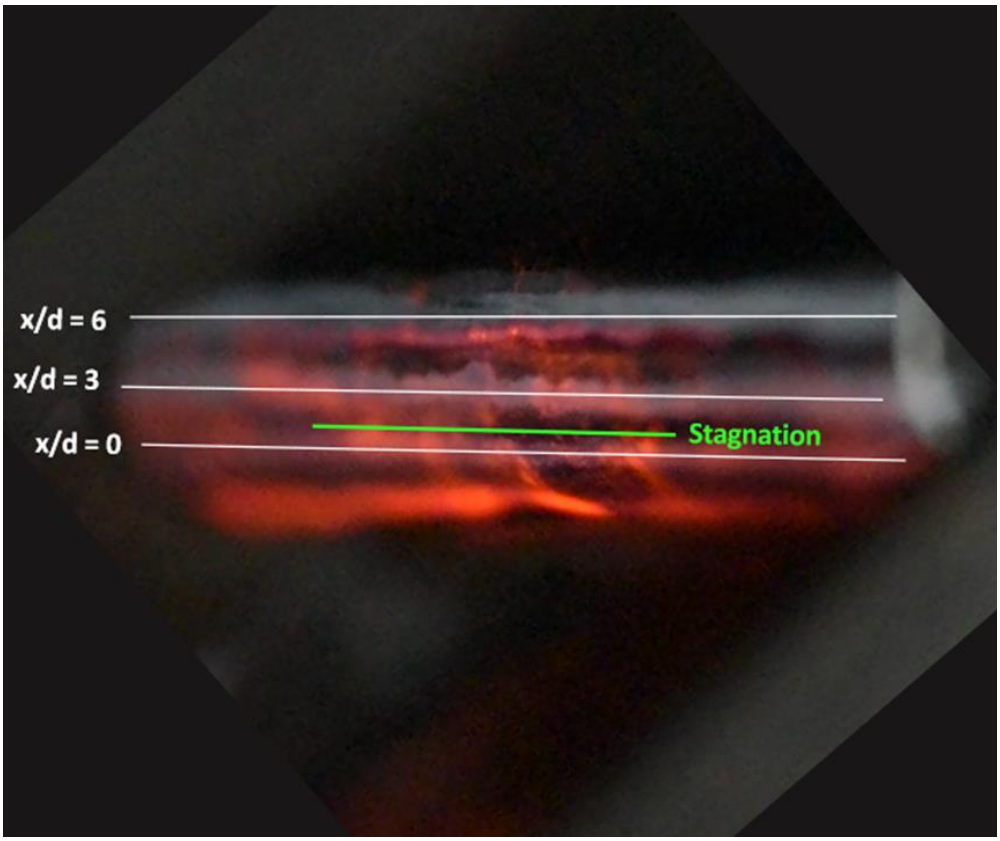

Figure 58: Experimental stagnation location with fully open bypass

This stagnation region found experimentally was also validated computationally. By viewing the streamlines of the coolant leaving the coolant holes and observing the direction they turn, the location of the stagnation region can then be inferred. As seen in Figure 59, all of the streamlines exiting the central row of holes at $x/d = 0$ turn downward and go under the airfoil, where the streamlines from $x/d = 3$ turn upward toward the top

surface. This flow split was indicative of the stagnation region being between those two rows, validating the experimental analysis.

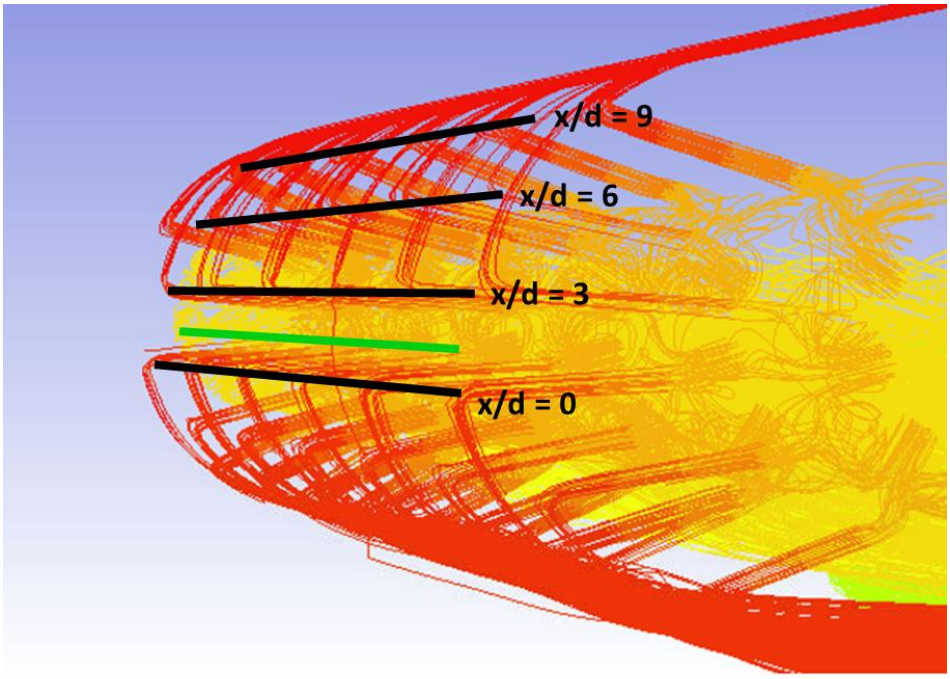

Figure 59: Computational stagnation validation

3.6.2. Thermocouple and IR Thermography Method

This research used a combination of thermocouples and IR thermography in order to quantify the temperature of the area within the test section. A series of thermocouples were installed at various points within the freestream flow, coolant flow, and surface points on and within the test airfoil and coolant block.

A series of 0.51 mm K-type thermocouples, highlighted in Figure 60, measured the coolant flow as it entered the coolant block through to exiting the leading edge coolant holes, as well as multiple surface temperatures on the external and internal sides of the airfoil. Coolant temperature was measured just before entering the coolant block, just inside the impingement plate, and within the coolant plenum between the

impingement plate and the internal side of the airfoil. The freestream temperature was initially thought to be accurately measured by a single 1.59 mm diameter Omega K-type thermocouple about 12.5 cm upstream of the test airfoil, at the entrance of the FCR test section. But that was found to be set back within a side cavity and not directly measuring the freestream. A 0.51 mm diameter K-type thermocouple was then inserted through an extra existing pressure port at the same distance upstream of the airfoil and properly into the freestream flow. The freestream temperature was used as the reference for determining the Reynolds number and *M* for the mass flow of each test case, as well as the basis for the *DR*.

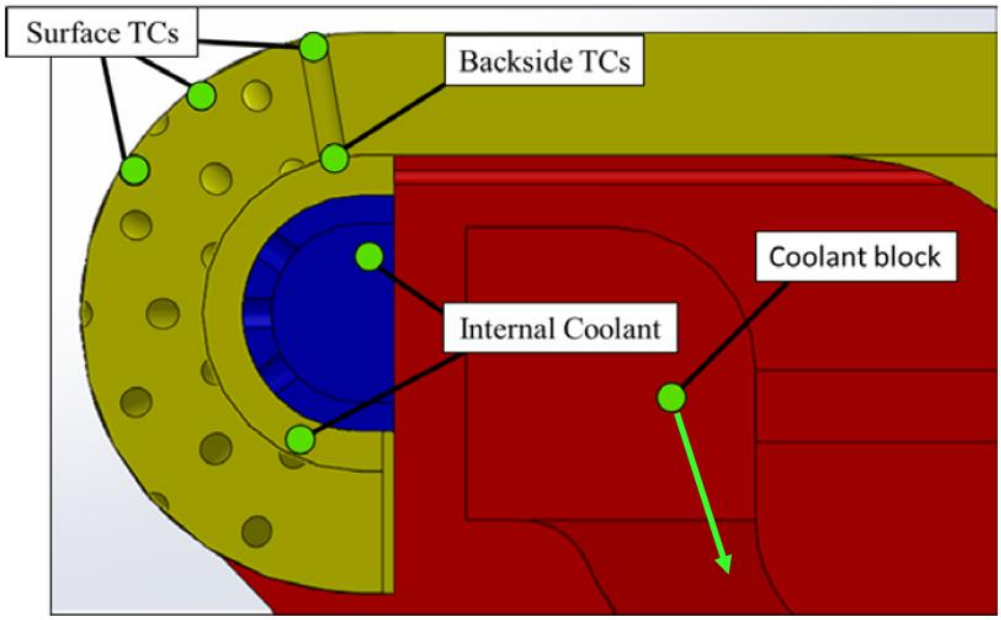

Figure 60: Test block thermocouple locations, adapted from Tewaheftewa [12]

Thermocouples were placed for surface thermal measurements as shown in Figure 61 to be used in effectiveness calculations and IR thermography calibrations. They were attached with spot welds and had the tips welded by Precision Join Technologies. The red oval in Figure 61 shows what the IR camera was able to see of the test surface,

including the center and pressure side rows of coolant holes. Figure 62 labels the visible rows and a corresponding raw IR image with intensity measured in counts. The orientation of the airfoil in those images has the airfoil leading edge pointed down, and the freestream flowing up. The blue-green surface of the airfoil where the holes are visible is the region of interest through the sapphire window, and the red border around the image is the adhesive to hold the window in place.

The IR camera software had a built-in temperature conversion, but that feature was not employed given the large temperature variations within the IR camera's view between the heated model and the cooler external test section surfaces. A separate IR calibration process was used to convert the IR count readings to surface temperatures, along with providing a temperature uncertainty. The process involved, on days of testing, stepping up through a temperature range to approach the desired testing freestream temperature and allowing the temperature to settle and level off at each step. For example, if the desired freestream temperature for test data was 500 K, calibration points would be taken in increments of 30 K starting at 380 K with the coolant flow off. The remainder of this section steps through that process and makes note of various challenges that were encountered during the IR calibration process.

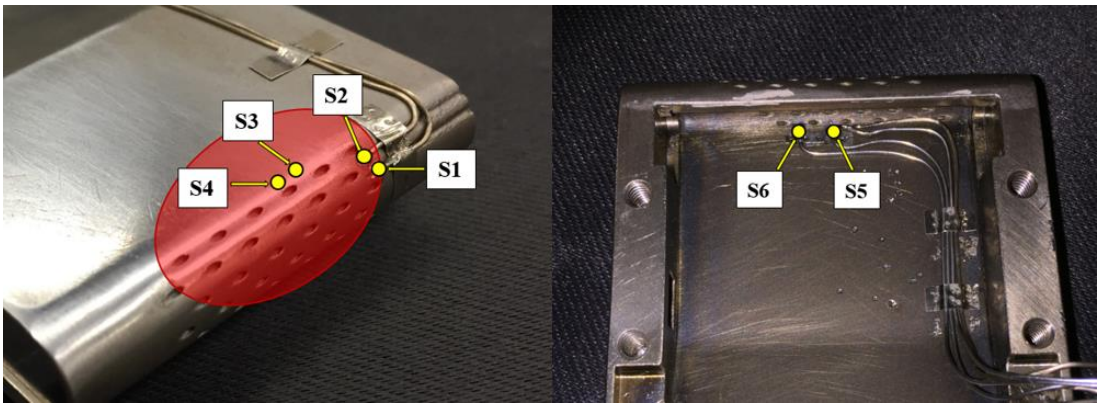

Figure 61: Test airfoil surface thermocouple external (left) and internal (right) locations

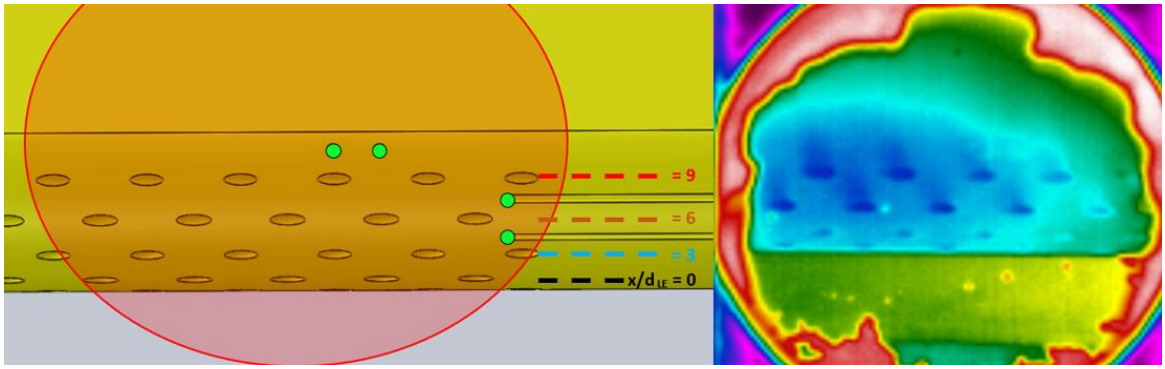

Figure 62: IR viewing diagram (left) and raw image (right)

It was important to have the camera settings properly set before each round of testing. The camera had a "Cal/Int" setting, which was similar to a light sensitivity setting for a normal camera, to adjust the exposure setting and related how wide a range of temperatures corresponded to a count range. A higher value setting would result in a greater range of counts for a given temperature regime, resulting in the calibration curves not falling on top of each other. Having the same Cal/Int setting on different days of testing would allow for comparison and repeatability for temperature calibration.

The IR image on the right of Figure 62 is an example of the raw image directly from the camera. 120 frames were taken over 2 seconds at 60 Hz and stored as .csv files of the count value by pixel. The 120 frames were averaged together by pixel into a single file, and the averaging helped account for any minor vibrations of the image. Because the flow through the rig was not completely steady, vibrations within the span of a pixel may have occurred. During that same time, thermocouple data was taken at 20 Hz using the LabVIEW program. If multiple data lines were taken for the same data point, those were averaged, as well.

The calibration code read in the thermocouple temperature data for thermocouples 1-4, as they were the ones visible through the IR window, and paired them to the

corresponding locations specified on the IR image for each thermocouple. When identifying the locations on the IR image and inputting into the code, it was important to note that the (0,0) origin started at the top left of the image for the IR program, while the origin in the code started in the bottom left. This resulted in subtracting the y-location from the IR image by the total pixels in the vertical direction to get the correct y-value input for the code. Once the thermocouple and IR count values were paired using the desired calibration data points, they were graphed and a calibration curve fit was generated. The calibration curves for the four temperature regimes tested are in Figure 63. The Cal/Int setting for each calibration and the resulting temperature uncertainty for each calibration are given in Table 4. The indications for having the same or different Cal/Int settings between cases can be noted by checking what the corresponding temperature is for any given count value.

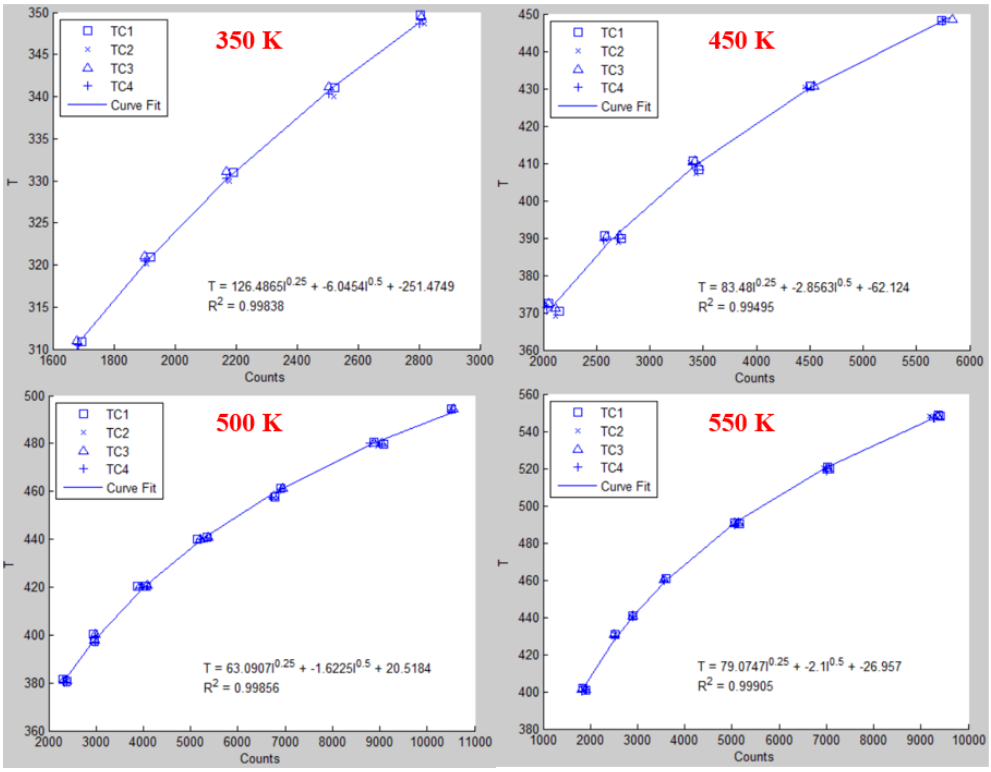

Figure 63: Calibration curves for all temperature regimes tested

Table 4: Calibration Settings and Uncertainty

T_∞	Cal/Int	Uncert
350 K	0.08	1.19 K
450 K	0.07	3.77 K
500 K	0.07	2.85 K
550 K	0.03	3.25 K

Figure 64 shows two examples of the same calibration set but using two different equations to solve for the curve fit. The left used a quartic polynomial of only the fourth power term and a constant, while the right introduced a squared term to make it a biquadratic. Adding the additional term created a visibly better agreement between the curve and data points, highlighted by the red oval on each graph, and decreased uncertainty by almost 5 K, resulting in a 2.71 K uncertainty, down from 7.02 K.

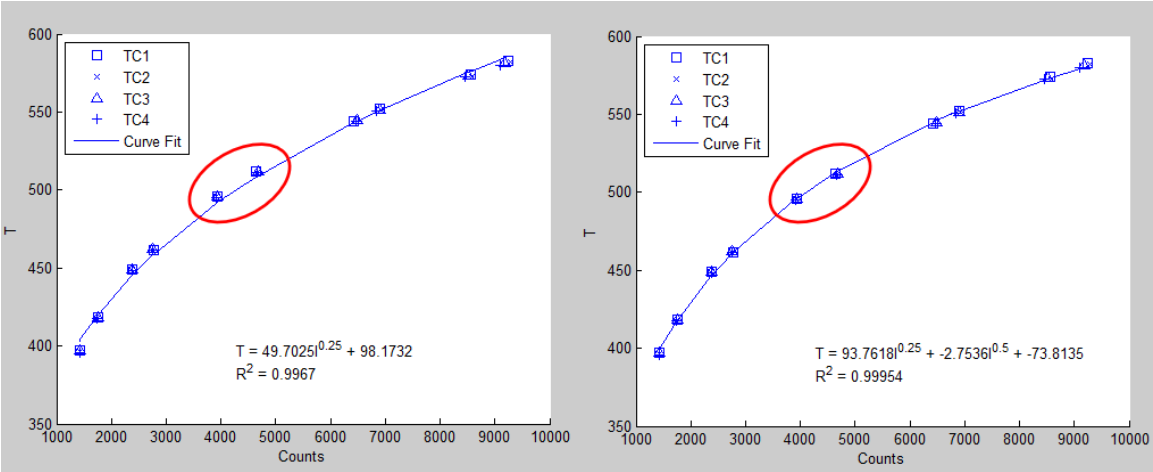

Figure 64: Improved calibration curve fit

Figure 65 shows the calibration curves from two separate days of testing but with the same camera Cal/Int setting of 0.07. The curves very closely match with an average difference over the 370-450 K temperature range of 2.74 K. While one test had a greater temperature range, the other only covered the 370-450 K range, so that was the limit for this comparison.

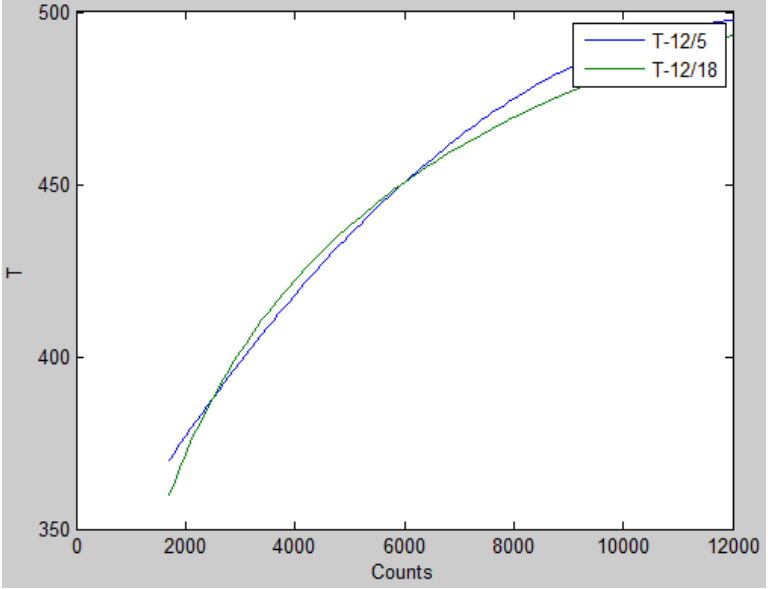

Figure 65: Calibration repeatability

An additional challenge to overcome was the existence of the welds on the tips of the thermocouples on the surface. During initial calibrations, a discontinuity between portions of the calibration range occurred with each thermocouple except for TC2, as shown in Figure 66. Because radiative intensity is related to temperature at the fourth power, the axes have T^4 to counts. During the lower temperature steps in calibration, the coolant flow was turned off for points 1-4 and 20-23. Coolant flow was turned on once temperatures were hot enough so that the coolant temperatures seen would not be lower than the initial calibration step. In theory, whether the coolant was on or not should have made such a difference. The only difference between TC2 and the others was that after having the tips welded, TC2 and needed replacing, but was not able to be sent off and welded again due to time constraints. TC2 was then truly on the surface, where the other three had a layer of metal, however small, covering the thermocouple tip. When the coolant was then turned on, large temperature gradients were created between the internal and external surfaces, and that gradient was enough to cause a difference in what

temperature each welded thermocouple read versus what it would have read if it were fully at the surface. This discovery lead to future calibrations being performed up to testing temperature with the coolant flow off so that there was a more uniform temperature distribution through the entire material. If the discontinuity were left in place, the calibration line would have split the difference between the portions of curves, resulting in all calibration results being slightly off by 1-3 K.

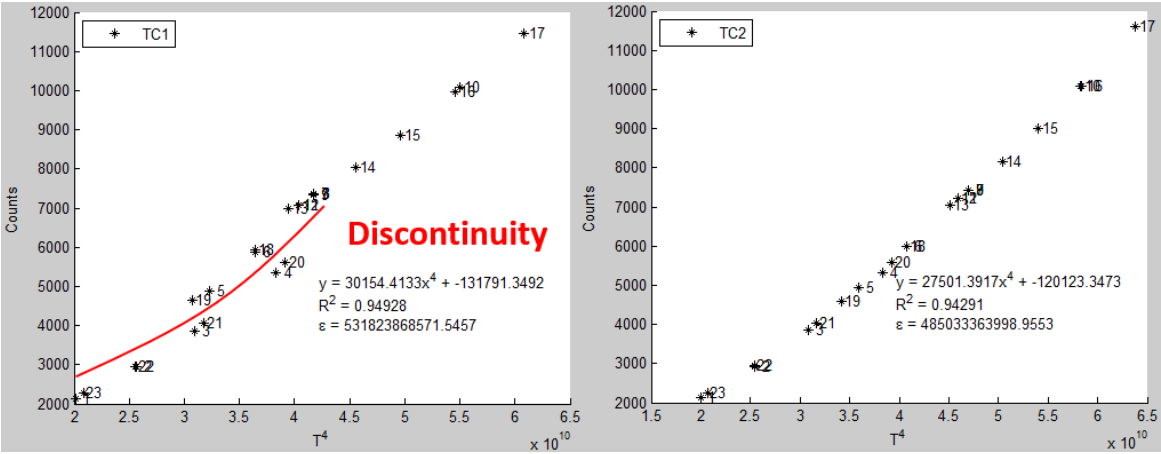

Figure 66: Calibration surface discontinuity between welded (left) and exposed (right) thermocouple

An additional calibration adjustment was utilized for the T_∞ = 350 K cases. Upon initial examination, the overall effectiveness results were as much as 0.1 lower than the corresponding conditions at the other temperature regimes. The calibration data was investigated and found that there was a discrepancy in the counts values for a given temperature point on the way up to testing conditions versus on the way back down. There was a gap between the two data sets at each calibration temperature, which the calibration curve fell between. The gap before the correction can be seen on the left of Figure 67, and the adjusted curve on the right. To make the adjustment, only the calibration points on the way down from testing temperature were used. It was reasoned that the test rig was more thermally soaked during those data points, so those were the

ones that were used. The new calibration curve resulted in a lower surface temperature conversion by 1-2 K, resulting in an increase in overall effectiveness values of as much as 0.03.

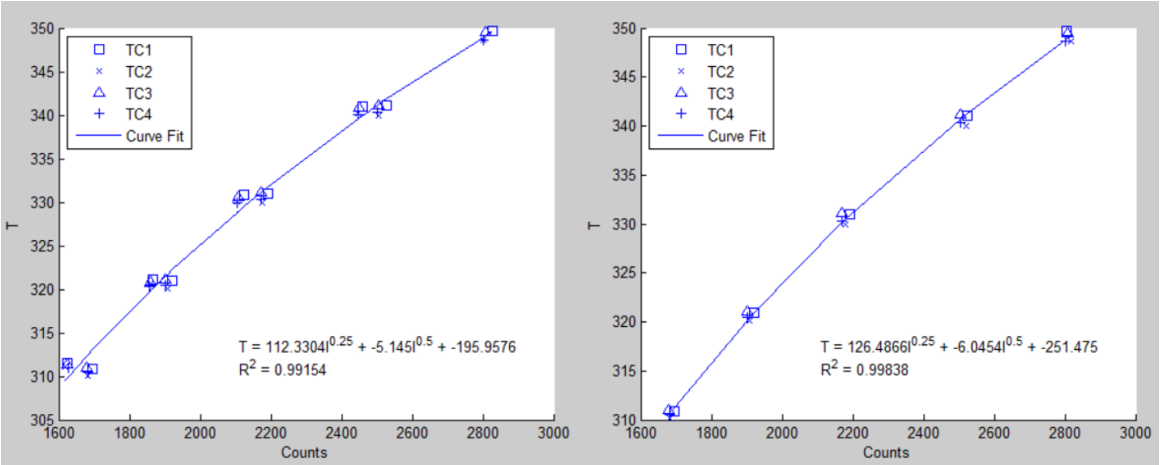

Figure 67: T_∞=350K calibration curve correction

3.6.3. Overall Effectiveness Plot

Using the curve fit from the temperature calibration, overall effectiveness can then be solved for the portion of the airfoil visible through the IR window using Eq. (1). The surface temperature, T_w, of the airfoil was solved for at each pixel using the calibration curve fit, and ϕ was solved for using the freestream temperature, T_∞, shown in Figure 68, and the internal coolant temperature, T_{ci}, between the impingement plate and the internal airfoil surface, shown in Figure 60.

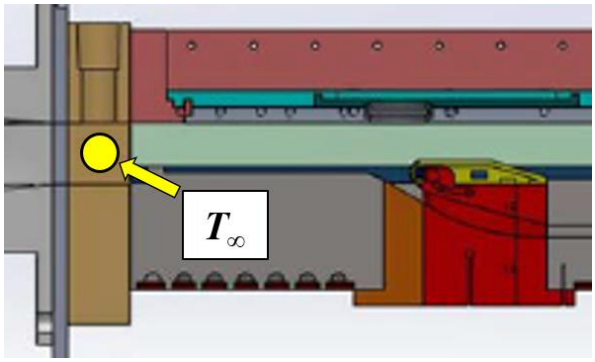

Figure 68: T_∞ location

The freestream temperatures for testing ranged from 350 K to 550 K, and are outlined in detail in Table 9 in Section 4. The results for overall effectiveness for an initial shakedown run of testing at 500 K came to be in the 0.3 range at M = 0.9 instead of Bryant's values of 0.6-0.8, seen in Figure 8, which was expected with matched flow conditions to her tests. Upon investigation it was found that the thermocouple that was expected to be measuring the freestream temperature entering the FCR test section was set back in an access hole out of the flow by about 2.5 cm, which resulted in what was determined to be a 45 K lower reading for T_∞ than what the airfoil was actually experiencing. This difference was determined by inserting an additional thermocouple through an unused pressure port at the test section entrance more than half a centimeter into the freestream flow and running the rig again to where the original TC read 500 K. The new TC inserted properly into the flow then consistently read 545 K. Increasing the freestream temperatures used in the 500 K cases by 45 K then resulted in the range of 0.6 overall effectiveness values as expected. The original overall effectiveness contour before adjusting T_∞ is on the left of Figure 69, and the adjusted contour on the right.

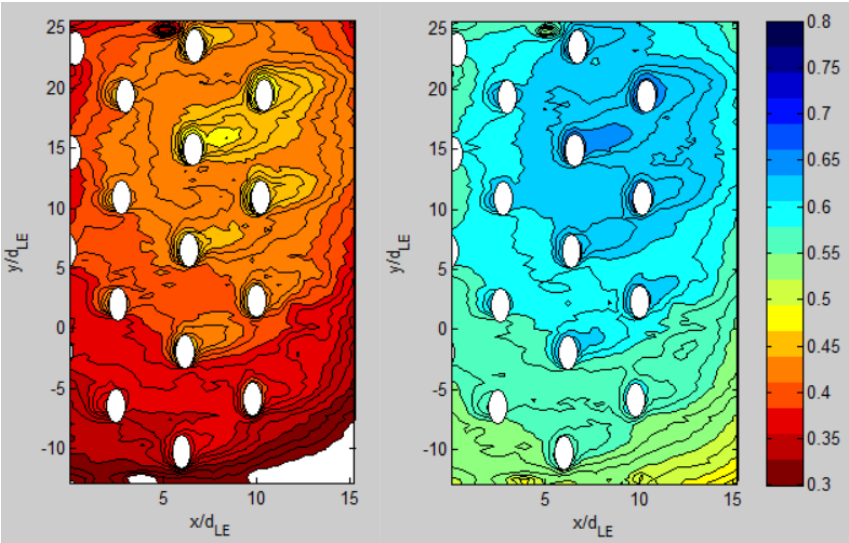

Figure 69: Overall effectiveness before (left) and after (right) T_∞ correction

Once the ϕ calculations were done by pixel, the image needed to be spatially calibrated to create a two-dimensional contour. The process mimicked the technique used by Tewaheftewa [12]. Due to the viewing angle of the IR camera to the leading edge, this spatial calibration was most required to flatten out the curvature of the leading edge into a two-dimensional plane to more effectively view and analyze the contour results. To accomplish the spatial calibration, a 1/16" fine grid was printed, carefully traced over with a fine pen, and attached to the airfoil surface, shown in Figure 70. The material difference between paper and ink created enough of an irradiative difference to be detected by the IR camera when heat was applied.

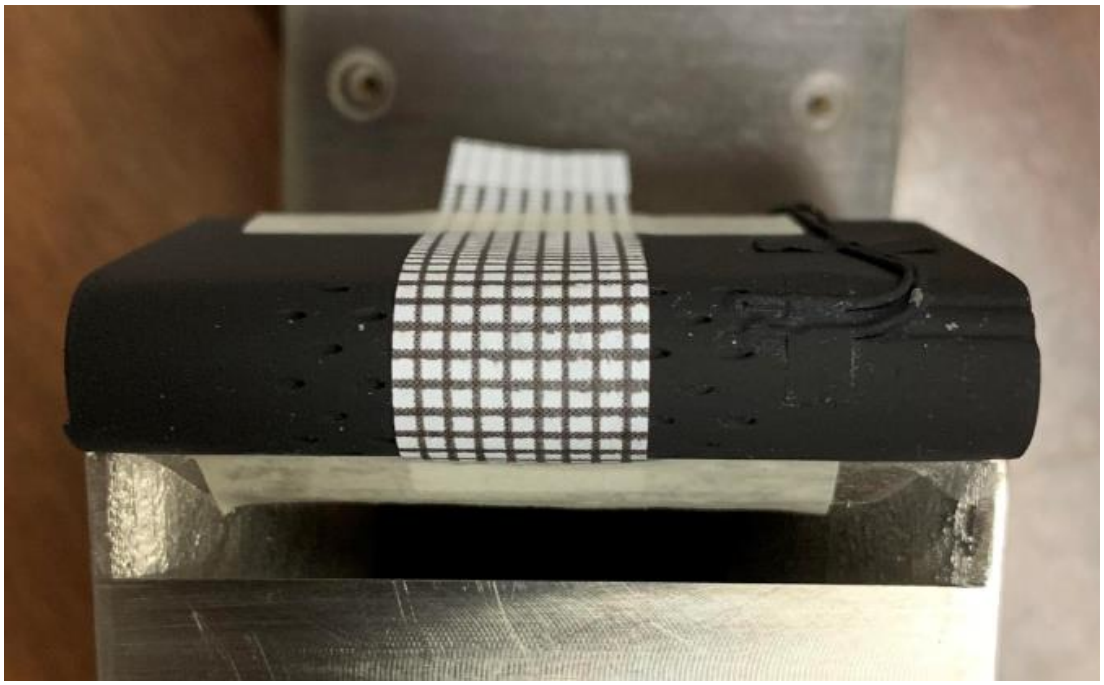

Figure 70: Spatial calibration grid

A coded grid was created using pixel locations from the raw IR image and a fourth-order polynomial was used to generate a curve fit in the x-direction. Figure 71 shows two of these curve fits, one including and one excluding the zero point defined as the center row of holes and supposed stagnation line. For this application, the curve fit

including the zero point was used for the spatial calibration because it produced a more accurate positioning of the coolant holes. Figure 72 shows an image spatially calibrated in this manner.

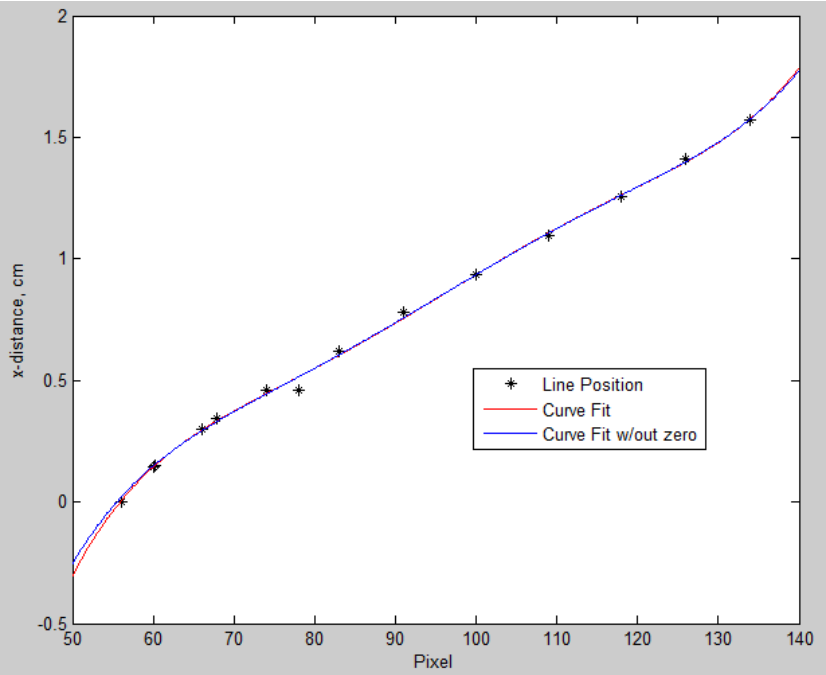

Figure 71: Spatial calibration curves

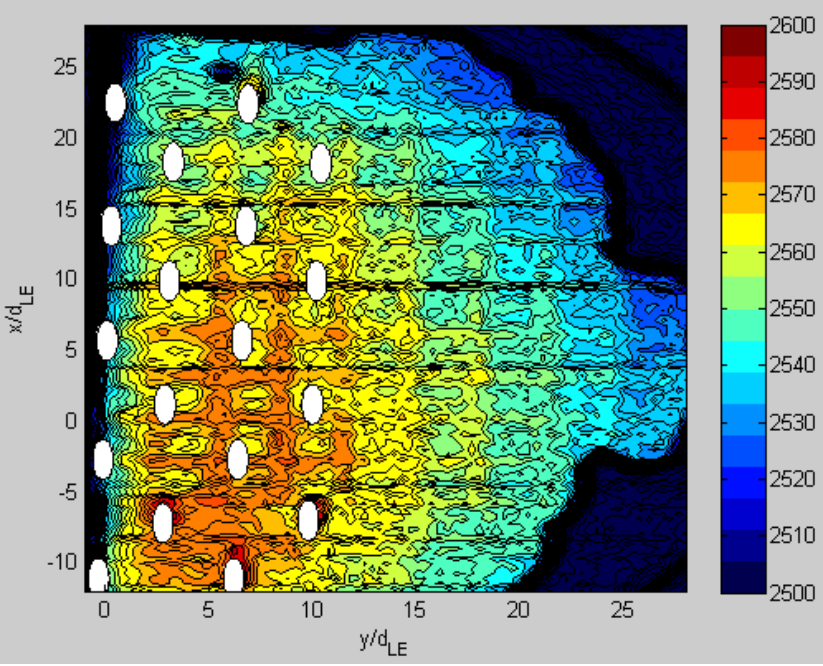

Figure 72: Spatially calibrated image, in counts

Applying the spatial calibration curve to the overall effectiveness data calculations resulted in a 2D ϕ plot like the one shown in Figure 73, and analyses of these results will occur throughout Chapter 4. White ovals were placed not only to specify each hole location, but to remove the misleading ϕ calculations resulting from being able to view within the hole openings and not actually on the outer surface.

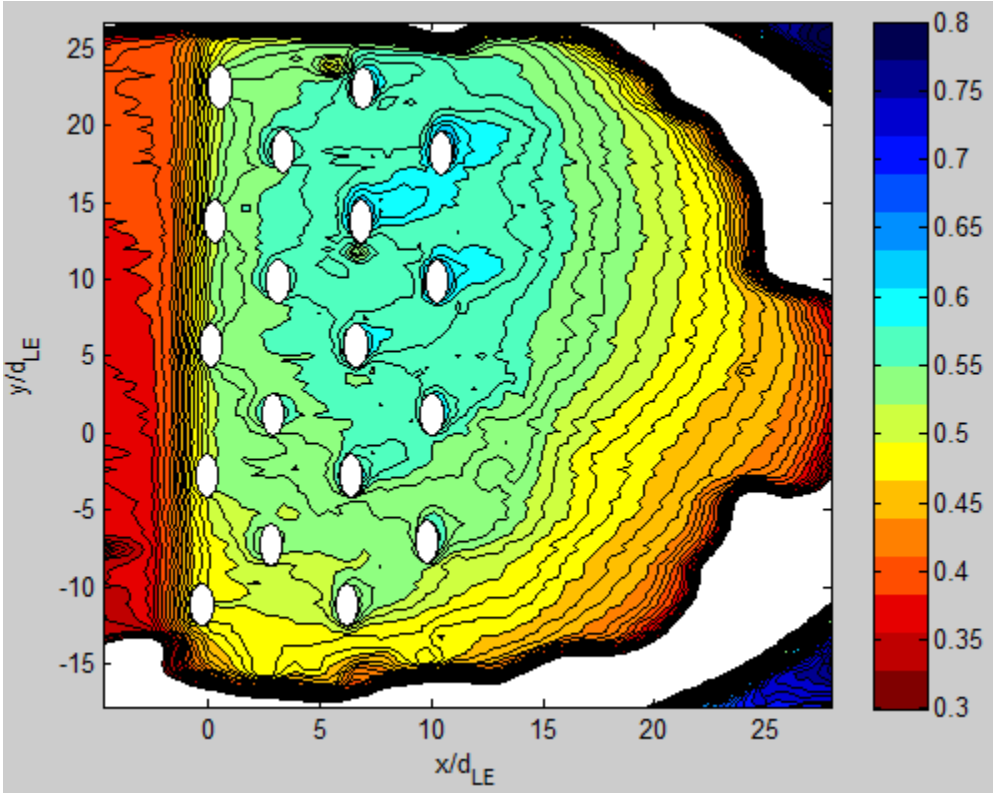

Figure 73: Spatially calibrated overall effectiveness plot

The overall effectiveness contours were then cropped to only display the area of interest on the leading edge model, with an example of a final contour image shown in Figure 74. The area of interest was the top half of the leading edge from the center row of holes, $x/d = 0$, to the top of the leading edge, $x/d = 15$. The spanwise edges were cropped to remove the portions of sealant around the viewing window that were visible within the image.

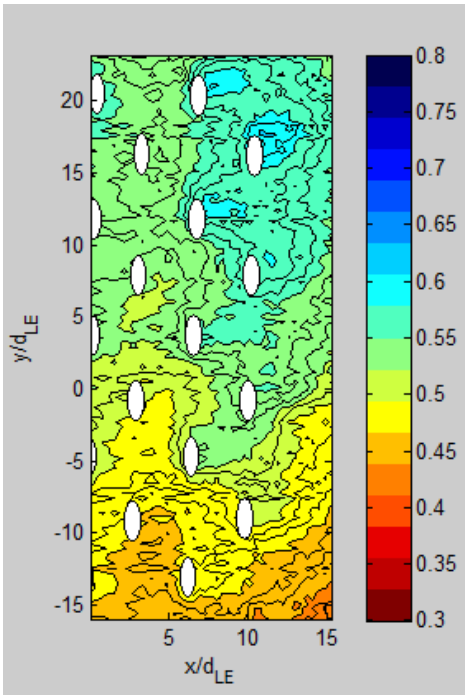

Figure 74: Final overall effectiveness contour

3.7. Repeatability

To determine the reliability of the experimental results, the same exact test case was run twice during the days of testing for the 450 K, 500 K, and 550 K data sets, resulting in six repeatability data collects. The test case was at T_∞ = 450 K, *Re* = 15,000, and *M* = 0.9. This repeatability test case was taken once on the way up in temperature and again on the way down on each test day, seeking to encompass repeatability over the full range of testing. Table 5 shows the repeatability data results for those test cases by taking the average, standard deviation, and 95% confidence interval for each parameter. The overall effectiveness results were averaged over the same streamwise data line used throughout the results analysis of this investigation.

The analysis showed fairly good repeatability through most of the parameters. Both *Re* and *M* were connected to the performance of the freestream mass flow, so any

variations in that mass flow would be carried through to those terms. There was low standard deviation for the freestream mass flow, however, so *Re* and *M* standard deviations also remained low. The freestream temperature was not directly hit at 450 K each time and varied by about ± 1 K, but the coolant temperature varied by a similar proportion for each test, resulting in a low standard deviation of *DR*, which is based on the ratio of those two temperatures. Overall effectiveness was the parameter that did not have as tight of a standard deviation compared to the others. Its standard deviation and confidence interval were right around the extremes for its uncertainty of 0.35. But due to additional environmental effects incorporated in the overall effectiveness calculations and surface temperature readings, it would be plausible that a higher standard deviation would occur, as experienced here, shown in Table 6. The variation of overall effectiveness is still higher than might be expected, however, and that would require further investigation. The freestream and coolant temperatures are also given for each case and appear to be very similar. If it were a calibration issue, Cases 3 and 4 or 5 and 6 would have similar ϕ values, but they vary before and after that round of testing. Other environmental factors or heat transfer paths may be influencing these values and would require more focus going forward.

Table 5: Repeatability Analysis Results

	Re	$\dot{m}_{\infty}$, ***kg/min***	T_{∞}, ***K***	T_C, ***K***	***M***	***DR***	***Φ***
Average	15230	2.954	450.25	419.55	0.898	1.073	0.534
StdDev	289	0.054	0.86	1.41	0.016	0.003	0.047
95% CI	231	0.043	0.69	1.13	0.013	0.003	0.038

Table 6: Overall Effectiveness and Temperatures for Each Repeatability Case

Repeat	T_∞	T_C	ϕ
1	450.97	420.25	0.482
2	449.06	417.24	0.487
3	451.68	419.76	0.597
4	450.17	421.10	0.501
5	449.76	418.13	0.589
6	449.84	420.81	0.547

3.8. Uncertainty

This uncertainty analysis covers to cases that were at opposite ends of the testing spectrum, both in testing conditions and IR calibration uncertainties. Table 7 summarizes the measurements used in this analysis in addition to the factory reported measurement uncertainties and calibration uncertainties for each case.

Table 7: Uncertainty Analysis Values

Measurement	Low T/ Low M/ Low Re	High T/ High M/ High Re	Uncertainty
$\dot{m}_\infty$ (kg/min)	1.647	3.369	±1%
$\dot{m}_c$ (kg/min)	0.0098	0.0338	±1%
T∞ (K)	351	550.3	±0.75%
Tc (K)	341.1	497.4	±0.75%
Ts (K)	345.5	518.2	1.14K/3.25K

By using these values, uncertainty was assessed for *M*, *DR*, and ϕ by using the constant odds, root-sum-square given by Moffat [32] in Eq. (25),

$$\delta Z = \left[\sum_{i=1}^{N}\left(\frac{\partial Z}{\partial X_i}\delta X_i\right)^2\right]^{\frac{1}{2}} \tag{25}$$

where *Z* is the parameter of interest, *X* is a variable of the parameter *Z*, and δ represents the uncertainty of the variable or parameter of interest. *M* and *DR* uncertainties were

assessed using their alternate forms in Eq. (6) and (5). The uncertainty results are summarized in Table 8.

Table 8: Uncertainty Analysis Results

	Case 1		Case 2	
Parameter	**Value**	**Uncertainty**	**Value**	**Uncertainty**
M	0.89	0.013	1.51	0.021
DR	1.03	0.011	1.11	0.012
ϕ	0.556	0.218	0.607	0.081

The coolant temperature was the parameter driving the uncertainty in Case 1, but surface temperature from the IR calibration drove uncertainty for Case 2. The calibration uncertainty was 2 K greater for Case 2 than Case 1, leading to a greater effect on uncertainty than the coolant temperature measurement. Given the surface and coolant temperatures each drove uncertainty for a case, uncertainty in overall effectiveness could be improved by reducing coolant temperature measurement uncertainty and calibration uncertainties.

4. Analysis and Results

The goal of this research was to explore the scalability of various flow parameters and their effects on overall effectiveness between temperature regimes. Tests of *Re* = 10,000 and 15,000 were run at four freestream temperature conditions, 350 K, 450 K, 500 K, and 550 K, for a range of blowing ratios between 0.25 and 1.5 at each temperature regime. Due to the challenges of the coolant heating through the delivery block, density ratios resulted ranging from 1.03 at $M = 0.25$ to 1.1 at $M = 1.5$, with *DR* known to ±1.5%. The 450 K freestream condition was the limiting factor for *DR*, and so *DR* for each blowing ratio at the 500 K and 550 K conditions were matched back to the 450 K condition along with additionally reaching the maximum *DR* for the higher temperature cases. The 350 K test cases were done after the other three temperature regime tests, so while *DR* was not exactly matched, the trends and analysis of the results can still be useful.

Section 4.1 reviews the impact of blowing ratio on overall effectiveness. The impact of density ratio on overall effectiveness is detailed in Section 4.2, and the impact of Reynolds number on overall effectiveness is given in Section 4.3. Section 4.4 details additional findings for zero coolant flow cases and the occurrence of significant coolant heating.

Table 9 outlines the leading edge test cases and pertinent parameters, including the *DR* that the 500 K and 550 K tests matched to for each *M*. The 350 K test case was not *DR* matched because the coolant temperatures necessary to do so were not achievable. *I* and *ACR* were also calculated for reference and comparison.

Table 9: Leading edge test cases

Case	Date	Re	Tinf	Tc	M	DR	I	ACR
1	12-Mar-19	10313	451.0	433.8	0.49	1.04	0.23	0.49
2	12-Mar-19	10300	449.1	421.3	0.89	1.07	0.74	0.88
3	12-Mar-19	10304	450.0	413.8	1.23	1.09	1.39	1.22
4	12-Mar-19	10367	459.0	408.7	1.47	1.10	1.95	1.46
5	12-Mar-19	15297	449.1	437.0	0.25	1.03	0.06	0.25
6	12-Mar-19	15241	450.0	431.0	0.49	1.04	0.23	0.49
7	12-Mar-19	15310	449.1	417.0	0.89	1.08	0.73	0.89
8	12-Mar-19	15290	451.9	411.0	1.24	1.1	1.40	1.23
9	12-Mar-19	15392	449.4	409.0	1.48	1.1	1.99	1.47
10	13-Mar-19	14718	500.6	482.7	0.25	1.04	0.06	0.25
11	13-Mar-19	15457	500.9	474.0	0.48	1.06	0.22	0.48
12	13-Mar-19	15194	498.8	457.6	0.88	1.09	0.71	0.88
13	13-Mar-19	15318	498.7	446.4	1.22	1.12	1.33	1.21
14	13-Mar-19	15364	499.0	439.3	1.46	1.14	1.87	1.45
15	13-Mar-19	15284	499.9	483.8	0.24	1.03	0.06	0.24
16	13-Mar-19	15154	500.5	479.2	0.49	1.04	0.23	0.49
17	13-Mar-19	14656	501.5	465.4	0.91	1.08	0.78	0.91
18	13-Mar-19	14488	499.7	456.8	1.29	1.09	1.51	1.28
19	13-Mar-19	14412	499.9	454.1	1.55	1.10	2.19	1.54
20	13-Mar-19	10023	502.2	478.4	0.50	1.05	0.23	0.49
21	13-Mar-19	10011	501.2	465.2	0.89	1.08	0.74	0.89
22	13-Mar-19	10114	500.4	453.7	1.23	1.10	1.36	1.22
23	13-Mar-19	10066	499.9	446.1	1.48	1.12	1.96	1.47
24	13-Mar-19	9888	500.2	454.0	1.51	1.10	2.07	1.50
25	13-Mar-19	9920	500.4	459.9	1.25	1.09	1.44	1.24
26	13-Mar-19	10215	501.1	468.5	0.88	1.07	0.72	0.87
27	13-Mar-19	9876	501.9	479.4	0.50	1.05	0.24	0.50
28	14-Mar-19	15253	551.3	532.1	0.25	1.04	0.06	0.25
29	14-Mar-19	15238	552.6	519.9	0.50	1.06	0.24	0.50
30	14-Mar-19	15291	551.4	499.8	0.90	1.10	0.73	0.89
31	14-Mar-19	15271	551.6	484.7	1.25	1.14	1.37	1.24
32	14-Mar-19	15200	551.6	474.4	1.50	1.16	1.95	1.49
33	14-Mar-19	15149	550.3	497.4	1.51	1.11	2.06	1.50
34	14-Mar-19	15275	550.6	503.6	1.25	1.09	1.43	1.24
35	14-Mar-19	15302	550.6	513.0	0.90	1.07	0.75	0.89
36	14-Mar-19	15311	551.0	526.1	0.50	1.05	0.24	0.50
37	14-Mar-19	15335	551.3	533.9	0.25	1.03	0.06	0.25
38	14-Mar-19	10035	551.5	521.3	0.50	1.06	0.24	0.50
39	14-Mar-19	10117	556.7	507.8	0.90	1.10	0.74	0.89
40	14-Mar-19	10135	556.4	494.1	1.24	1.13	1.39	1.23
41	14-Mar-19	9881	555.6	484.5	1.53	1.15	2.07	1.52
42	14-Mar-19	10127	551.6	498.6	1.50	1.11	2.05	1.49
43	14-Mar-19	10105	551.3	504.2	1.26	1.09	1.44	1.25
44	14-Mar-19	10153	551.0	513.1	0.90	1.07	0.75	0.89
45	14-Mar-19	9870	550.5	523.3	0.51	1.05	0.25	0.51
46	3-Apr-19	10166	351.0	341.1	0.89	1.03	0.78	0.89
47	3-Apr-19	10123	349.7	337.3	1.25	1.04	1.51	1.25
48	3-Apr-19	10030	349.1	334.4	1.52	1.04	2.19	1.51
49	3-Apr-19	14811	349.8	338.1	0.92	1.03	0.82	0.92
50	3-Apr-19	14967	349.5	332.9	1.27	1.05	1.53	1.27
51	3-Apr-19	15145	350.6	331.4	1.50	1.06	2.13	1.50

Data values were taken from each test case in accordance with the red lines in Figure 75 for comparison and analysis. A pixel line of data values was in the streamwise direction between the fourth coolant holes in each row from x/d = 0 and 15. Two spanwise pixel lines of data, each one pitch in length from the streamwise line, were taken at x/d = 4.5 and 12.

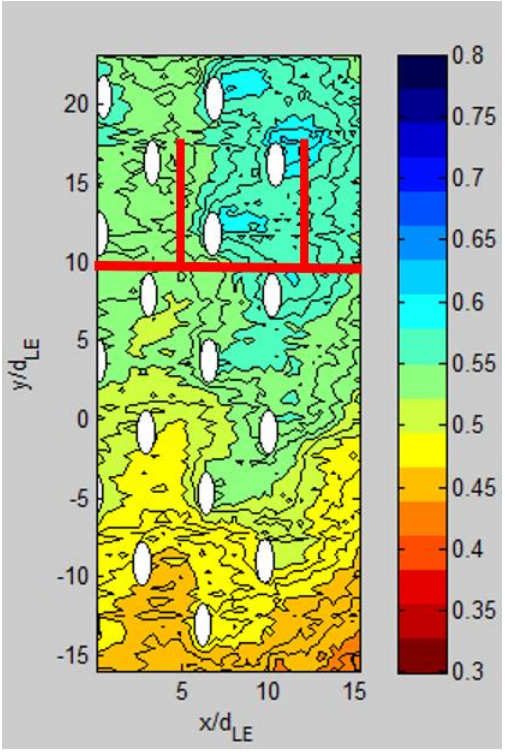

Figure 75: Overall effectiveness data locations

4.1. Blowing Ratio Effects

The effects of increasing blowing ratio in the streamwise direction from $0 < x/d < 15$ are shown in Figure 76, with the 450 K test condition on the left and 550 K on the right. Reynolds number and density ratio were all kept the same between temperature regimes while progressing through each blowing ratio. As expected, overall effectiveness increased with blowing ratio due to increased coolant flow within the airfoil

and over the external surface, peaking at around 0.57 for both freestream temperatures. As *M* increased to 1.5, the improvement between those cases began to diminish. While the increased blowing ratio improved cooling due to conduction, it also caused an increase in momentum ratio, *I*, where the coolant jets were likely beginning to separate from the surface and becoming less effective. As the flow progressed downstream from the stagnation region, better development of coolant coverage was noted across the test cases, shown in Figure 77.

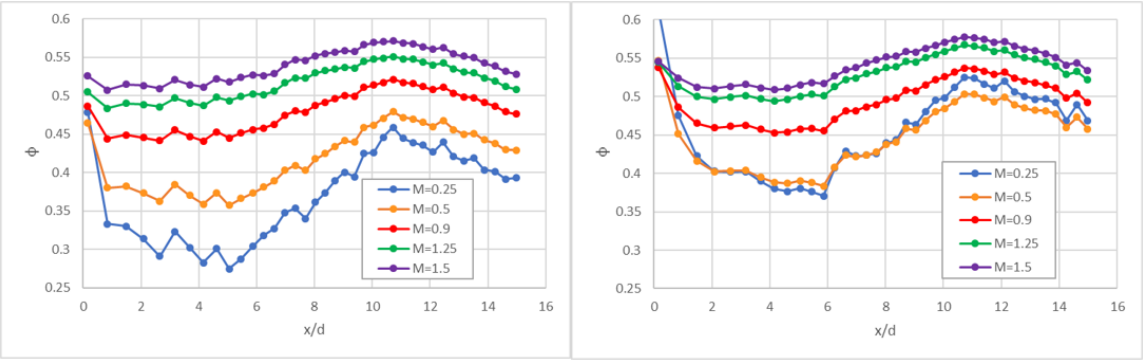

Figure 76: Re=15,000 with increasing M at T_∞=450K (left) and T_∞=550K (right)

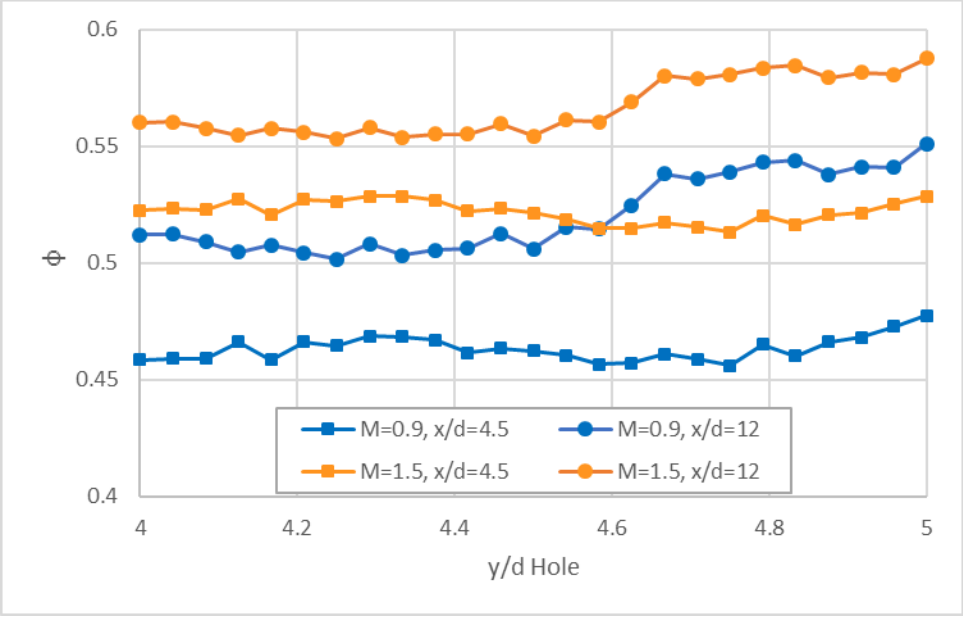

Figure 77: Spanwise overall effectiveness of x/d=4.5 and x/d=12 for M=0.9 and M=1.5, Re=15,000 and T_∞=450K

As noted by Bryant et al. [9] ingestion of the freestream into the central rows of coolant holes at lower blowing ratios of 0.25 and 0.5 was experienced. This resulted in drastically lower, near zero, overall effectiveness around the holes experiencing ingestion. To understand this impact on the current results, Figure 78 shows the test case of M = 0.25 at 450 K and Re = 15,000 compared to the M = 0.9 case. A notable decrease in overall effectiveness to about 0.3 from 0.6 was seen in the lower y/d areas of the surface contour consistent with no cooling being ejected from these holes. However, where Bryant et al. showed a near zero overall effectiveness along the entire length of the row, due to conduction within this model, some cooling of the surface did occur at larger y/d. Raising the blowing ratio to 0.9, as seen in the right image of Figure 78, did result in a dramatic improvement of the cooling flow out of the showerhead row resulting in a significant increase in downstream overall effectiveness. Figure 79 more directly compares the potential ingestion and non-ingestion cases by comparing the spanwise cuts at x/d = 4.5 and 12 for both cases. While both axial locations on the M = 0.25 case are lower, the x/d = 4.5 values are significantly lower than the rest, further confirming that ingestion is possibly occurring. The remainder of this analysis will focus on blowing ratios of 0.9 and higher, consistent with positive ejection of coolant from the holes.

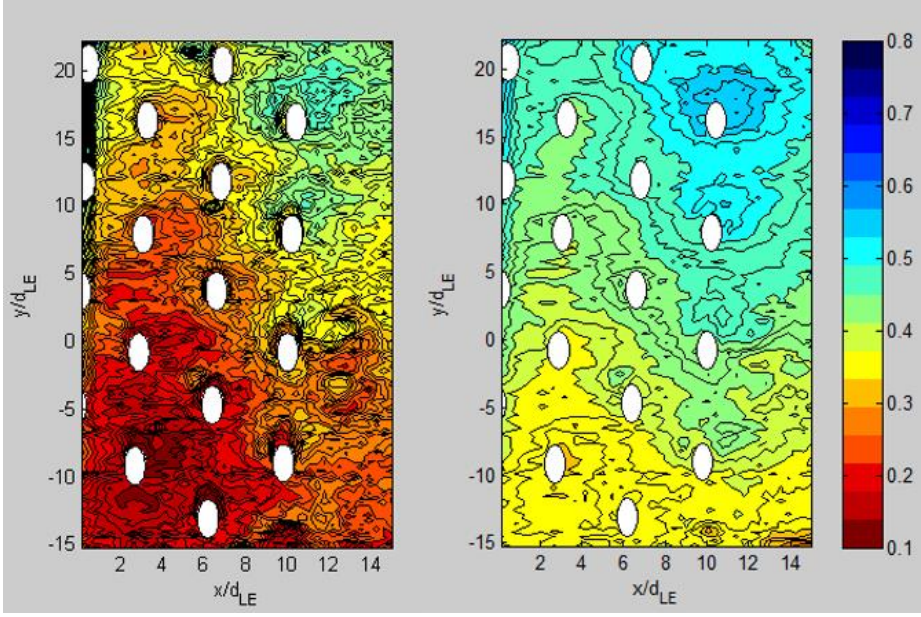

Figure 78: Overall effectiveness for blowing ratio cases M = 0.25 (left) and M = 0.9 (right), T_∞ = 450 K, Re = 15,000

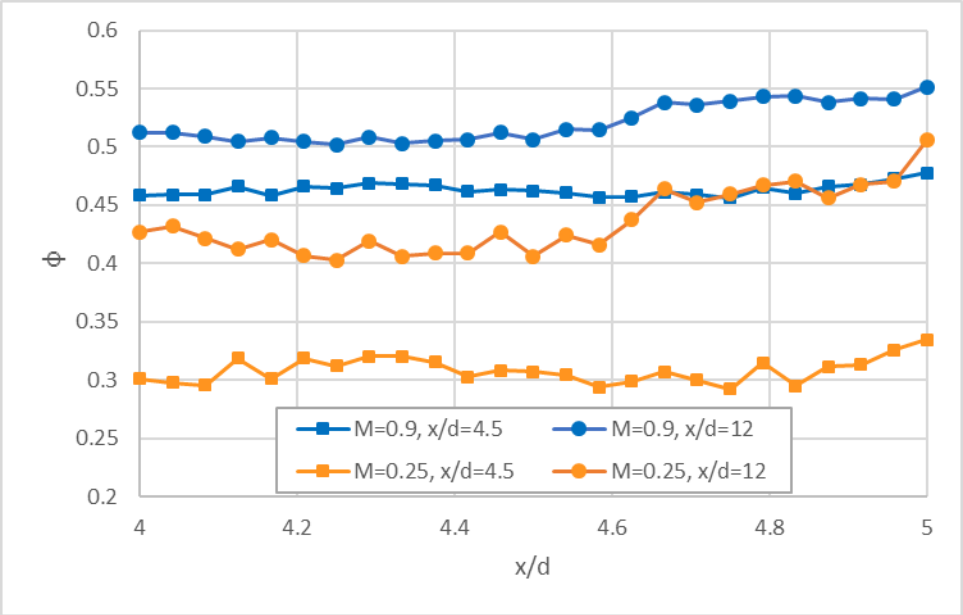

Figure 79: Spanwise overall effectiveness for blowing ratio cases M=0.25 and M=0.9 at x/d=4.5 and x/d=12, T_∞=450K, Re=15,000

Additionally, overall effectiveness was assessed at M = 0 for each temperature regime because there still seemed to be a conduction path for heat to escape from the model. During testing and calibration data points with no coolant flow, T_s was a few degrees cooler than T_∞. If there were no conduction paths from the model, those

temperatures would have been the same. The resulting resting overall effectiveness at each temperature regime with no coolant flow were around that same 0.6 range seen by Vorgert. Due to the very small difference between the freestream, surface, and internal temperatures of less than 10 K, just a 1 K difference in that internal temperature reading would result in a 0.1 shift in overall effectiveness.

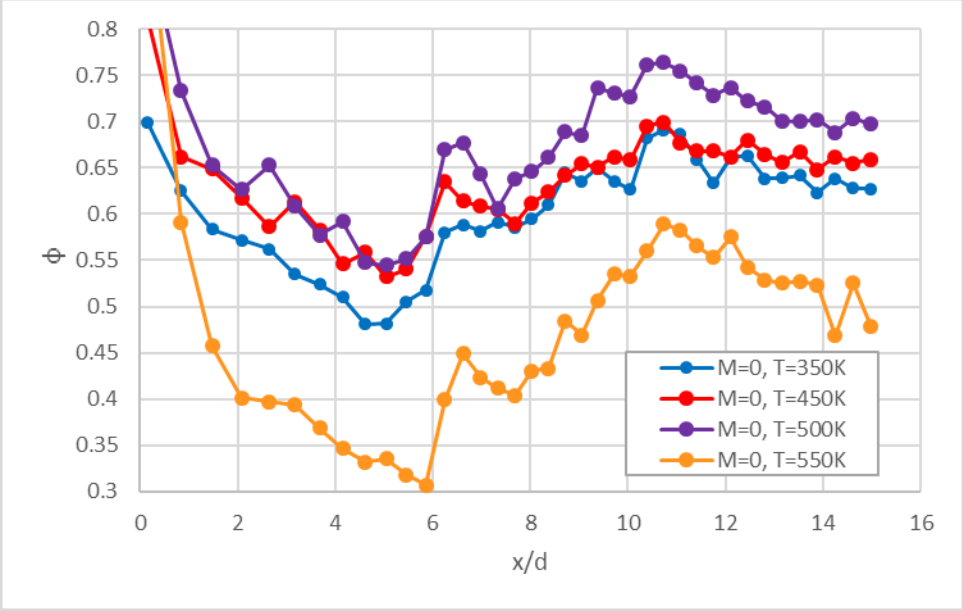

Figure 80: Overall effectiveness at M = 0 for each T∞ tested

4.2. Matched Density Ratio for Scaling Overall Effectiveness

A large part of the motivation for this research was to accurately scale between temperature regimes by matching various flow parameters. The first investigation sought to confirm the impact of matching density ratio on overall effectiveness to allow for scalability and accurate comparison between temperature conditions. The *DR* was matched at 1.07, aside from 1.03 at 350 K, for M = 0.9 at Re = 15,000 across the four temperature regimes. Figure 81 shows the contour plots of overall effectiveness revealing a consistent distribution over the surface between each case.

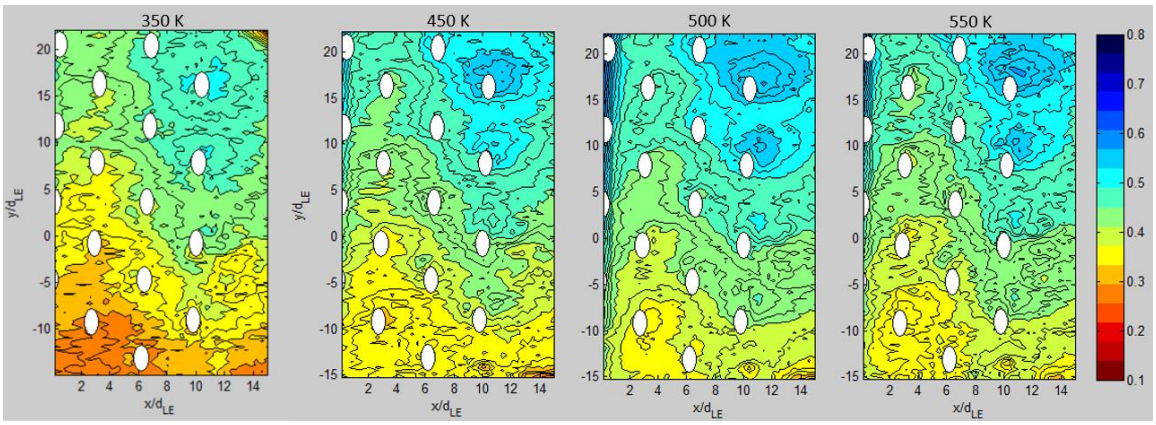

Figure 81: Overall effectiveness contours across temperature regimes, M = 0.9, Re = 15,000

Figure 82 shows the corresponding level of ϕ for these cases for M = 0.9 and 1.5. Aside from discrepancies in measurements right at the leading edge, overall effectiveness remained within 0.03 for nearly the entire streamwise length. Additionally, incorporating the accuracy range of overall effectiveness due to the coolant temperature measurement uncertainty, each set of M lines were within this accuracy range of 0.025 of each other, suggesting that the density ratio directly scales between temperature regimes. Even though DR for the 350 K cases was not exactly matched to the other three temperature regimes and slightly set father apart, the overall effectiveness results were not beyond the allowable uncertainty ranges. Another aspect to note, and this stands for the remainder of the 350 K data in the discussion, this data was the corrected set after the IR calibration adjustment covered in Section 3.5.2 and shown in Figure 67. Before the correction, the values of overall effectiveness for the 350 K cases were up to 0.05 lower than shown in this section.

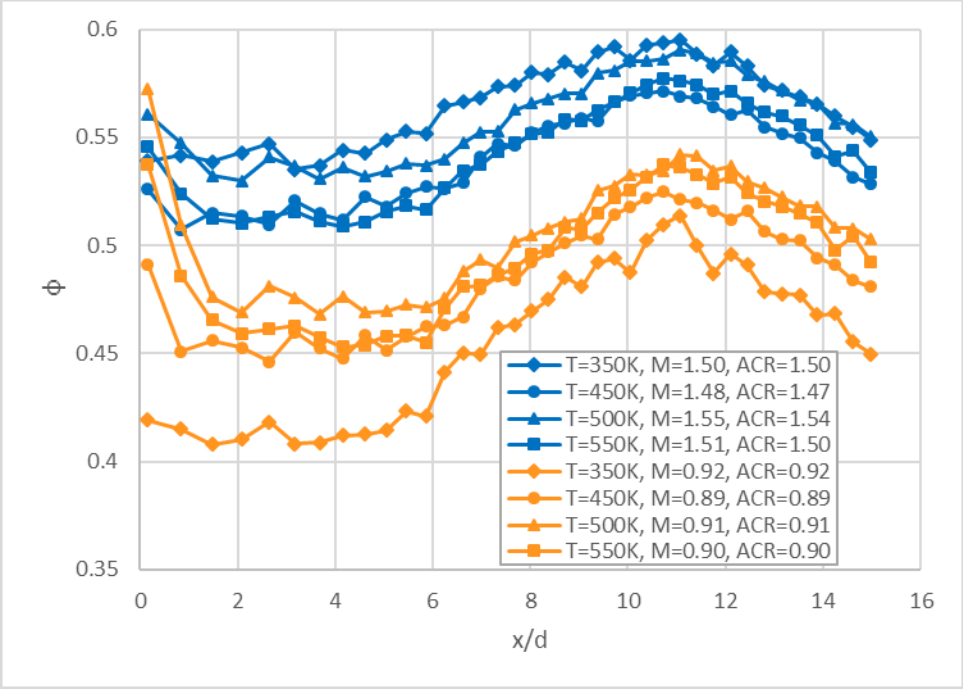

Figure 82: Overall effectiveness between temperature regimes at M=0.9 and M=1.5, Re=15,000

The same cases given in Figure 82 for *Re* = 15,000 are shown in Figure 83 at *Re* = 10,000. The distribution of overall effectiveness was similar but not as clear cut at the lower *Re*. This discrepancy can at least be partly explained by a decreased *Re* requiring lower flow rates overall, resulting in a more compact distribution of the freestream, surface, and coolant temperatures used in the overall effectiveness calculations. The uncertainty of the measurements remains the same, and so greater shifting of the overall effectiveness lines is likely to occur.

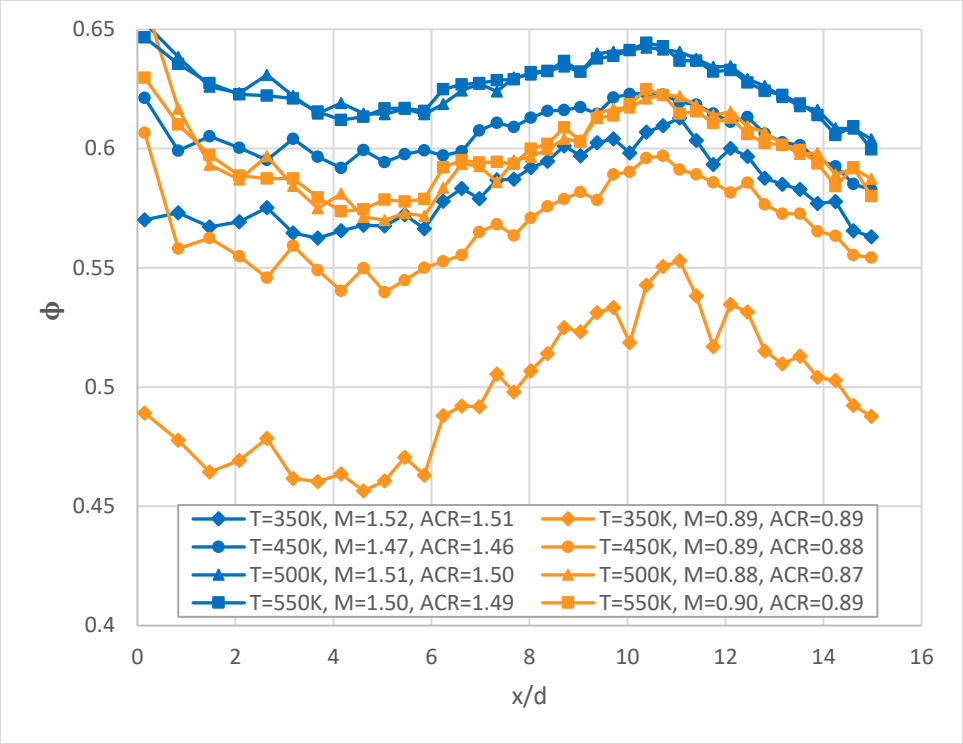

Figure 83: Overall effectiveness between temperature regimes at M=0.9 and M=1.5, Re=10,000

The investigation then aimed to understand the impact of a variable *DR* on the results. For the 500 K and 550 K freestream temperatures, the maximum density ratio at each *M* was also collected. Figure 84 shows overall effectiveness in the streamwise direction at *M* = 0.9 across the three temperature regimes for matched *DR* of 1.07, along with the maximum *DR* of 1.09 and 1.10 at that blowing ratio for the 500 K and 550 K test cases, respectively. Not matching *DR* had a small difference, but within the experimental uncertainty of 0.03 in overall effectiveness at the same freestream temperature. This could likely be due to the low *DR*'s that were achieved through any of the testing. It is possible that a more significant effect on overall effectiveness would occur if there were greater variations in *DR*, which would allow for a fuller appreciation of the impact that changing *DR* has on overall effectiveness.

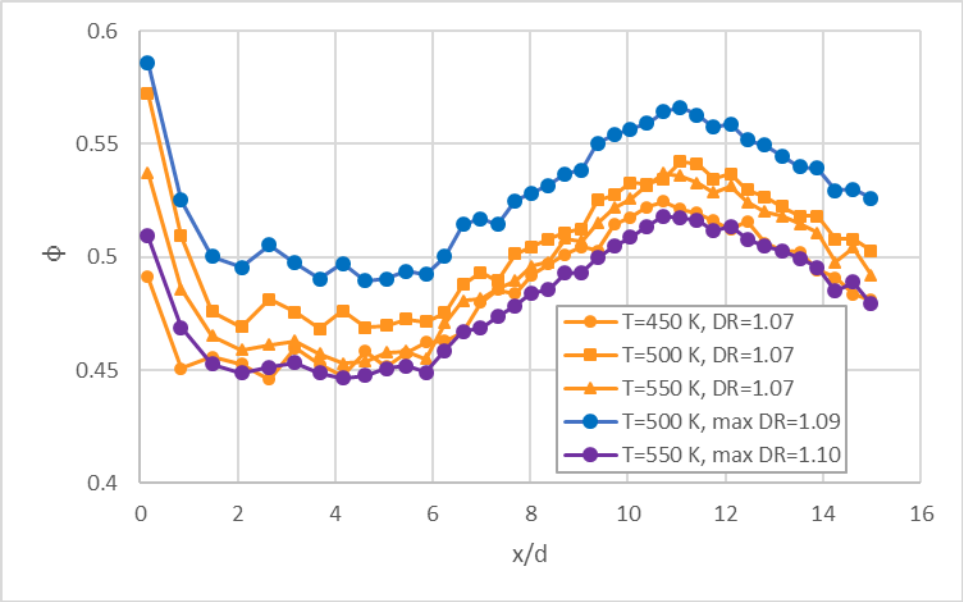

Figure 84: Effect of DR on overall effectiveness at y/d = 10, M = 1.5, Re = 15,000

4.3. Impact of Reynolds Number on Overall Effectiveness

The last investigation focused on the effect of varying Reynolds number by changing the freestream mass flow rate. A drop in overall effectiveness was noted with increasing *Re*, which can visually be seen in Figure 85. Both contours are at T_∞ = 550 K, M = 0.9, and matched *DR*, with the only difference being an increase from 10,000 to 15,000 *Re*. The streamwise plots for M = 0.9 at T_∞ = 350 K, 450 K, 500 K, and 550 K with matched *DR* are displayed in Figure 86 to further highlight the drop in overall effectiveness with increasing *Re*.

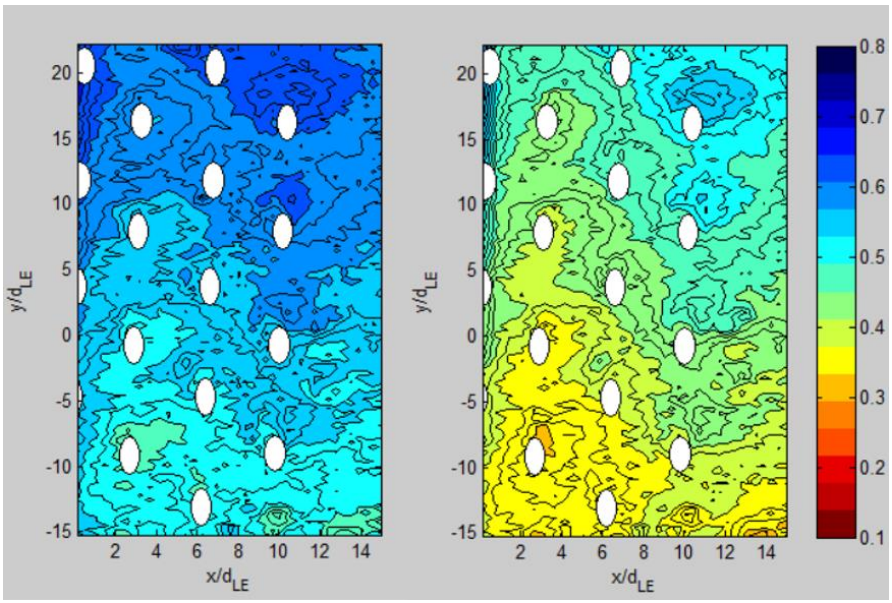

Figure 85: Increasing Reynolds number from 10k (left) to 15k (right)

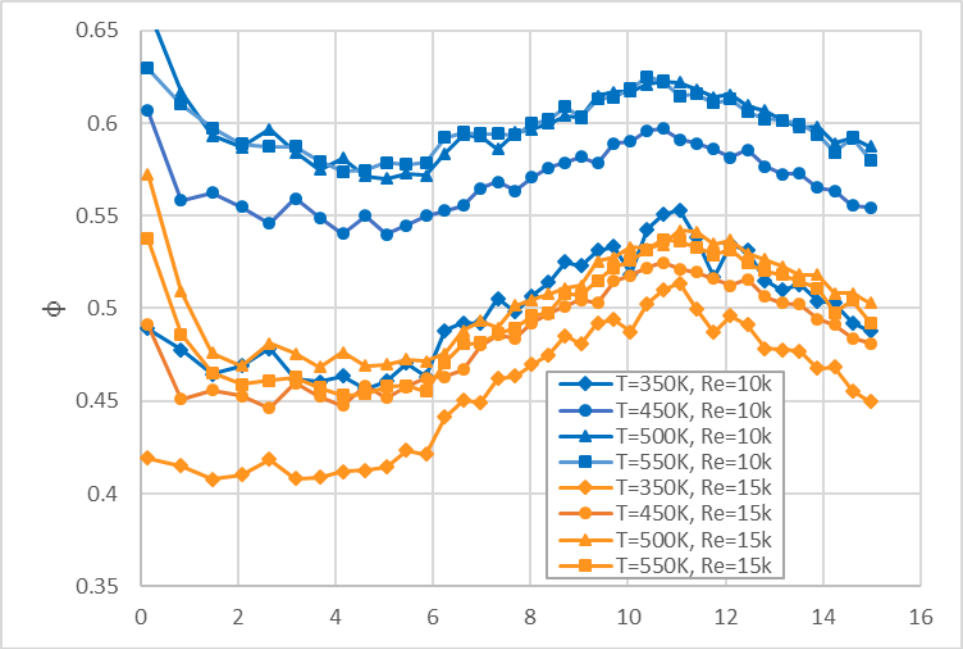

Figure 86: Streamwise overall effectiveness with increasing Re, T_∞=350K, 450K, 500K, and 550K

Figure 87 shows the effects of Reynolds number on overall effectiveness, averaged spanwise at x/d = 12 for each blowing ratio case with matched *DR* in accordance with Table 9. Increasing Reynolds number from 10,000 to 15,000 systematically resulted in a decrease in ϕ of 0.05. The exception to that occurrence were

the 350 K cases. The values of overall effectiveness for T_∞ = 350 K were in the same range as the others but did not follow the same trend. However, due to the extremely small ΔT, only about 7-10 K, between the freestream, surface, and coolant temperatures, a 1 K change in measurements could shift overall effectiveness ±0.08. This knowledge was taken into account, and so the remaining analysis focused on the upper three temperature regimes. As stated in the literature [10], an increase in Reynolds number typically results in a decrease in the local heat transfer coefficient through the Nusselt number correlation given in Eq. (26). This results in a decrease in the overall effectiveness due to its inverse relationship with the external *h*, shown previously in Eq. (3).

$$C = Nu_\theta Re_D^{-1/2} Pr^{-1/3} \tag{26}$$

The value of C in Eq. (26) was taken to be 0.7 from Incropera and DeWitt [10] at the 75 degree position around a cylindrical leading edge corresponding to the x/d =12 location on the airfoil at a Reynolds number of 10,000. The Nusselt number correlation was then used to solve for $h_{f,10k}$ = 1.932 kW/m^{2}K, and therefore Bi_{10k} = 2.95x10^{-4}. Assuming an initial ratio of h_f/h_c = 3 [6,7] and using the experimental ϕ_{10k} = 0.629, the value of adiabatic effectiveness was then solved to be η = 0.505. Assuming that the value of adiabatic effectiveness remained unchanged, that value was put back into Eq. (3) for *Re* = 15,000 along with the corresponding analytical values of $h_{f,15k}$ = 2.536 kW/m^{2}K, Bi_{15k} = 3.876x10^{-4}, and the same h_f/h_c = 3. The analytical value of overall effectiveness when increasing *Re* from 10,000 to 15,000 yielded ϕ_{15k} = 0.605, about a 0.025 drop in overall effectiveness. Given that this analytical assessment does make some assumptions

about the heat transfer characteristic and does not account for the full effects of film cooling on the internal or external wall, it does yield a similar magnitude change to what was seen experimentally, which was a drop of about 0.05-0.07. This leaves plausibility that changes in *Re* across temperature regimes can be accounted for during investigations, and ultimately in fully operational conditions.

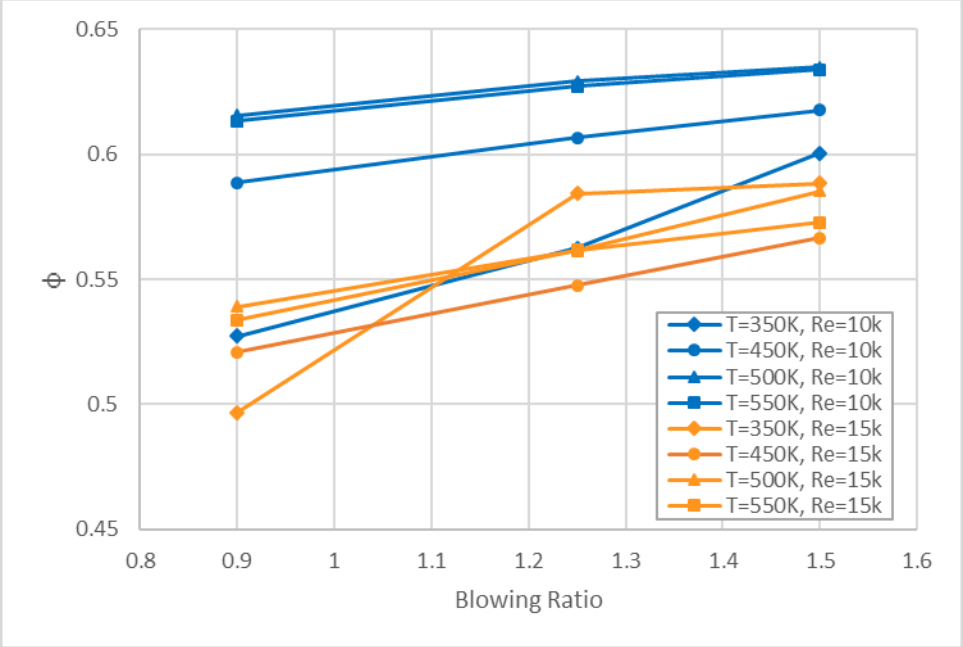

Figure 87: Effects of Reynolds number on overall effectiveness

4.4. Additional Objectives

Additional findings were discovered through the course of performing this investigation and analyzing the results. The first stemmed from determining the no cooling flow overall effectiveness that was initially reported by Vorgert [21] as the "resting" result. This is attributed to conduction through the model, which will be covered in Section 4.4.1. The second finding focuses on the significant amount of heating that the coolant underwent while traveling through the coolant block, resulting in the low *DR* values achieved during testing, and will be discussed in Section 4.4.2.

4.4.1. Resting Overall Effectiveness

As initially described by Vorgert [21], there was still conductive cooling of the airfoil during this investigation. The introduction of the bypass channel aimed to provide a more realistic boundary condition by having hot gas flowing around both sides of the airfoil. However, conduction remained in the model, most likely laterally. The resting overall effectiveness at each temperature regime with no coolant flow was around the same 0.6 range found when coolant was flowing, shown in Figure 88. The main difference was that the temperature change between the freestream, surface, and internal 'coolant' temperatures was not more than 11 K. This meant that even a small amount of conduction could result in an apparent cooling improvement. This small temperature difference also made this measurement uncertain as just a 1 K difference in the internal temperature reading would result in a 0.1 shift in overall effectiveness, as potentially seen with the 550 K case. Table 10 provides the T_∞, T_s, T_c, and resulting overall effectiveness for $M = 0$ at each temperature regime. It is also important to note that the T_s listed is the average value of the four external surface thermocouples, but no thermocouple had more than a 1 K variance from the others.

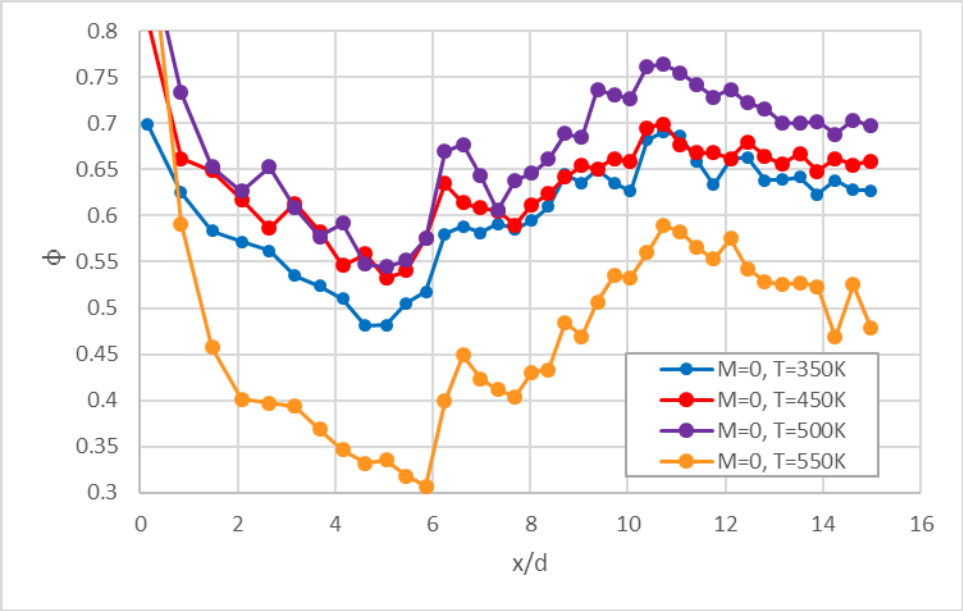

Figure 88: Overall effectiveness at M = 0 for each T_∞ tested

Table 10: Temperature values and overall effectiveness for M = 0 cases

	350 K	**450 K**	**500 K**	**550 K**
T_∞ (K)	352.4	455.8	499.2	550.9
T_s (K)	349.1	448.3	494.4	547.7
T_c (K)	346.6	444.1	490.3	543.7
Φ	0.57	0.64	0.54	0.44

The M = 0 case was plotted against the corresponding M = 0.9 and M = 1.5 cases for the 450 K and 500 K temperatures, shown in Figure 89, which were nearly identical to each other. It is important to note the decrease in overall effectiveness when the coolant is turned on. This decrease was due to the greater difference between the surface and coolant temperatures. Overall effectiveness increases when the surface and coolant temperatures are closer in value, which was noted with the M = 0 cases. This increase in overall effectiveness cannot directly correspond to better cooling, however, because the surface is heating the coolant passage in this case, instead of the coolant cooling the surface. It seems counterintuitive to conclude, but while running coolant decreased the overall effectiveness, the surface of the airfoil was decreased, which is the main goal of

incorporating a film cooling method. The comparisons between surface temperatures at the increasing blowing ratios are shown in Table 11. At both temperature regimes, surface temperatures decrease with increasing blowing ratios, achieving the purpose of film cooling.

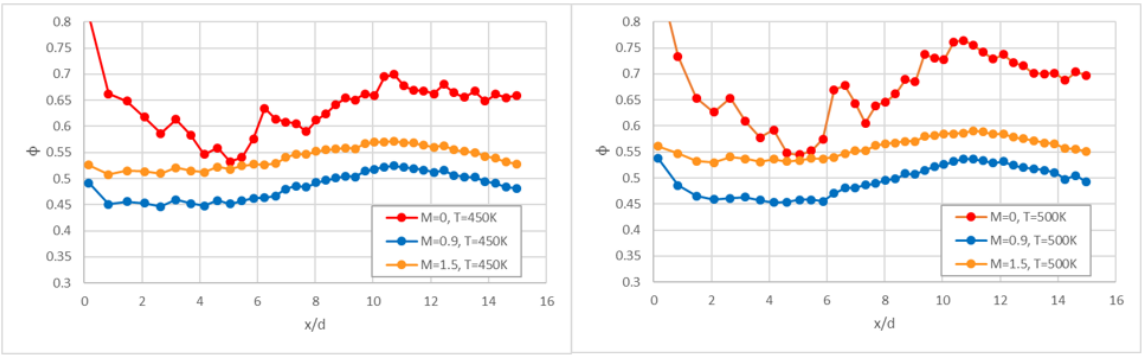

Figure 89: Resting overall effectiveness against M = 0.9 and M = 1.5 for T_∞ = 450 K (left) and T_∞ = 500 K (right), Re = 15,000

Table 11: Temperature values and overall effectiveness for M = 0, 0.9, and 1.5 for T_∞ = 450 K and T_∞ = 500 K, Re = 15,000

	450 K			500 K		
M	**0**	**0.9**	**1.5**	**0**	**0.9**	**1.5**
T_∞ (K)	455.8	449.1	449.4	499.2	501.5	500.0
T_s (K)	448.3	433.5	427.3	494.4	483.7	474.4
T_c (K)	444.1	417.2	409.0	490.3	465.4	454.1
Φ	0.64	0.49	0.55	0.54	0.49	0.56

4.4.2. Coolant Path Heating

Significant heating of the coolant as it progressed through the coolant block toward the airfoil was the main factor in the resulting low *DR* values. While the coolant at the inlet to the block resulted in a *DR* close to 1.8 for the 550 K test cases, heating of the coolant caused that to drop to 1.16 by the time the coolant reached the hole inlet at the higher *M* of 1.5. This coolant heating as it progressed up the internal channel was visualized in the CFD Case 1 results, shown in Figure 90. With velocity vectors colored by temperature, the rapid increase in temperature can be tracked as the coolant progresses

up the channel from the inlet toward the airfoil. The CFD test case set the inlet *DR* to 1.5, but as was experienced, that certainly did not result in the same *DR* at the airfoil. The coolant entered the block at 333 K, but gained nearly 70 K in the quick turn upward. Upon entering the larger coolant plenum, the temperature increased to about 445 K. When the coolant finally progressed through the impingement plate and reached the internal side of the airfoil where the coolant temperature is measured for the overall effectiveness calculation, it was at around 460-470 K, resulting in the low *DR* of 1.08.

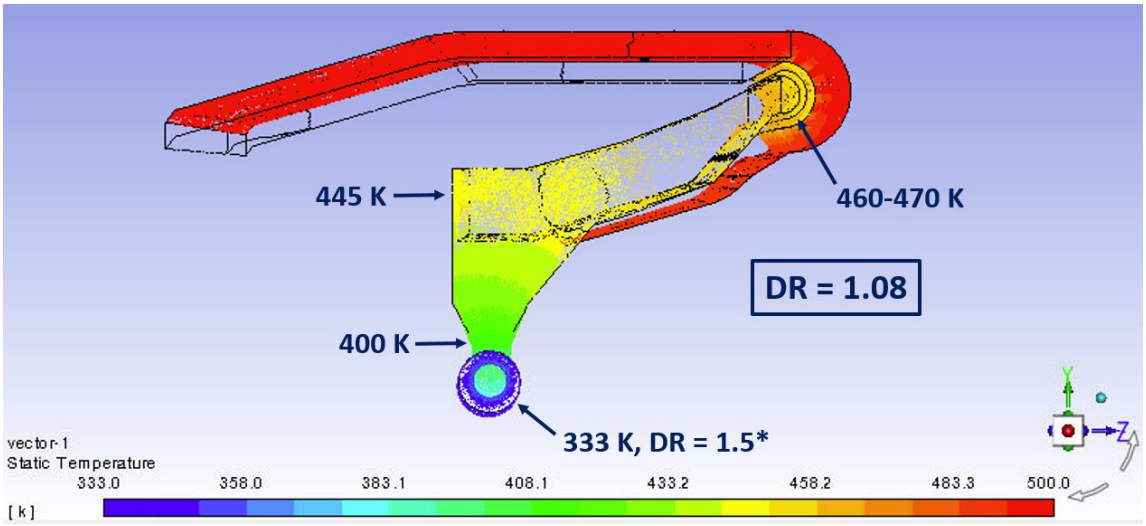

Figure 90: CFD coolant heating through internal channel, T_∞ = 500K, Re = 15,000, M = 1.0

The same temperature increase was also noted throughout all of the experimental test cases. Figure 91 shows the same CFD image with the experimental temperatures tracked from similarly to the CFD case above, but at a slightly lower *M* = 0.9. The experimental coolant temperatures are provided at the thermocouple locations shown in Figure 60 which were before the inlet to the block, inside the impingement plate, and between the impingement plate and the internal airfoil surface. Those temperatures are shown in the figure along with the *DR* at the inlet (*DR* = 1.59) and the resulting actual *DR* at the airfoil for the test case (*DR* = 1.09). As seen with the CFD, the high *DR* that was

specified going into the turbine blade model was not achieved at the airfoil surface after traveling through the internal channel. Because of the highly conductive nature of the metallic blade, specifying the inlet *DR* to the airfoil will not mean that the same *DR* was experienced out of the coolant holes. An understanding of the coolant heating involved would lead to more accurate assessments and comparison of film cooling data.

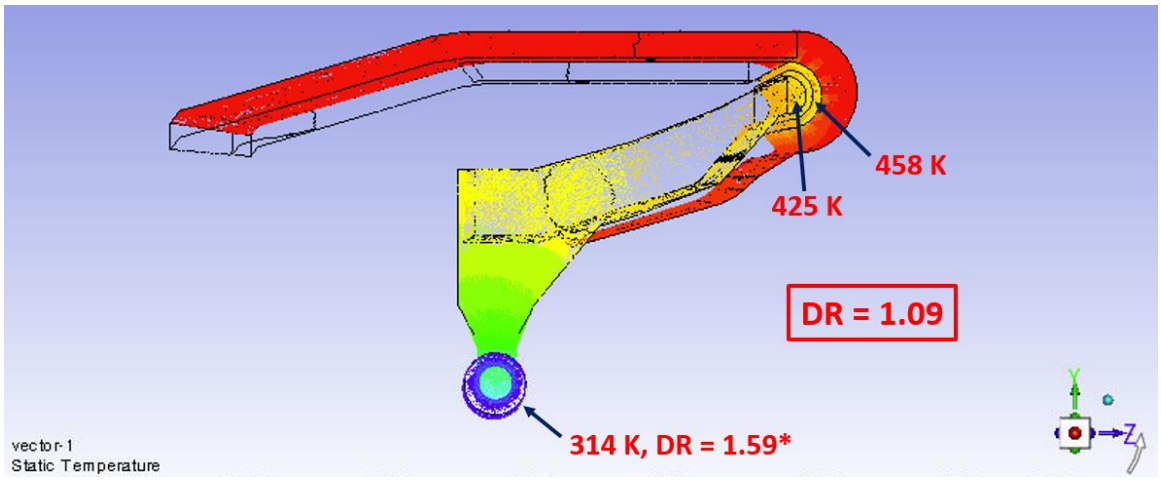

Figure 91: Experimental coolant heating through internal channel, T_∞ = 500K, Re = 15,000, M = 0.9

To illustrate the impact of the coolant heating and lower *DR* on overall effectiveness, test cases of M = 0.9 and a more extreme M = 5.37, both at T_∞ = 550 K and Re = 15,000, shown in Figure 92. The actual DR cases were experimentally collected, while the DR = 1.5 cases were adapted using a T_C measurement of 366 K that would correspond to that density ratio. The figure shows how much overall effectiveness could change with a greater ΔT between the coolant and freestream, but is not fully accurate because the same surface temperatures were used in the recalculations. In a real test with the decreased coolant temperature, the corresponding surface temperatures would decrease, as well, leading to a less drastic decrease in overall effectiveness.

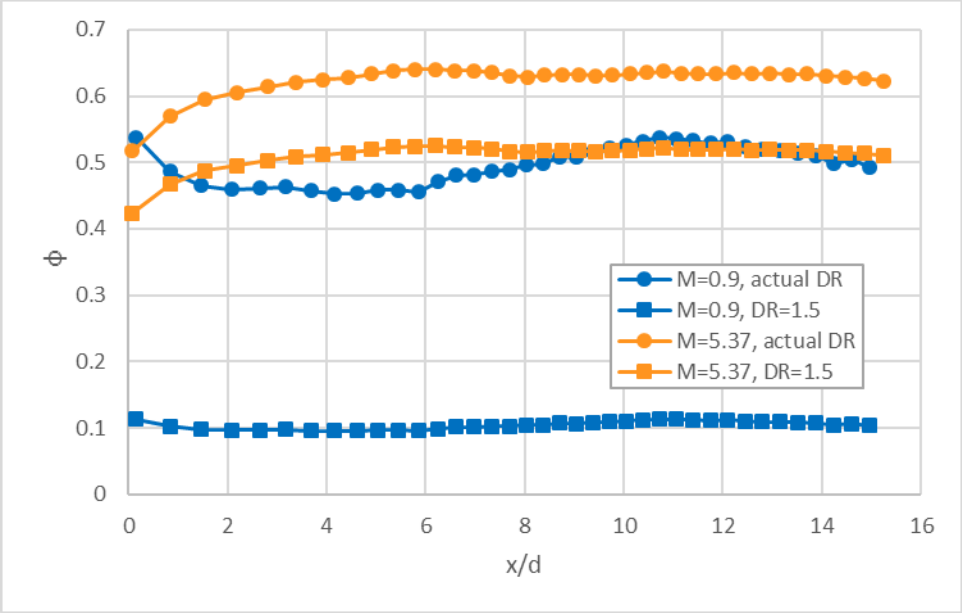

Figure 92: Potential impact of increased DR on overall effectiveness

5. Conclusion

With the creation and development of gas turbine engines, the need to create cooling methods for the turbine blades quickly became apparent due to ever-rising combustion temperatures to extract more power and better performance. The increased temperatures, along with frequent temperature fluctuations, causes the blades to degrade during their operation. Various cooling schemes allow these blades to operate with higher combustion temperatures, even beyond the melting points of the blade. Challenges existed of thoroughly analyzing the cooling effectiveness of gas turbine blade cooling methods at engine operating temperatures. Scaling down to lower temperature regimes that were achievable in laboratory environments while accurately predicting effectiveness at operation conditions was the motivation for this research.

This investigation focused on three main objectives. The first objective was to investigate the effectiveness of geometric scaling between the FCR and an existing large scale facility. The second was to further investigate the effects of various nondimensional parameters on film cooling effectiveness. The third objective was to analyze the ability to scale overall effectiveness between temperature regimes by matching various nondimensional parameters.

Near scalability was achieved by using a geometrically matched one-sided airfoil model of Bryant's large scale, two-sided model. The model was made of Inconel 718 for the beneficial Biot number scalability properties of the material. A bypass channel beneath the one-sided model provided the necessary flow split without requiring the freestream mass flow of a two-sided model. The leading edge configuration, consisting of seven staggered rows of six cylindrical holes each, was shifted by one pitch from

Tewaheftewa's previous design to allow for better visibility of flow development by the IR camera. The model had thermocouples integrated to obtain temperature data at various points on the internal and external surfaces, as well as the internal coolant plenums. These temperatures were utilized with IR thermography to create contour plots to use in assessing overall effectiveness between test cases.

By matching various flow parameters, such as blowing ratio, Reynolds number, and density ratio, overall effectiveness could be scaled between cases. Four temperature regimes were investigated: 350 K, 450 K, 500 K, and 550 K, with Reynolds numbers of 10,000 and 15,000 were run at each temperature. Blowing ratio sweeps of 0.5-1.5 were performed at the 10,000 *Re* and 0.25-1.5 at the 15,000 *Re* cases. Even though the differences were small, DR was matched for each M across the upper three temperature regimes to account for any slight discrepancies in overall effectiveness it may have caused. When matching these parameters, overall effectiveness was calculated and compared between cases to track the effects of the parameters and the ability to scale the effectiveness among temperature regimes.

Trends of increasing overall effectiveness by increasing blowing ratio were identified and validated with other research and literature. Overall effectiveness peaked at 0.57 with the highest blowing ratio of $M = 1.5$, similar to surrounding research. A plateauing effect began to be observed with increasing blowing ratio because while conductive cooling was still increasing, the momentum ratio at the high blowing ratios was likely causing the coolant jets to separate from the surface, countering the conductive increase in overall effectiveness. Potential cases of ingestion were also noted at the lower blowing ratios of 0.25 and 0.5, which was consistent with Bryant's low blowing ratio

tests. Due to this investigation using a high conductive material, some cooling by conduction was still experienced with ϕ = 0.3, where Bryant had near-zero values for overall effectiveness in the ingestion regions.

The effects of matching density ratio on scaling overall effectiveness were investigated. *DR* at the 500 K and 550 K cases were matched at each *M* and *Re* to the corresponding test cases at 450 K. These upper three test cases were focused on for the *DR* analysis because the 350 K test cases could not reach the *DR* at 450 K. While the density ratios at the upper three test cases were very low to begin with due to significant coolant heating through the test block, the *DR*'s experienced at 350 K would have been too low to match the higher temperature to in order to have a useful analysis. Matching *DR* between temperature regimes with blowing ration and Reynolds number also matched, allowed for consistent overall effectiveness distributions over the airfoil surface, with values within 0.03 of each other. Adjusting the coolant temperature within the range of measurement uncertainty shifted the overall effectiveness values by as much as 0.025, suggesting that the overall effectiveness plots could indeed collapse and scale between temperature regimes.

Effects of increasing Reynolds number were also analyzed and were confirmed to experience a decrease in overall effectiveness in accordance with other experimentation and a numerical analysis. Again, the upper three temperatures were focused on due to skewed results from measurement uncertainty at the 350 K range. Increasing the Reynolds number from 10,000 to 15,000 resulting in a systematic decreasing in overall effectiveness of 0.05. This effect was also investigated analytically. A relation between Reynolds number and convective heat transfer coefficient exists through the Nusselt

number correlation. Due to the inverse relationship h has with overall effectiveness, when Re increases, h increases, causing a decrease in ϕ. Allowing for some assumptions to be made, the analytic analysis resulted in a 0.025 drop in overall effectiveness, which is at least on the same scale as the 0.05 drop seen experimentally.

After analyzing accuracies of temperature measurements and identifying how those changes affected overall effectiveness results, it was found that overall effectiveness fell within the range of direct scalability across the four temperature regimes tested. More precise and thorough measurements would allow further confirmation for scalability, but this investigation found direct overall effectiveness scaling to be plausible when matching flow parameters.

Two additional findings were realized through the course of this investigation. A no cooling flow overall effectiveness existed from conduction paths through the model that was at least the same, if not greater, than the overall effectiveness values at each temperature regime with coolant flowing. While the overall effectiveness dropped when coolant was flowing, the surface temperatures also dropped, which is the goal of implementing film cooling methods. Secondly, significant heating of the coolant was experienced as it traveled through the block's internal channel, creating very low density ratios. If the density ratio going into the model was around 1.5, the coolant temperature rapidly increased as it progressed to the airfoil coolant plenum due to the model's high conductivity, resulting in a density ratio of about 1.08. Accounting for this heat gain of the coolant would allow for more accurate assessments of film cooling investigations and performance.

Pressure side film cooling configurations using shaped holes were set up to be investigated through follow-on research. The shaped holes would allow coolant to slow down and increase spreading upon interaction with the freestream, increasing coverage and effectiveness. A new airfoil with modular plates containing the shaped holes was developed, along with a new coolant delivery block. The coolant delivery block sought to simulate the series of U-bend channels that feed the rows of coolant holes around a typical turbine blade. Reynolds numbers around 15,000 and a series of blowing ratios will be investigated at similar temperatures to those of the leading edge tests to analyze effectiveness.

Future research will explore other cooling configurations and a wider range of flow parameters. Additionally, more precise and accurate temperature measurement methods could help improve overall effectiveness results and tighten the analysis further. Lastly, more efficient coolant delivery could result in higher density ratios and the ability to explore even higher temperature regimes for expanded scalability.

References

[1] Bogard, D. G. and Thole, K. A., (2006), "Gas Turbine Film Cooling," *Journal of Propulsion and Power*, 22(2), 249–270.

[2] Polanka, M. D., Rutledge, J. L., Bogard, D. G., and Anthony, R. J., (2016), "Determination of Cooling Parameters for a High-Speed, True-Scale, Metallic Turbine Vane," *Journal of Turbomachinery*, 139(1), 011001.

[3] Greiner, N. J., Polanka, M. D., and Rutledge, J. L. (2014), "Scaling of Film Cooling Performance From Ambient to Engine Temperatures," *Journal of Turbomachinery*, 137(7), 071007.

[4] Rutledge, J. L. and Polanka, M. D., (2014), "CFD Evaluations of Unconventional Film Cooling Scaling Parameters on a Simulated Turbine Blade Leading Edge," *Journal of Turbomachinery*, 136(10), 101006.

[5] Dyson, T. E., (2013), "Overall Effectiveness for a Film Cooled Turbine Blade Leading Edge With Varying Hole Pitch," *Journal of Turbomachinery*, 135(3), 031011.

[6] Rutledge, J. L., Polanka, M. D., and Bogard, D. G., (2016), "The Delta Phi Method of Evaluating Overall Film Cooling Performance," *Journal of Turbomachinery*, 138(7), 071006.

[7] Stewart, W. R. and Dyson, T. E., (2017), "Conjugate Heat Transfer Scaling for Inconel 718," ASME Turbo Expo, pp. 1–9, GT2017-64873.

[8] Wiese, C. J., Bryant, C. E., Rutledge, J. L., and Polanka, M. D., (2018), "Influence of Scaling Parameters and Gas Properties on Overall Effectiveness on a Leading Edge Showerhead," *Journal of Turbomachinery*, 140(11), 111007.

[9] Chandran, D. and Prasad, B., (2014), "Conjugate Heat Transfer Study of Combined Impingement and Showerhead Film Cooling Near NGV Leading Edge," *International Journal of Rotating Machinery*, 1-13.

[10] Oguntade, H. I., Andrews, G. E., Ingham, D. B., Pourkashanian, M., and Burns, A. D., (2012), "Conjugate Heat Transfer Predictions of Effusion Cooling: The Influence of Injection Hole Size on Cooling Performance," ASME Turbo Expo, GT2012-68516, pp. 1-12.

[11] Davidson, F. T., Kistenmacher, D. A., and Bogard, D. G., (2013), "Film Cooling with a Thermal Barrier Coating: Round Holes, Craters and Trenches." *Journal of Turbomachinery*, 136(4), 041007.

[12] Tewaheftewa, J. G., "Investigation of Geometric and Thermal Scaling Effects on a Simulated Turbine Vane Leading Edge Model," Master's Thesis, Air Force Institute of Technology, WPAFB, OH, 2018, AFIT-ENY-MS-18-M-297, 2018.

[13] Albert, J. E., Bogard, D. G., and Cunha, F., (2004), "Adiabatic and Overall Effectiveness for a Film Cooled Blade," ASME Paper No. GT2004-53998.

[14] Schmidt, D., Sen, B., and Bogard, D., (1996), "Film Cooling with Compound Angle Holes: Adiabatic Effectiveness," *Journal of Turbomachinery*, 118(4), 807-813.

[15] Baldauf, S., Scheurlen, M., Schulz, A., and Wittig, S., (2002), "Correlation of Film-Cooling Effectiveness from Thermographic Measurements at Engine-like Conditions," *Journal of Turbomachinery*, 124(4), 686-698.

[16] Gritsch, M., Schulz, A., and Wittig, S., (1998), "Adiabatic Wall Effectiveness Measurements of Film-Cooling Holes with Expanded Exits," *Journal of Turbomachinery*, 120(3), 549-556.

[17] Li, X., Sun, B., You, H., and Wang, L., "Evolution of Rolls-Royce Air-Cooled Turbine Blades and Feature Analysis," Procedia Engineering, Vol 99, 2015, 1482-1491.

[18] Nickol, J., Mathison, R., Dunn, M., Liu, J., and Malak, M., (2017), "An Investigation of Coolant Within Serpentine Passages of a High-Pressure Axial Gas Turbine Blade," *Journal of Turbomachinery*, 139(9), 091006.

[19] Omega®, 2018, "Thermocouples" [Online]. Available: https://www.omega.com/prodinfo/thermocouples.html. [Accessed: 18-Oct-2018]

[20] Damele, C. J., (2013), "Operational Characteristics of an Ultra Compact Combustor," Master's Thesis, Air Force Institute of Technology, WPAFB, OH, AFIT-ENY-14-M-13.

[21] Vorgert, C. J., (2017), "Relating Film Cooling Performance Between Ambient and Near Engine Temperatures," Master's Thesis, Air Force Institute of Technology, WPAFB, OH, AFIT-ENY-MS-17-M-298.

[22] Ashby, R. W., (2016), "Scaling Film Cooling Performance From Ambient to Near Engine," Master's Thesis, Air Force Institute of Technology, WPAFB, OH, AFIT-ENY-MS-16-D-036.

[23] Bryant, C. E., Weise, C. J., Rutledge, J. L., and Polanka, M. D., (2019), "Experimental Evaluations of the Relative Contributions to Overall Effectiveness

in Turbine Blade Leading Edge Cooling," *Journal of Turbomachinery*, 141(4), 041007.

[24] Sweeney, P. C. and Rhodes, J. F., (1999), "An Infrared Technique for Evaluating Turbine Airfoil Cooling Designs," *Journal of Turbomachinery*, 122(1), 170-177.

[25] Lawson, S. A., Straub, D. L., Beer, S., Casleton, K. H., and Sidwell, T., (2013), "Direct Measurements of Overall Effectiveness and Heat Flux on a Film Cooled Test Article at High Temperatures and Pressures," ASME Turbo Expo 2013, San Antonio, Texas, USA, GT2013-94685.

[26] Nathan, M. L., Dyson, T. E., Bogard, D. G., and Bradshaw, S. D., (2013), "Adiabatic and Overall Effectiveness for the Showerhead Film Cooling of a Turbine Vane." *Journal of Turbomachinery*, 136(3), 031005.

[27] Martiny, M., Schiele, R., Gritsch, M., Schulz, A., and Wittig, S., (1996), "In Situ Calibration for Quantitative Infrared Thermography," *3rd QIRT Conference*, Stuttgart, Germany, pp. 3-8.

[28] Ochs, M., Horbach, T., Schulz, A., Koch, R., and Bauer, H. J., (2009), "A Novel Calibration Method for an Infrared Thermography System Applied to Heat Transfer Experiments," *Meas. Sci. Technol.*, 20(7), p. 75103.

[29] Dees, J. E., Bogard, D. G., Ledezma, G. A., Laskowski, G. M., and Tolpadi, A. K., (2012), "Experimental Measurements and Computational Predictions for an Internally Cooled Simulated Turbine Vane." *Journal of Turbomachinery*, 134(6), 061003.

[30] Fischer, J. P., Rutledge, J.L., McNamara, L.J., and Polanka, M.D., (2019), "Scaling Flat Plate, Low Temperature Adiabatic Effectiveness Results Using the Advective Capacity Ratio," ASME Turbo Expo 2019, GT2019-90997, pp. 1-13.

[31] Parks, A. K., (2012), "Desensitizing Flame Structure and Exhaust Emissions to Flow Parameters in an Ultra-Compact Combustor," Master's Thesis, Air Force Institute of Technology, WPAFB, OH, AFIT/GAE/ENY/12-M33.

[32] Moffat, R. J., (1988), "Describing the Uncertainties in Experimental Results," *Exp. Therm. Fluid Sci.*, 1(1), pp. 3-17.

[33] http://laser-industrial.com/wp-content/uploads/2014/10/ldex1.jpg [Accessed: 21-Apr-2019]

REPORT DOCUMENTATION PAGE		Form Approved OMB No. 0704-0188

1. REPORT DATE *(DD-MM-YYYY)*	2. REPORT TYPE	3. DATES COVERED *(From - To)*
06/13/2019	Master's Thesis	March 2018-June 2019

4. TITLE AND SUBTITLE
Investigation of Thermal Scaling Effects for a Turbine Blade Leading Edge and Pressure Side Model

5a. CONTRACT NUMBER

5b. GRANT NUMBER

5c. PROGRAM ELEMENT NUMBER

6. AUTHOR(S)
Lynch, Ryan A., First Lieutenant, USAF

5d. PROJECT NUMBER

5e. TASK NUMBER

5f. WORK UNIT NUMBER

7. PERFORMING ORGANIZATION NAME(S) AND ADDRESS(ES)
Air Force Institute of Technology
Graduate School of Engineering and Management (AFIT/ENY)
2950 Hobson Way, Building 640
WPAFB OH 45433-8865

8. PERFORMING ORGANIZATION REPORT NUMBER
AFIT-ENY-MS-19-J-072

9. SPONSORING/MONITORING AGENCY NAME(S) AND ADDRESS(ES)
Dr. Randall Mathison
Assistant Professor, Department of Mechanical and Aerospace Engineering
The Ohio State University
2300 West Case Road
Columbus, OH 43235

10. SPONSOR/MONITOR'S ACRONYM(S)

11. SPONSOR/MONITOR'S REPORT NUMBER(S)

12. DISTRIBUTION/AVAILABILITY STATEMENT
DISTRIBUTION STATEMENT A:
APPROVED FOR PUBLIC RELEASE; DISTRIBUTION UNLIMITED

13. SUPPLEMENTARY NOTES
This material is declared a work of the U.S. Government and is not subject to copyright protection in the United States.

14. ABSTRACT
Recent experiments have attempted to quantify the overall cooling effectiveness at elevated temperature conditions. The Film Cooling Rig (FCR) at the Air Force Institute of Technology has been modified to better match the configuration of a similar large scale, low temperature rig at the Air Force Research Laboratory and used the thermal scaling capability of Inconel 718 across temperature ranges 350-550 K. Effects of blowing ratio, density ratio, and Reynolds number on overall effectiveness and scalability were investigated. Scalability was plausible when matching those flow parameters. The highly conductive material created overall effectiveness results and caused significant coolant heating and low density ratios.

15. SUBJECT TERMS
Film cooling

16. SECURITY CLASSIFICATION OF:			17. LIMITATION OF ABSTRACT	18. NUMBER OF PAGES	19a. NAME OF RESPONSIBLE PERSON
a. REPORT	b. ABSTRACT	c. THIS PAGE			Polanka, Marc D., USAF ADVISOR
U	U	U	U	141	19b. TELEPHONE NUMBER *(Include area code)* (937) 785-3636, ext 4714 (NOT DSN)

Standard Form 298 (Rev. 8/98)
Prescribed by ANSI Std. Z39.18